ROBOTICS AND MECHATRONICS

Flow visualisation using small bubbles inside opaque structures: An experimental approach

K.J.J. (Kay) van der Hoogt

MSc Report

Committee:
Prof.dr.ir. C.H. Slump
Dr.ir. M. Abayazid
E. Groot Jebbink, MSc

July 2017

030RAM2017
Robotics and Mechatronics
EE-Math-CS
University of Twente
P.O. Box 217
7500 AE Enschede
The Netherlands

UNIVERSITY OF TWENTE.

MIRA CTIT
BIOMEDICAL TECHNOLOGY AND TECHNICAL MEDICINE

Abstract

Cardiovascular diseases are a major cause of death in the Netherlands. One of these diseases is the aneurysm of the aorta abdominalis (AAA). In this case the vessel diameter is too large, which can cause rupturing of the aorta. When a patient with an AAA have to be treated, this can done by the placement of a stent graft. Here, a surgeon has two options: Open repair or Endovascular repair (EVAR).

This topic is discussed in chapter 1, which is the introduction of this thesis. Here, we discuss the pathology, the treatment, and the complications that might occur. Furthermore, some aspects about choosing the right stent graft are discussed. Placing a stent graft can also have an influence on the fluid mechanical behaviour in and around the stent graft. Research is done, in vitro and by computation fluid dynamics (CFD), to gain more knowledge about the fluid mechanical phenomena.

Doing in-vitro-studies can give some problems. Stent grafts are not transparent. For analysing flow, structures have to be made transparent in some cases. For example, if Particle Image Velocimetry (PIV) based on optical techniques (lasers) is used.

In this thesis, we looked for a method to visualise flow in opaque structures.

As first step, optic techniques were used to visualise a laminar flow inside a straight tube. This is discussed in chapter 2 in detail. Visualising flow profiles can be done with proper illumination, a camera system and tracer particles (which are injected into the flow). The diameter of these particles has to be small enough to follow the flow. Following the flow accurately is called tracer fidelity. Combining all these aspects makes flow visualisation possible.

In our experiments, flow visualisation was done with the hydrogen bubble technique. This is a technique which is based on the electrolysis of water. By placing a very thin metal wire in a tube and using pulsed voltages, hydrogen bubbles were created. These bubbles formed so-called timelines. Using these timelines, the offset of a parabolic profile was seen in the some obtained images. The results of these experiments were used as first step in our flow experiments.

Chapter 3 discusses visualisation of bubbles with X-rays. X-rays can be used for visualisation inside opaque structures. For this part of the research, bubbles were injected via thin needles (placed inside a tube filled with water) and visualised with single shot X-ray images. The results of this technique showed that small microbubbles are difficult to visualise with X-rays. Some of the limitation factors, here, were the resolution of the imaging system and not much contrast between bubbles and water.

Because we made snapshots, only the position of bubbles in one frame could be seen. To visualise a motion more frames are needed. In X-ray imaging, this can be accomplished by adding a shutter in front of the X-ray tube. A shutter is able to block X-rays for a predefined period. This means the timing of the shutter is essential to make consecutive images.

A shutter was build and placed in front of the X-ray tube. Because this timing was not optimal during the experiments, future research is necessary to optimise this imaging technique further.

In the last chapter, other parameters (pulse wave velocity and wall shear stress) are discussed in relation to the measurement principles to obtain data in in-vitro studies. These include aspects like algorithms needed to obtain the pulse transit time (PTT), and some theoretical background regarding to these parameters.

Samenvatting

Hart- en vaatziekten is een van de grootste doodsoorzaken in Nederland. Een van deze ziekten is het aneurysma van de aorta abdominalis (AAA). Hierbij is de diameter van het bloedvat te groot, wat onder bepaalde omstandigheden een ruptuur van de aorta kan veroorzaken. Als een patiënt moet worden behandeld, kan dat worden gedaan door het plaatsen van een stent. Hiervoor heeft een chirurg twee opties: de open benadering of de endovasculaire benadering (EVAR).

Dit onderwerp wordt verder uiteengezet in hoofdstuk 1, de introductie van deze thesis. Hier worden de pathologie, behandeling en complicaties besproken. Verder worden de aspecten behandeld, die belangrijk zijn bij het kiezen van de juiste stent. Verder kan het plaatsen van een stent op het gebied van de stromingsleer bepaalde effecten vertonen: in en rondom de stent. Hier wordt onderzoek naar gedaan met in-vitro studies en numerieke stromingsleer (: in het Engels afgekort met CFD) om meer over de stromingsleer gerelateerde effecten te kunnen bestuderen.

Bij het uitvoeren van een in-vitro studie kunnen er problemen optreden. Stents zijn niet doorzichtig. Voor het analyseren van stromingen moeten de structuren in sommige gevallen doorzichtig zijn/worden gemaakt. Bijvoorbeeld wanneer PIV met behulp van optische technieken (lasers) wordt gebruikt.

In deze thesis onderzoeken we methoden om stromingen in ondoorzichtige structuren te visualiseren.

Allereerst hebben we gekeken naar optische technieken om laminaire stroming in een rechte buis te kunnen visualiseren. Dit wordt in hoofdstuk 2 in detail besproken. Voor het visualiseren van stromingsprofielen hebben we goede belichting, een camerasysteem en tracerparticles (die worden geïnjecteerd in de stroming) nodig. Deze tracerparticles moeten klein genoeg om de stroming te kunnen volgen. Het nauwkeurig volgen van de stroming wordt tracer fidelity genoemd. Al deze aspecten samen maken flow visualisatie mogelijk.

In onze experimenten hebben we flowvisualisatie gedaan met een techniek gebaseerd op waterstofbellen. Hierbij treedt elektrolyse van water op. Door het plaatsen van een dunne metalen draad in een buis en hier gepulseerd stroom op te zetten, worden waterstofbellen gecreëerd. Deze bellen vormen zogenaamde tijdlijnen. Door gebruikt te maken van deze tijdlijnen is op enkele foto’s een deel van een parabolisch flowprofiel waargenomen. Deze resultaten zijn gebruikt als eerste stap in onze flowexperimenten.

Hoofdstuk 3 behandelt de visualisatie van bellen met behulp van röntgenstraling. Röntgenstraling kan worden gebruikt om de inhoud van ondoorzichtige structuren in beeld te brengen. In dit deel van het onderzoek werden de bellen via dunne naalden geïnjecteerd in buizen gevuld met water. De resultaten lieten zien dat het moeilijk is om kleine bellen te visualiseren met behulp van röntgenstraling. Dit komt o.a. door de resolutie van het röntgensysteem en het minimale contrast tussen de bellen en het water.

Omdat we tijdens de experimenten steeds een snapshot hebben gemaakt, is alleen de positie van de bellen bekend. Voor het in beeld brengen van een beweging hebben we meerdere frames nodig. Om dit met röntgenstraling te kunnen doen, kunnen we gebruik maken van een shutter. Deze shutter kunnen we voor de röntgenbuis plaatsen. Met een shutter kan röntgenstraling worden geblokkeerd voor een bepaalde, vooraf gedefinieerde tijdsduur. Dit betekent dat timing essentieel is voor het maken van korte achtereenvolgende röntgenbeelden.

Voor dit onderzoek is er een shutter gebouwd, en deze is geplaatst voor de röntgenbuis. Echter, omdat de timing van de shutter nog niet optimaal was, is aanvullend onderzoek nodig om deze techniek verder te optimaliseren.

In het laatste hoofdstuk worden er andere parameters (de polsgolfsnelheid en de wandschuifspanning) kort behandeld met betrekking tot de bijbehorende meetmethodes, die gebruikt kunnen worden in in-vitro studies. Dit zijn o.a. algoritmes om de pulse transit time te verkrijgen, en daarnaast wordt ook de theoretische achtergrond behandeld.

Table of Contents

List of figures

List of Tables

List of symbols

Greek

δ	Boundary layer thickness
λ	Wavelength
μ	Dynamic viscosity / Attenuation coefficient
μ_f	Dynamic viscosity fluid
ν	Kinematic viscosity
ν_f	Kinematic viscosity fluid
ρ	Density
ρ_f	Density fluid
ρ_p	Density particle
τ	Relaxation time
τ_w	Wall shear stress

Subscripts

f	Fluid
p	Particle

Roman

A	Area
a	Acceleration
C_c	Slip correction factor
C_d	Drag coefficient
$C_{intensity}$	Intensity contrast
$C_{line-integral}$	Line integral contrast
C_{object}	Object contrast
C_s	Subject contrast
D	Hydrodynamic diameter
d	Depth / Tube diameter
d_p	Particle diameter
E	Elastic modulus
E_l	Entrance length number
F	Force
$F_{buoyancy}$	Buoyancy force
F_{drag}	Drag force
g	Gravitational constant / Scattering anisotropy
HVL	Half value layer
h	Wall thickness
I	Intensity
L_c	Characteristic length
L_{tube}	Tube length
l	Entrance length
m	Mass
P	Pressure

Q	Flowrate
Re	Reynolds number
Re_p	Particle Reynolds number
r	Radius / Radial position
r_i	Inner radius
r_p	Radius particle
St	Stokes number
s	Position
s_p	Position particle
T	Surface tension
t	Time
U_f	Fluid velocity
U_p	Particle velocity
u	Velocity
V	Instantaneous relative velocity
x	Size parameter

1 Introduction

1.1 Thesis introduction and main research problem

In the Netherlands, cardiovascular diseases are a major cause of death. In 2014, 38432 people (28%) died because of a cardiovascular disease.[4]

One of these cardiovascular pathologies is the aneurysm of the aorta abdominalis (AAA). In 2014, in the Netherlands 238 people (168 man and 70 women) died because of a ruptured AAA [4].

In order to understand the background of this pathology, we will first describe the normal structure of the aorta, followed by the pathophysiological mechanisms that occur in case of an AAA, subsequently corresponding treatment and complications.

The aorta consists of the lumen and the wall. The aortic wall can be divided in three layers: the tunica adventitia, tunica media and tunica intima (see figure 1).

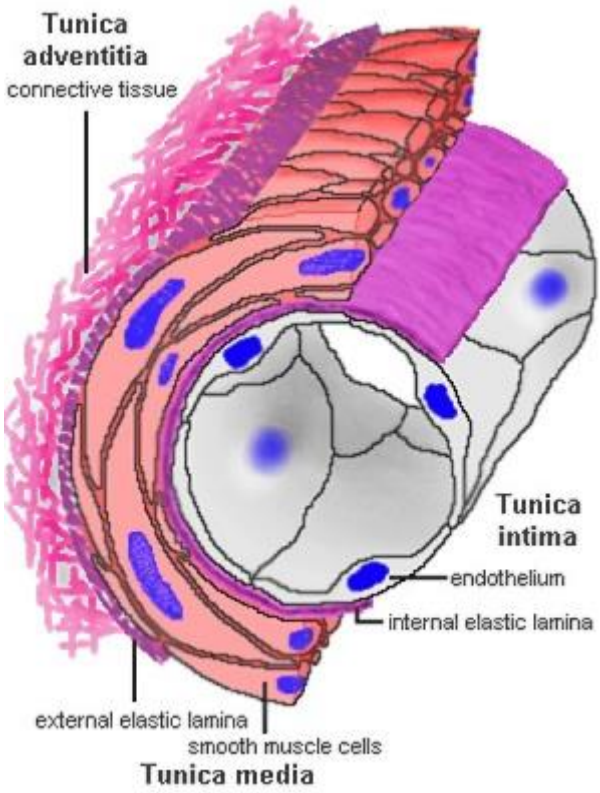

Figure 1: Taken from [5]: the different layers of a vessel wall (tunica intima, tunica media and tunica adventitia).

Each layer with its own components and function:

The adventitia is the outer layer of the vessel with mainly connective tissue, the media is the middle layer consisting of elastin, smooth muscle cells and collagen fibres and finally the intima consists of the endothelium layer and the internal elastic layer (not always clearly recognised). [5]

In elastic arteries, like the aorta, the subendothelial layer is thick and contains connective tissue, and also elastin in the case an onelayer internal elastic lamina is not present. [6] This thick subendothelial layer can also be seen in figure 2, taken from Toczek et al. [7].

The vessel wall consists of two keyproteins: collagen and elastin. In an AAA, proteins are affected by an inflammatory response. The matrix metalloproteinases (MMP's) are likely for a part responsible for this process. These MMP's digest the extracellular matrix and elastin, which stimulates the inflammatory response and changes the structure of the arterial wall. [8]

More recently, a paper was published about the current insights in the pathogenesis of the aorta abdominalis, focusing on the biochemical aspects of the AAA. [9]

In figure 2, taken from the paper of Toczek et al [7], a schematic overview of the development of an aneurysm is shown. Here, the different stages are summarised from left (normal) to right (rupturing when the wall stress is higher than the tensile strength). This strength is low at locations where these type of reactions, like in figure 2, occur. Also, it is seen that the media becomes thinner. [7]

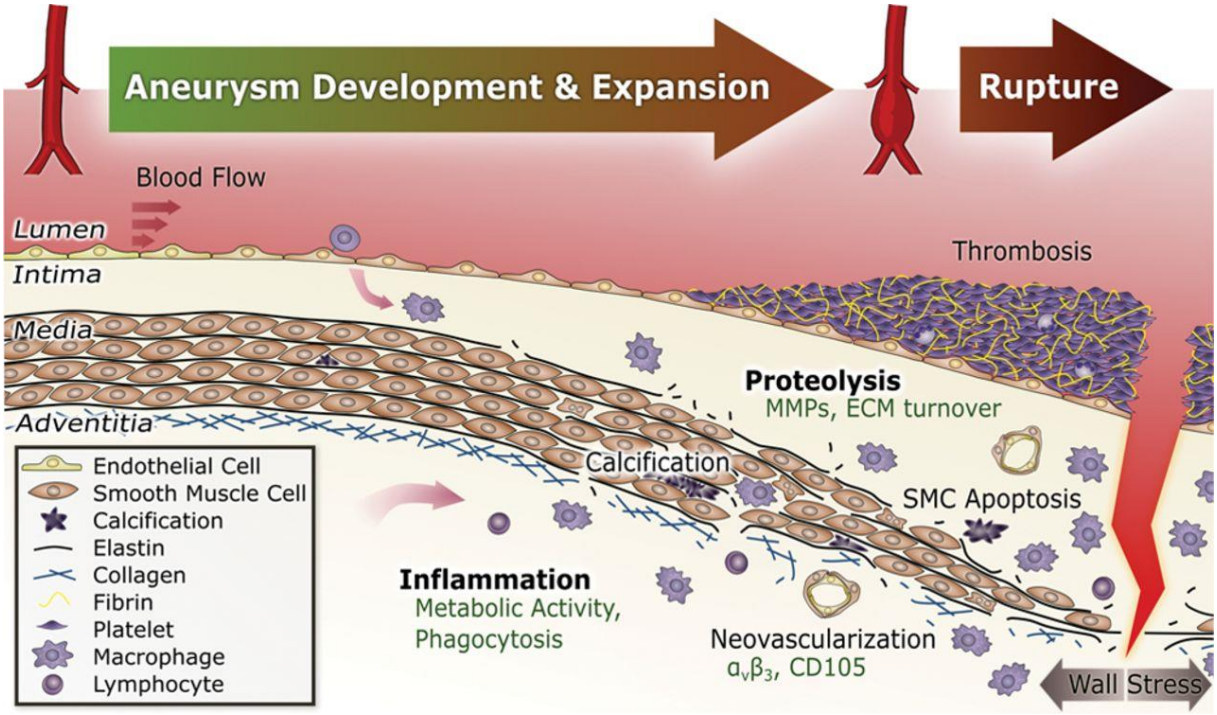

Figure 2: Taken from figure 3 of Toczek et al. [7]: showing the different stages of an AAA.

The phenotype of this pathology is a local dilatation of the aorta of at least 50% of the nominal diameter, which untreated may result in a rupture of the aorta.[10]

Patients, with an AAA, can complain about asymptomatic pain in the abdomen or about pain in the back. These are reasons for doing palpations and/or ultrasound imaging. Ultrasound imaging can be used for analysing the aorta abdominalis. With this imaging modality, it is also possible to measure the diameter of the aorta.[11]

In literature, a diameter of 5.5 cm for men and 5.0 cm for women is considered as threshold for intervention, because of the increased risk of rupturing the aorta. [12] This threshold is partly based on the Laplace law, where the relation between diameter and stress in a tube is defined [13], and on clinical experience.

For a circular tube (e.g. aorta), this law can be described as in equation (1.1) [14]:

$$T = \frac{P \times r}{2 \times h} \tag{1.1}$$

Where: P= transmural pressure; h= wall thickness; T= wall tension; and r=radius. [14]

This means that in case of an aneurysm, where r is already higher than normal less pressure is required to exceed the surface tension of the wall. This is the reason why vessels with a high diameter require screening and if necessary a vascular intervention. [14]

However, we see in literature that also people with a smaller diameter (than the mentioned threshold) died because of a rupture of the aneurysm and that in some other people with a diameter higher than 5.5 cm rupturing did not occur.[15] This is one of the reasons why the 5.5 cm threshold is under discussion, for example by Kontopodis et al. (2016) [13] and in the review of Vorp et al. [15]**.** Other factors are considered to give a prediction of the rupture risk. In papers for example wall stress and diameter are compared [16] [17], or even with the rupture potential index (RPI) included [18].

A Rupturing of the AAA

Rupturing of the aneurysm results in an internal bleeding and pressure loss, which can cause death if surgery is not done immediately. After surgical repair of a ruptured aneurysm the mortality rate is approximately 50 percent in hospital [19].

Within the western world rupture of aortic aneurysms is the thirteenth leading cause of death. [10] Therefore, much research is drawn into this area. Some examples are already mentioned above.

Besides the rupture estimation, also the anatomical location at the aorta is important for the type of treatment which is necessary. For some types of aneurysms at the thoracic part and abdominal part of the aorta, this can done for example with the Crawford classification. [10]

These are a few of the factors that determine the treatment options for an AAA.

B Treatment options for an abdominal aneurysm

In this part, we start with defining the surgery options together with some historical background.

For treating aneurysms two main procedures are possible:

1) Open aortic repair: this is conventional surgery for placing a vascular prosthesis at the site of the aneurysm (see figure 3). [20]

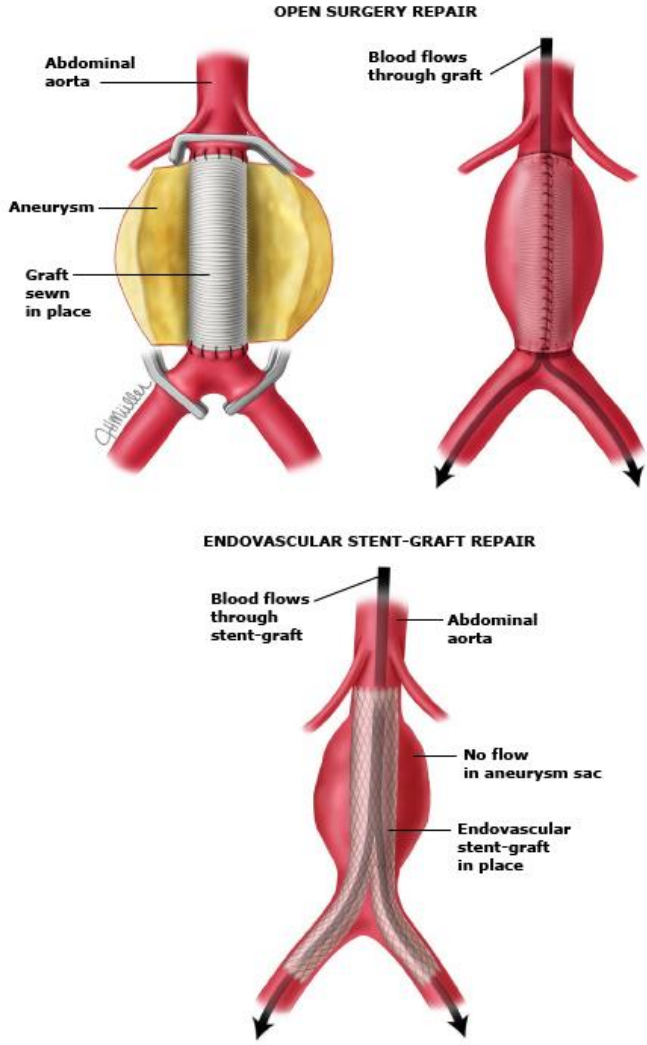

Figure 3: Taken from figure 2 of [20]: showing the difference between open repair and endovascular repair.

Einstein was operated in 1948 because of an AAA by the surgeon Nissen (who published about the Nissen fundoplication [21]). This was done by placing cellophane around the aneurysm. The idea of this technique was that by causing a foreign body reaction and the fibrosis forming the aneurysm would stabilise. On 18 April 1955 Einstein died of the ruptured aneurysm.[22]

In 1950, Dubost repaired an AAA by placing a human homograft.[8] This was the first open repair of an AAA [3].

The open procedure can be initiated by a left retroperitoneal approach or median laparotomy. When the proximal and distal ends of the aneurysm are clamped, a tube graft is placed. The aneurysm is not excluded, because otherwise the graft may come in contact with the duodenum, which may

result in fibrosis and an aorta-enteric fistula. In order to avoid these reactions the aneurysm “covers” the graft. [11] This can also be seen in figure 3.

2) The second type of repair is the endovascular aneurysm repair (EVAR) [3]: surgical procedure via the femoral arteries (endovascular) to place a stent graft at the location of the aneurysm [20].

In 1991, Parodi et al. first reported the placement of an endoprosthesis via the femoral aorta in five patients [23]. From that moment, the EVAR procedure was further developed with different kind of stent grafts for patients with an AAA. We can see this back in the number of stent grafts available nowadays [1].

In the EVAR procedure a guide wire is placed in the iliac artery at the ipsilateral side, where the main body of the stent graft is directed in. The other side (contralateral) is used for the angiography. Sealing is done infra- or suprarenal. After this, the contralateral limb is directed through this side. Sometimes a cross over approach has to be used. After fixation/sealing by a balloon expansion, angiography is done for checking the stent graft functionality, where the physician looks for things, like endoleaks.[11]

Nowadays, more people are treated with EVAR than with open surgery. This can be seen for example in the annual report of the Dutch Institute for Clinical Auditing (DICA), where statistics of the Dutch Surgical Aneurysm Audit are published. [24]
In the Netherlands in 2016, 77 percent of the patients, treated with elective surgery, were operated with EVAR. In 21 percent open surgery was done and in 0.4 percent EVAR was changed to open repair during the intervention. In other situations, like in the case of rupture, open surgery is done more. However, this is a small part compared to the total number of treatments done in an elective setting. [24]

C Complications

As we have already seen, there are some parameters to estimate the rupture risk for an AAA. Also for the outcome of surgery there are different prediction tools for example the Glasgow Aneurysm Score. This score implements other pathologies the patient may suffer, which may give additional risk for mortality. These are factors like: myocardial disease, renal disease and cerebrovascular disease. The score is calculated with the following formula: GAS=(age + [7 points for myocardial disease] + [10 points for cerebrovascular disease] + [14 points for renal disease]).[25]

In study of Baas et al. (2008) the 30-day mortality and two-year mortality with GAS were compared for the open and endovascular repair[25]. For open surgery the optimal GAS-value found was 75.5 and for EVAR 86.5. The conclusion of this paper is that GAS can be used as predictor for both interventions. However, for people who can be operated with both interventions, it is a better outcome predictor in EVAR**.**[25]

In the directive of 2009 for diagnostics and treatment of an AAA in the Netherlands it is stated to include these kind of tools (like the GAS) when indicating an open operation, mainly for patients with a good prognosis. [26] The GAS was originally developed for open surgical repair [25].

For the open procedure the 30-day mortality in the UK is reported in the review of Duffy (2015) between 2 and 12 percent. [19]

However, these two statements about using GAS look not in accordance to each other and might need some further explanation. One reason can be the time between publishing both sources. Finding these reasons is not the goal of this report, therefore we will not discuss this here in more detail.

Finally, besides these (positive) statements about using these scorings systems, cautions are also mentioned in literature. These are related to the accuracy and reliability of these models. [27]

From this point on we will focus on EVAR. As already mentioned, the number of EVAR procedures is higher than for open repair. And also, in open repair the average number of complications and mortality is higher than in the case of EVAR. [24]

For abdominal aneurysms different stent grafts may be used. These consist of a graft of ePTFE or woven polyester and skeleton of nitinol or stainless steel. [1]
ePTFE stands for extruded polytetrafluoroethylene and is used for many purposes, because of its divers properties like biocompatibility, high strength, lightweight, low porosity/high porosity and UV resistance. [28]
Polyester is also used in many industries, like for clothing etc. Both materials are often used as graft material. [29], [1].
Nitinol is biocompatible and superelastic, has corrosion resistance and shape memory. Meaning that it can be used in the EVAR procedure: it becomes deformable at body temperature when it comes at the site of the aneurysm. This property is used in the self-expanding nitinol stent. [29]

An overview of the recent stent grafts can be found in table 1 and table 2, both are taken from Schoretsanitis et al.[1].

Choosing the right type of stent graft is equally important as the procedure itself for a successful outcome for the patient. Errors in preparation or during surgery may cause short or long-term complications.

Endoleak

Endoleak is one of these complications. Endoleaks can be divided in five types. The different definitions can be found in the paper of Rand et al. [30]:

-Type I: Caused by the sealing failure on the proximal or distal side of the stent graft. [30]

-Type II: Caused by retrograde flow in the aneurysm sac which can come from collateral vessels: like the inferior mesenteric and lumbar arteries. [30]

-Type III: Caused by disconnection of the modulus of the stent graft, or likewise problems. [30]

-Type IV: Caused by porosity of the stent graft, which is detected within 30 days after the intervention. [30]

-Type V: Caused by the so-called endotension: pressurisation of the aneurysm sac without finding any of the above-mentioned causes (type I to type IV). [30]

Graphically these type of endoleaks can be seen in figure 4, taken from Erbel et al. [11].

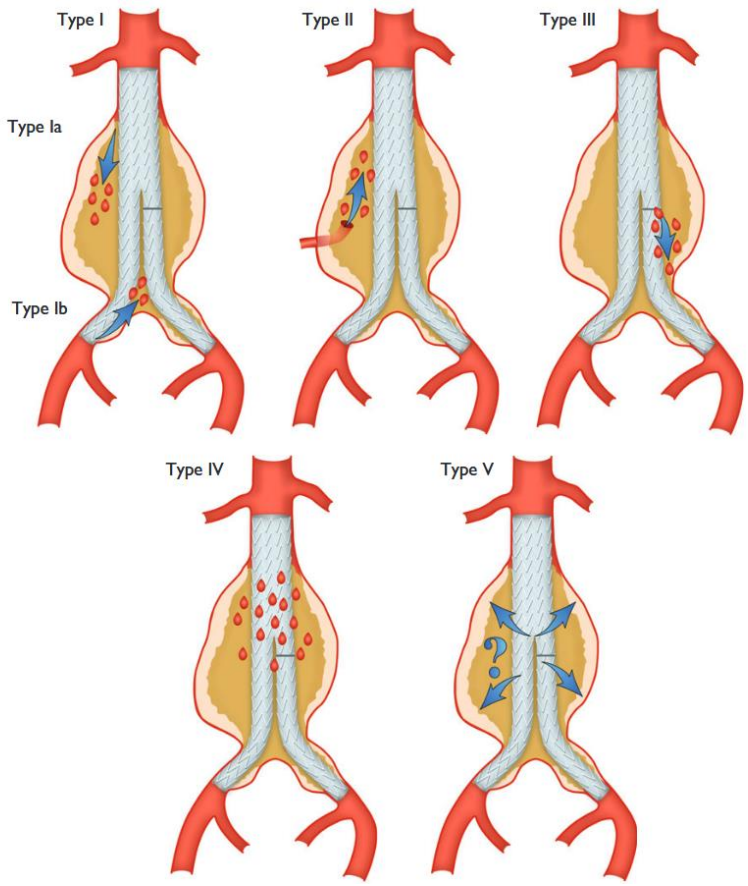

Figure 4: Taken from [11]: Showing the different types of endoleaks.

These type of endoleaks can only occur at EVAR, because at the open surgery repair the aneurysm is removed and subsequently, a vascular prosthesis is sewn to both ends of the aorta. [10]

The stent grafts, used in EVAR, can be divided based on different properties, for example balloon-expandable stent grafts (BES) vs. self-expandable stent grafts (SES). [1] [31]

Based on these properties also other complications can occur, like dilation of the infrarenal neck. Some stent grafts (SES) exerts continuously a radial force to the vessel wall. In the study of Savlovskis et al. BES and SES were compared. It was found that in patients with a SES infrarenal dilation occurs in greater extent than in patients with BES. [31]
However, in the paper of Oberhuber et al. this is not mentioned as main cause, because also dilation in open repair is seen. The authors suggest, it is a combination of different factors.[32]
We have to note that the paper of Savlovskis was published several years later. SES might have a higher influence than BES, but more factors look responsible, looking at both papers [31] [32].

Migration

Also, migration of stent grafts is mentioned in literature as complication after placing a stent graft [33]. Recently, in 2016 Antoniou et al. published a case report, where Nellix stent migration is discussed [34]. One of the causes of migration in stent grafts, mentioned in the paper of Resh et al., is dilatation of the infrarenal neck [35]. The authors suggest better proximal fixation of the stent graft and is discussed in more detail in their paper [35].

We can see in table 1 that the fixation method varies for the different stent grafts, meaning that also the change of migration of the stent grafts differ.

Mechanical failure of stent grafts

The last aspect we will shortly mention, is the mechanical failure of stent grafts.
In 2003, Jacobs et al., looked extensively to mechanical failure of stent grafts, such as abdominal stent graft wear holes, suture disruption [36].
By analysing these failures, more knowledge is gained about them. However, we see also that in this period after 2003 mechanical failures occur. A recent example, where a stent graft complication is discussed, is the case report of Kansal et al. where a type IIIb endoleak is mentioned. This shows the importance of surveillance after placing a stent graft. [37]

A type III endoleak can be repaired by placing an aorto-iliac endograft within the other graft and femorofemoral bypass [38].

In new developed stent grafts these mechanical issues might also occur, which may cause also fluid mechanical effects. For example, one issue mentioned in literature is occlusion of the kidney arteries by migration of the stent graft [39].
Also because the fact that Jacobs et al. reported that 19 months was the average period for detecting these mechanical issues [36], surveillance is important.

D Different Stent grafts

In table 1 and table 2, taken from Schoretsanitis et al.[1], we can see some of the most recent stent grafts used for the endovascular treatment of an AAA.

Table 1: taken from [1]: different stent grafts composed of different materials.

Endograft type	Device structure	Fabric and skeleton	Fixation mode
Excluder C3 (Gore associates)	Modular-bifurcated	ePTFE and nitinol	Active infrarenal fixation with anchors
Endurant II (Medtronic)	Modular-bifurcated	Woven polyester and nitinol	Active suprarenal fixation with pins
Endurant IIs (Medtronic)	Modular-three pieces	Woven polyester and nitinol	Active suprarenal fixation with pins
Zenith LP (Cook Medical)	Modular-bifurcated	Woven polyester and nitinol	Active suprarenal fixation with barbs
Zenith Flex (Cook Medical)	Modular-bifurcated	Woven polyester and nitinol	Active suprarenal fixation with barbs
Treovance (Bolton)	Modular-three pieces	Woven polyester and nitinol	Double active fixation (suprarenal and infrarenal)
Incraft (Cordis)	Modular-three pieces	Woven polyester and nitinol	Suprarenal with barbs
Anaconda (Vascutek)	Modular-three pieces	Woven polyester and nitinol	Active infrarenal fixation with hooks
E-tegra (Jotec)	Modular-bifurcated	Woven polyester and nitinol	Active suprarenal with anchors
Aorfix (Lombard)	Modular-bifurcated	Woven polyester and nitinol rings	Helical circular nitinol frame and hooks
AFX (Endologix)	Unibody	ePTFE and cobalt chromium alloy	Anatomical fixation onto the aortic bifurcation
Ovation (Endologix)	Modular-three pieces	PTFE and nitinol	Active suprarenal fixation with anchors and seal through polymer-inflatable rings
Nellix (Endologix)	Two balloon-expandable stents surrounded by polymer-filled endobags	PTFE and cobalt chromium alloy	Anatomical sealing in the AAA sac

Table 2: taken from [1]: different stent grafts with their main properties, IFU: instructions-for-use.

	Neck length (mm)	Neck diameter (mm)	Neck angulation (°)	Distal fixation length (mm)	Iliac diameter (mm)	Main body sheath size (Fr)	Limb sheath size (Fr)
Excluder C3	≥15	19–32	≤60	≥10	8–25	16–18	12–15
Endurant II	≥10	19–32	≤60 if neck length 10–14 mm <75° if neck length >15 mm	≥15	8–25	18–20	14–16
Zenith Flex	≥15	18–32	Infrarenal ≤60; suprarenal ≤45	≥10	7.5–20	18–20 (ID)	14–16 (ID)
Aorfix	≥20	19–29	≤90	≥20	8.5–19	22	20
AFX	≥15	18–32	≤60	≥15	10–23	17	9
Anaconda	≥15	16–31 (17.5–31 for Anaconda One-Lok)	≤90	≥20	8.5–21	20–22	18
Treovance	≥10	17–32 with neck length ≥10 17–30 with neck length ≥15	≤60 if neck length 10–14 mm <75 if neck length >15	≥10 with diameter 8–13 ≥15 with diameter 14–20	8–13 if iliac length ≥10 14–20 if neck length ≥15	18–19	15–16
E-tegra	≥15	19–32	≤75	≥15	8–25	18	16
Incraft	≥15	20–27	≤60	≥10	9–18	14	12.5
Ovation	–	16–30 at 13 mm IR[a]	≤60 if neck ≥10 mm ≤45 if neck <10 mm	≥10	8–25	14	14
Nellix	≥10	18–32	<60	?	8–35	17	17

The IFUs for all aortic stent-grafts appear as described in published articles and studies in the literature

[a] IR; infrarenally (below the lowest renal artery)

As we can see in both tables the different stent grafts have different parameters, which make it important for the vascular surgeon to make the right choice based on the patients anatomy.

In the European Society of Cardiology (ESC) Guidelines of 2014 with regard to aortic diseases [11], these parameters are also partly discussed:
For an EVAR the aortic neck should have a minimum length of 10 to 15 mm and a maximum diameter of 32 mm. In case the angulation is higher than 60 degrees, there is an increased risk in endoleaks and migration. Furthermore, the iliofemoral part to the aneurysm should be studied because of the parts needed to get the stent graft at the position of the aneurysm.[11]
Further, we can imagine each stent graft has its own advantages and disadvantages.

In the dissertation "Endovascular Aortic Repair : Clarifying risk factors, complications and follow-up strategies" (2015) from Gonçalves different stent grafts with the main complications are discussed [40].

We will discuss some of these stent grafts based on the review of Schoretsanitis et al. [1],because this is published most recently.

Nellix: this is a stent graft with two extendable balloons for fixation at the aneurysmatic sac, mentioned as endovascular aneurysm sealing (EVAS), to avoid endoleak type II. Often in the other stent grafts fixation occurs supra- or infrarenal. Long term follow-up is not available until now. [1]

Endurant II: this is a modular bifurcated stent graft which is fixated suprarenal. In patients with short and angulated proximal necks, it should able to resist migration better by the anchoring pins.
It is stated in the review of Schoretsanitis et al. that this is the most studied stent graft in literature. [1]

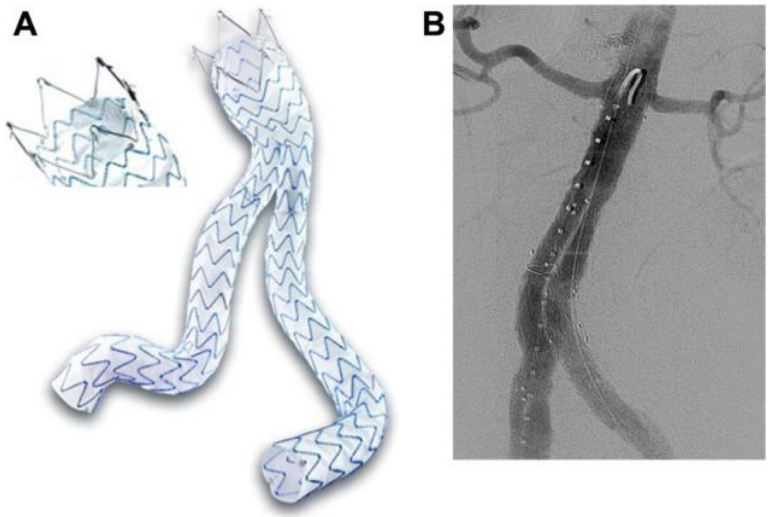

Figure 5 Taken from [41]: The Endurant II stent graft (left) and aortogram with the stent graft (right).

Anaconda: this is a stent graft device, existing of three pieces. At the upper part it consists of two nitinol rings for fixation, the main body is unsupported and the limb parts consist of a nitinol stent. The gives the stent graft its flexibility. [40]

Figure 6: Taken from [40]: Anaconda system

These different stent grafts can be studied by computational fluid dynamics (CFD) or experimentally: in-vitro/or in-vivo.

E Relevant aspects in stent graft design

The design of a stent graft is important for the long-term performance, when the stent graft is implanted in a patient who suffers from a vascular disease. The design aspects are for example the type of material, stent strut thickness, the spacing between the struts, fenestrations etcetera.

In the paper of Moore and Berry from 2002 these aspects are discussed. The main points of interest discussed were for example [42]:
-compliance mismatch between the stent graft and the vessel
-the stress the stent exerts on the vessel wall and its mechanical and fluid mechanical influence on the vessel.
-the stent strut spacing, responsible for backward and forward facing steps, which results in flow separations
[42]

Some background about backward facing steps can be found in the paper of Biswas et al. [43], forward facing steps are for example discussed in Shao et al. [44] and Iftekhar et al. [45]

The stent design can influence processes like thrombus forming and restenosis. [42]
A recent example of a stent graft design using CFD is the model developed at Sanford Health.[46] In the paper published in 2016, the authors describe a CFD model which simulates blood flow. And the response of blood flow of a proposed stent graft design is investigated. Here streamlines were computed using different configurations, see figure 7. [46] These diaphragm pitches are the angles with respect to the normal.

Diaphragm pitch	0 degree	20 degree	40 degree
Particle streamlines	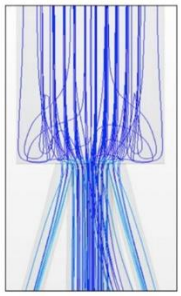	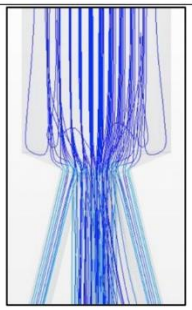	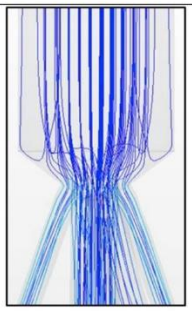

Figure 7: Taken from [46], velocity streamline at different diaphragm pitches

Also material combinations, stents and grafts, were tested for optimal stent graft lifetime.
In the paper of Kleinstreuer et al. (2008) nitinol stents were analysed. Here, different nitinol types (NITI1 and NITI2) were tested with graft materials ePTFE and polyethylene terephthalate (PET), looking at material fatigue and compliance. [29]

Studies looking at mechanical and fluid dynamics in stent grafts

One can imagine that placing a stent graft at the location of an aneurysm implies, that the aortic bifurcation will be shifted more proximal in the direction of the renal arteries.
In the study of Walsh et al. (2003) these implications are analysed in a glass model of the aorta. Furthermore, it is discussed that in rest at the level of the kidney vortices (as periodic patterns) may occur due to the fact that 25 percent of the flow goes via the renal arteries and the flow also is decelerated during diastole. Placing a stent graft and therefore shifting the aortic bifurcation can change these flow patterns in rest and during exercise (in which case less blood will flow in the renal arteries).[47]

The conclusion was, however, that the aortic flow pattern did not change, by placing a Cordis stent graft, much due to this displacement[47]. Other stent grafts may result in different outcomes. These can be analysed with a different flow visualisation technique with currently on the market available stent grafts.

Also in-vitro studies are done in the past to analyse the flow patterns, with laser Doppler anemometry (LDA). For example in the paper of Chong and How (2004), the flow patterns were analysed for a NiTi stent where the opaque part was replaced by a transparent model of polyurethane.[48]

This means original fabricated stents have to be modified for LDA measurements. Because the properties may be altered by this process, alternative imaging techniques are favourable above the LDA technique for measuring inside stent grafts.

These studies show different aspects are important when checking the performance of stent grafts in vitro and in-vivo. Currently, it is difficult to visualise the flow patterns in stent grafts without changing the opaque structure/affecting the (fluid)mechanical properties.

Analysing flow patterns in opaque structures requires a detailed analysis without changing the stent graft configuration. This should give more insight in the performance of stent grafts under different physiological conditions.

We can think of effects in patients with an irregular cardiac rhythm (during exercise), effects of hypertension on the flow in the stent grafts and in the different branches. And besides different physiological conditions, also anatomical variation can be simulated in in-vitro models to study their influence on the flow inside stent grafts.

As we already mentioned, there is much interest in the effects of stent grafts on flows in arteries, but there is not much published about clinical imaging techniques for looking at flows inside stent grafts. In this thesis, we will focus on whether it is possible or not to use X-ray imaging for visualising flows in opaque structures, like for example stent grafts. We will build/develop a proof of concept by looking at particles that are visualised, which can represent some flow properties. But before this, we look first at: building an experimental set-up for optical based Particle Image Velocimetry (PIV), which is a more regular flow visualisation method.

We start with a PIV method that captures hydrogen bubbles as (tracer) particles, based on their optical properties. Subsequently, if we succeed with this method to visualise some flow profiles with optical techniques, we try to use the same type of particles; this time using a different imaging modality: X-rays instead of photons in the visible spectrum. With this in mind, we could extrapolate these results for imaging flow profiles in opaque structures.

Before we discuss these experimental techniques, some background information of fluid mechanics is desirable to understand the choices made, in regard to the defined requirements used in this thesis.

1.2 Some of the basic aspects of fluid mechanics

Fluid mechanics describes and analyses the behaviour of fluids inside or around structures. Examples include pipes, airfoils, building, and blood vessels. By studying these behaviours for example inside arteries (or models of arteries), more insights can be established into influence of blood flow alterations (for instance on the vessel wall) and specific treatments.

A particular example is the blood interaction with the vessel wall (fluid-solid interaction), resulting in particular velocity profiles and analysing their relation with shear stress and wall shear stress.[49] [50] The last one depends on the properties of the vessel (its elasticity, roughness, etc.).

For understanding the main aspects of this thesis, first an introduction will be given where the main fluid dynamic aspects, like the types of flow and flow properties, will be explained. With this in mind the reader will able to clarify some aspects mentioned in this thesis. However, the goal of this thesis is not give a quick course in fluid dynamics.

We start with some definitions.

The shape of liquids can be changed without any real force in contrast to solids. The parameter that describes changing the rate of change is called *viscosity*. The fluids with high viscosity have a resistance for changing its shape (in motion). [51]

The flow of fluid can be categorised based on the so-called *Reynolds number*. This is a dimensionless number which is the ratio between the inertial and viscous forces and can be calculated as follows [52]:

$$Re = \frac{\rho u^2}{\mu \frac{u}{L}} \tag{1.2}$$

which can be rewritten as Re=$\frac{uL}{\nu}$. The parameters used are: u: the velocity in m/s; ρ: the density in kg/m³; μ: the dynamic viscosity in Ns/m²; L is the characteristic length in m and ν is equal to $\frac{\mu}{\rho}$ in m²/s. For a tube with a fully developed flow (FDF), see the definition later on in this paragraph, L is the hydraulic diameter. Re lower than 2300 is laminar flow; between the 2300 and 4000 the flow is transient, and with Re higher than 4000 the flow is turbulent. [52]. Be aware that μ in the case of X-ray physics is the attenuation coefficient (see chapter 3).

In case of steady FDF flow in a pipe the flow profile gets a parabolic shape. The flow can be described by a certain velocity profile, which describes the velocity at different locations in a pipe from the center to the wall of the pipe. The formula, which is called the law of Poiseuille, is described as [53]:

$$u(r) = (\frac{\Delta P}{l})(r_i{}^2 - r^2)/4\mu \tag{1.3}$$

where r_i: the internal diameter and r: distance from the center of the tube in radial direction

[53]

And:

$$\Delta P = \frac{8\mu L_{tube} Q_{tube}}{\pi r_i^4} \tag{1.4}$$

where L_{tube}: the length of the tube; and Q_{tube}: the flowrate

[53]

We will take an example based on the flow, measured in the paper of Cheng et al., during exercise at the infrarenal level of the abdominal aorta for men: 5.9 L/m. [54]

We choose to calculate the velocity profile of water in a tube with a length of 1.5 m and a radius of 1.3 cm. The reason for using this length and tube radius is because this was the same order of magnitude used in our experiments (see later on).

- ➔ $\mu_{water} = 1.002\times10^{-3}$ Pa.s [52] ; $L_{tube} = 1.5$ m ; $r_i = 0.013$ m and
- ➔ $Q_{tube} = \frac{5.9\times10^{-3} m^3/min}{60}$=$9.8\times10^{-5}$ m³/s

Using equation (1.4) gives:

$$\Delta P = \frac{8\times1.002\times10^{-3}\ \text{Pa.s}\times1.5\ \text{m}\times9.8\times10^{-5}\ \text{m}^3/\text{s}}{\pi\times0.013^4} = 13.2\ \text{Pa}$$

In figure 8, the corresponding velocity profile is shown.

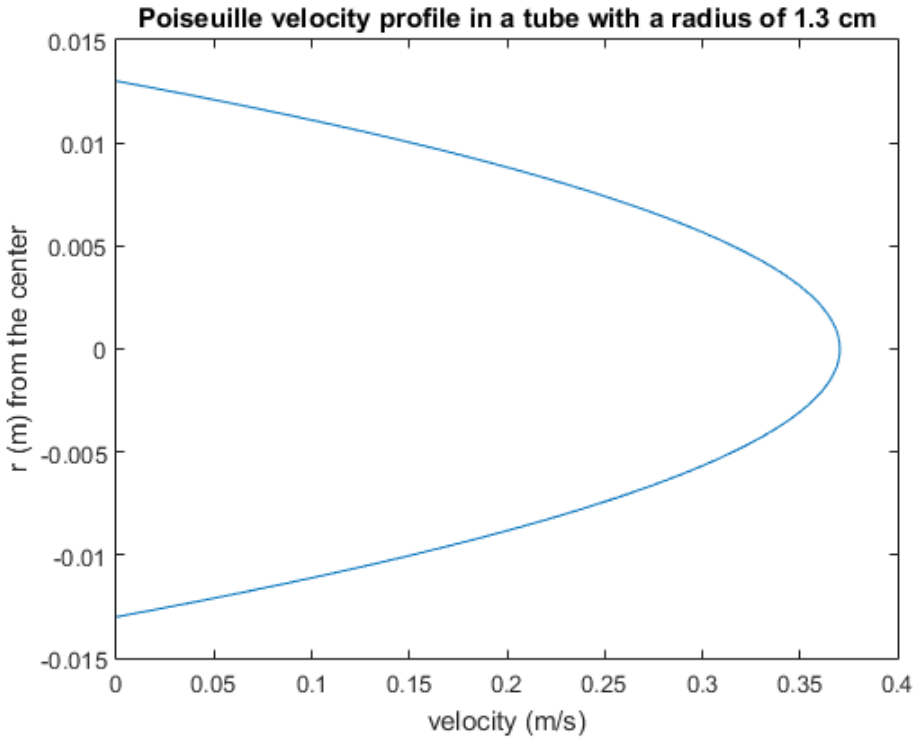

Figure 8: Velocity profile in a tube with a Poiseuille flow and a volumetric flow rate of 9.8×10^{-5} *m³/s (caused by a pressure difference).*

Flows are categorised by the Reynolds number. Fluids can be described based on properties as dynamic viscosity (μ) or kinematic viscosity (ν). (Dynamic) Viscosity is related to the shear stress between different layers of fluid. This can be seen in the formula of shear stress (τ): $\tau = \mu\frac{du}{dy}$ where du is het unit velocity in m/s; $\frac{du}{dy}$ can be replaced as γ which is the shear rate in s^{-1}. Fluids, where this relation is linear, are Newtonian fluids. When this is not the case, the fluid is non-Newtonian. Dividing the dynamic viscosity by the density gives the kinematic viscosity.[52]

As fluids flow through a pipe some pressure loss will occur, which can be approximated by the Darcy-Weisbach equation. One of the parameters involved is the friction factor. This friction factor can be found in the Moody diagram (see figure 9). [55]

In the Moody diagram, the relation is shown between the friction coefficient λ and the Reynolds number Re, see figure 9. For laminar flow, there is a linear relation between both, i.e. the slope of the line $\lambda = \frac{64}{\mathrm{Re}}$. [52]

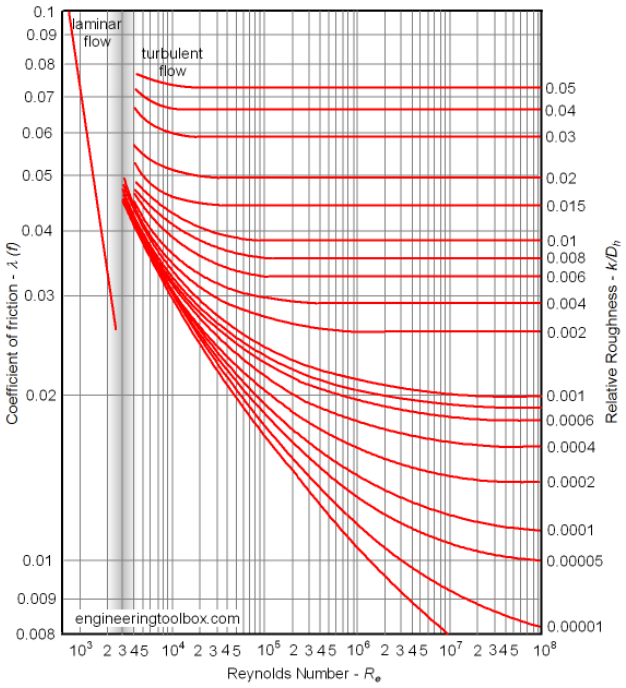

Figure 9: Moody diagram taken from [55]: showing the relation between Reynolds number, roughness and the friction coefficient.

The velocity profile (like figure 8) needs length to develop. This is the entrance length and for laminar flows can be calculated with:

$$E_l = \frac{l}{d} = 0.06\,Re \tag{1.5}$$

Where E_l: entrance length number; l: entrancelength; and d: tube diameter

[52]

We will focus us mainly on the laminar flow during the experiments. Experimental studies for this type of flows can be done with flow visualisation.

For instance analysing Poiseuille flow is important with use of catheters and their diameters. [56] [57] This shows that laminar flows are of interest in clinical research.

Also studying flow visualisation with pulsatile flows gets more interest, especially in the hemodynamics [58, 59] [60]. It is hard to implement and draw conclusions from studying these flows. In this study, we will use an optical PIV technique to visualise a laminar flow profile. The final goal is to develop a method where (tracer)particles, also in opaque structures, can be visualised.

2 Optical PIV technique

2.1 Introduction optical flow visualisation

Why optical techniques

For determining flow properties, Particle Image Velocimetry (PIV) is one of the techniques to visualise a flow field. The technique uses seeding particles, which visualise the flow, and an image capturing system and some illumination (a laser for example). The basic idea is that the particles are illuminated in a specific plane and the camera records the travelling of these seeding particles. Between different frames the displacement can be measured and from that data the flow field can be derived. In order to measure the displacements of the seeding particles the time-interval between the frames has to be short enough.[61]

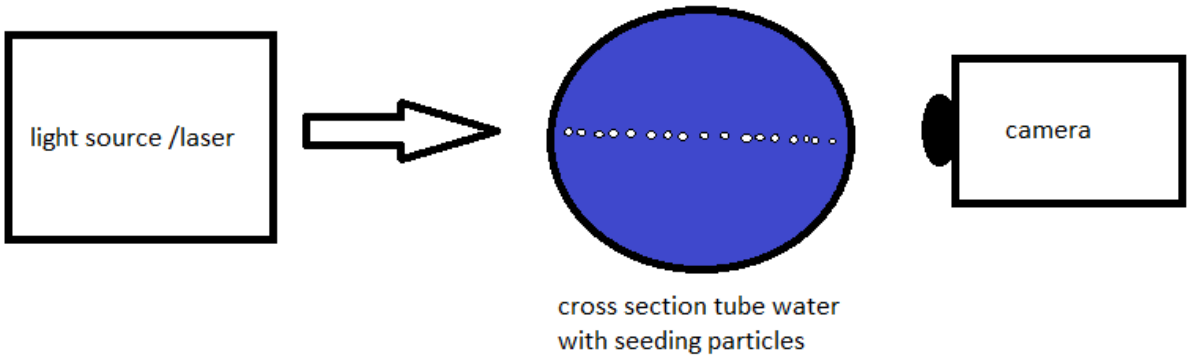

Figure 10: Simplified schematic model PIV system with the flow in the direction out of the paper, where the camera has a (small) angle to see the bubble line.

Because the optical flow visualisation requires not always very expensive materials, (see the paper of Schraub et al. [62] vs. the use of expensive lasers [61]), and the method is simple to implement, it is our first step using flow visualisation.

Depending on the application different seeding particles must be used. A variety of particles is available. For example, flow visualisation with milk and fluorescent dye (process referred as LIF (Laser-induced-fluorescence) is possible [63]. Also normal dyes are used [64]. However, these cannot be used with X-ray imaging. We will look at bubbles which can be visualised also by X-ray machines. A practical example is looking at air embolisms [65], [66].

In the paper of Schraub et al., a setup for hydrogen bubble tracer particles is described with the most important considerations and requirements [62]. Davis and Fox have evaluated this technique further [67].

The hydrogen bubble method is a flow visualisation method, based on the electrolysis of water. It is used by placing a thin metal wire in the object where fluid is flowing. An electrical pulse is send to the wire, inside the fluid, causing electrolysis of water (in the case water is “the working fluid”). Here the formed hydrogen bubbles will be pushed from the wire by the flow passing the wire. Recording these travelling bubbles in the flow by imaging with a camera, is in short the hydrogen bubble technique for flow visualisation. Also, is stated that the velocity error is small, by illustrating that bubbles generated by an 0.0006 inch wire reach free stream velocity after 70-wire diameters.[67] This velocity error is discussed later on this chapter.

The electrolysis of water occurs at the cathode and anode. First, we have to notice that water is in equilibrium with hydron (H^+) and hydroxide (OH^-). [68]

$H_2O(l) \leftrightarrow OH^-_{(aq)} + H^+_{(aq)}$ [68]

During electrolysis, the reaction at the anode (positive electrode) is:

$4OH^-_{(aq)} \leftrightarrow 2\,H_2O\,(l) + O_2(g) + 4e^-$ [68]

At the cathode (negative electrode) this reaction is:

$2H^+_{(aq)} + 2e^- \leftrightarrow H_2(g)$ [68]

For the hydrogen bubble flow visualisation this means we focus us on the cathode for the bubble production.

2.2 Goals/problem setting:

The first research goal is to visualise a laminar flow profile with tracer particles that eventually can be used for visualising flows in opaque structures. Establishing this goal requires in the first place some understanding regarding to tracer fidelity and scattering. These will be discussed in the next paragraph together with the requirements, distilled out by discussing these properties.

2.3 Requirements

2.3.1 Tracer fidelity

In this paragraph, we will discuss tracer fidelity. We will do some assumptions to obtain an indication for the order of particle diameter necessary for our experiments. We will do this by discussing the relation between particle diameter and tracer fidelity.

A: Optical tracer particles

First of all, we have to assume that tracers are suspended in some kind of flow where there will be a difference in the velocity of the tracer particle U_p and the surrounding fluid U_f. This is called the instantaneous relative velocity $V = U_p - U_f$. The motion of this (tracer) particle can be described by the Basset equation. This is a partial differential equation, where different forces on the tracer particle are described (see Appendix I). The different elements mentioned in the formula are: acceleration force, viscous resistance, force due to a pressure gradient near the particle, resistance of an inviscid fluid due the particle acceleration and the resistance caused by the unsteady flow field.[69]

Our working fluid is not inviscid, meaning the terms describing those effects can be neglected.

The equation of motion, mentioned in the paper of Melling [69], is based on Newton's second law of motion .

In the paper of Davis and Fox (1967), this equation of motion is simplified for 1-dimensional motion in the form of:

$$\left(\frac{4}{3}\pi r^3\rho_b + \frac{2}{3}\pi r^3\rho_f\right)a_p = 6\pi\mu r(U_f - U_p) \qquad (2.1)$$

Where: a_p: the acceleration of the bubble; and r: particle radius

[67]

This is on the left side of the equation the second law of Newton with an added mass implemented. These terms should be equal to the drag force (see later on in this paragraph).

The added mass term can be described in terms of inertia. When a body moves through a fluid the fluids reacts by changing the inertia of the travelling particle in that fluid. For the full derivation of the added mass in the case of a spherical particle, the reader is referred to the book Theoretical Fluid Dynamics of Shivamoggi. [70]

In the paper of Davis and Fox an expression of U_p is made by rewriting formula (2.1):

$$a_p = \frac{18\mu(U_f - U_p)}{4r^2\left(\rho_b - \frac{1}{2}\rho_l\right)} \tag{2.2}$$

[67]

Out of this a second order ODE is formed in the paper in the form of:

$$\ddot{x} + K\dot{x} - KU_f = 0 \tag{2.3}$$

[67]

where $\ddot{x} = a_p$ and $\dot{x} = U_p$ and $K = \frac{18\mu}{4r^2\left(\rho_b - \frac{1}{2}\rho_l\right)}$

The solution for $\dot{x}$, mentioned in the paper, is:

$$U_p = \dot{x} = U_f(1 - e^{-Kt}) \tag{2.4}$$

[67]

Because were interested in the particle velocity and not in the position of the particle at this moment, we work with $\dot{x}$ (=U_p) and not x.

We have to notice that there are some differences in this simplified form, when compared with the Basset equation: some force terms are neglected and there is a difference in the use of acceleration with the added mass in both formulas. The advantage is that this paper describes this situation for the hydrogen bubble method. Because of both points, we look further in more recent literature what is stated about tracer fidelity.

We can assume that tracer particles, following a turbulent flow inside a tube accurately, are also able to follow laminar flow accurately in the same pipe. This assumption is reasonable because the characteristic length and characteristic time scales in turbulent flows are much smaller than in laminar flows in the same system. Hence, if for a turbulent flow the instantaneous velocity $V \to 0$ within this characteristic time, tracer fidelity is also guaranteed for laminar flow.

In literature tracer fidelity for turbulent flows are well defined. [69] We will use the same kind of approach for determining tracer fidelity.

A way to quantify the tracer fidelity is the Stokes Number. This is the ratio between characteristic time response and the characteristic time flow scale.[71] The Stokes Number St can be calculated with:

$$St = \frac{\rho_p U_f d_p^2}{18\mu_f L_c} \tag{2.5}$$

Where d_p: particle diameter; U_f: (upstream) fluid velocity; L_c: characteristic length scale

[72]
Where the subscript p stands for particle and subscript f for fluid.

Besides this, also the particles Reynolds number is important. This is defined as:

$$Re_p = \frac{\rho_f V d_p}{\mu} = \frac{V d_p}{\nu} \tag{2.6}$$

[69]

Besides the Reynolds particle number and Stokes number as important dimensionless numbers, another parameter is important to mention when analysing small particles moving into a fluid. This is the drag force F_d.

The drag (force) is defined in Encyclopaedia Brittannica as: “force exerted by a fluid stream on any obstacle in its path or felt by an object moving through a fluid.”[73]

The drag force can be calculated with:

$$F_{drag} = \frac{1}{2} C_d A \rho_f V^2 \tag{2.7}$$

Where C_d: the drag coefficient; and A: frontal area

[74]

In the case of a sphere this projected area (A), normal to the flow direction, is equal to the area of a circle: $A = \pi r_p^2 = \frac{1}{4}\pi {d_p}^2$.

In the laminar situation where $Re_p < 1$ the drag coefficient for a sphere is:

$$C_d = \frac{24}{Re} \tag{2.8}$$

[74]

We can substitute C_d in the previous equation and get for Stokes flow:

$$F_{drag} = \frac{1}{2} C_d A \rho_f V^2 = \frac{1}{2} \frac{24}{Re} A \rho_f V^2 = \frac{1}{2} \frac{24}{\frac{\rho_f V d_p}{\mu}} \frac{\pi d_p^2}{4} \rho_f V^2 = 3\pi \mu d_p V \quad (2.9)$$

[74]

This expression is called Stokes law. [74] Stokes law shows that a smaller particle gives a lower drag force.

Some background information about the relation between Stokes Law and the Navier-Stokes equation can be found in Chapter 5 of the book "Aerosol Technology: Properties, Behavior, and Measurement of Airborne Particles" of Hinds. [75] Here it is also stated that in Stokes flow the viscous terms dominate the inertial terms in the equation of motion.
Stokes law can be seen in the equation of motion in formula (2.1), directly after the equal sign.

Recently in 2016, a paper is published about the relation between particle size and PIV measurements by Van Overbrüggen et al. For (recent) theoretical background information about this research area, we refer to this article. [76]

In the next paragraph, we will define a situation for which some tracking parameters can be calculated. With this, we want to find the order of magnitude for the particles diameter d_p, which is needed to obtain flow tracking abilities.

B: Calculation with an example regarding to tracer fidelity

We will calculate a situation where we have a steady flow of water through a tube of 26 mm with a flowrate similar of that in the abdominal aorta. Besides this, we give an indication of the parameters involved in tracer fidelity during specific flow conditions. Some of these are summarised in table 3.

Table 3: Some parameters needed for calculating the tracer fidelity in a laminar flow, fluid is water and the particle consists of hydrogen gas.

Particle density	ρ_p	0.09 kg/m³ [77]
Particle diameter	d_p	2.5×10^{-5} m
Fluid kinematic viscosity	ν_f	1.004×10^{-6} m²/s [52]
Fluid dynamic viscosity	μ_f	1.002×10^{-3} kg/m.s [52]
Fluid density	ρ_f	998.2 kg/m³ [52]
Hydrodynamic diameter tube	D	26×10^{-3} m [52]
Fluid velocity	U_f	0.094 m/s

In the case of the abdominal aorta, the flow rate is in the order of 3 L/min [54] (equal to: 5.0×10^{-5} m³/s). The tubes' cross-sectional area is: $\pi\times(13\times10^{-3}\ \mathrm{m})^2 = 5.3\times10^{-4}\ \mathrm{m}^2$.
With both variables, we are able to calculate the fluid velocity U_f in a tube of 26 mm in diameter:

$$U_f = \frac{Q}{A} = \frac{5.0\times10^{-5}\ \mathrm{m}^3/\mathrm{s}}{5.3\times10^{-4}\ \mathrm{m}^2} = 0.094\ \mathrm{m/s}$$

This means, in this example, the average velocity is 9.4 cm/s.

The next step is to calculate the Reynolds particle number. For the type of particles we can for instance look at hydrogen gas bubbles. Let the bubble diameter be 25 µm, which gives a Reynolds particle number of:

$$Re_p = \frac{998.2\ \mathrm{kg/m^3}\times0.094\ \mathrm{m/s}\times2.5*10^{-5}\ \mathrm{m}}{1.002\times10^{-3}\ \mathrm{kg/(m.s)}} = 2.34$$

For further analysing the tracking ability of particles, Stokes' drag law can be used. It applies for the condition $Re_p < 1$, which is called Stokes flow. [69] It gains more insight in tracer fidelity by applying for example the formula for particle relaxation time [75].This will be discussed later on in this chapter. For Stokes flow the fluid velocity or the particle diameter needs to be adjusted.

With this in mind, we can determine a particle diameter based on the Reynolds number of the particle, the Stokes number and a maximal difference in velocity between the fluid and the particle that we can formulate (for example 10% difference).

For our example, using equation (2.5) and table 3, this gives:

$$St = \frac{0.09\ \mathrm{kg/m^3}\times0.094\ \mathrm{m/s}\times(2.5\times10^{-5}\ \mathrm{m})^2}{18\times1.002\times10^{-3}\ \mathrm{kg/(m.s)}\times26\times10^{-3}\ \mathrm{m}} = 1.1\times10^{-8}$$

With regard to the tracking error it is stated in the book "Springer handbook of experimental fluid mechanics" that a Stokes number lower than 0.1 will give a tracking error below 0.1%. [71]

This means, based on this calculated Stokes number alone, the tracking error is already low. However, this example is not representing a Stokes flow. For further analysing the tracer fidelity we adjust Reynolds particles number $Re_p < 1$ to analyse some limits.

In this case we want the tracking error to be below 0.1%. So, we want to satisfy a $Re_p \ll 1$ and St<0.1 we will determine these limits by calculating the particle diameter for $Re_p = 1$ and $U_f = 0.094\ \mathrm{m/s}$ (situation 1) and the maximum U_f that will be followed by tracer particles of 25 µm diameter in the Stokes regime at $Re_p = 1$ (situation 2).

Situation 1:

For calculating the particle diameter, reordening formula (2.6) for Re_p is necessary.

Where we assume that: $U_{f,max} \sim V$

$$d_p = \frac{Re_p\times\mu}{\rho_f V} = \frac{1\times1.002\times10^{-3}\ \mathrm{kg/m.s}}{998.2\ \mathrm{kg/m^3}\times0.094\ \mathrm{m/s}} = 1.068\times10^{-5}\ \mathrm{m}$$

This shows, that for having Stokes flow, the particle diameter has to be lower than 10.7 µm.

Situation 2:

Where we assume that: $U_{f,max} \sim V$

$$V = \frac{Re_p \times \mu}{\rho_f d_p} = \frac{1 \times 1.002 \times 10^{-3}\ \text{kg/m.s}}{998.2\ \text{kg/m}^3 \times 2.5 \times 10^{-5}\ \text{m}} = 0.04\ \text{m/s}$$

With a particle size of 25 µm the maximum fluid velocity that is possible, for calling it Stokes flow, is 0.04 m/s.

Calculating this to volumetric flowrate gives:

$$Q = U_f \times A = 0.04\ \text{m/s} \times 5.3 \times 10^{-4}\ \text{m}^2 = 2.1 \times 10^{-5}\ \text{m}^3/\text{s}$$

Which is equal to 1.27 L/min.

Besides the Stokes number, it is important to know how much time it take for particles to follow the fluid velocity. This will be discussed in the next paragraph.

C: Relaxation time

The difference between particle velocity and fluid velocity reduces as the particle propagates. This is quantified in relaxation time, where the instantaneous relative velocity V is decreased with a factor 1/e.[69]

The relaxation time τ can be calculated for the Stokes regime for $Re_p < 1$ with:

$$\tau = \frac{\rho_p d_p^2 C_c}{18 \mu_f} \tag{2.10}$$

[75]

With the main condition that this holds only in the Stokes regime. Here is C_c the slip correction factor, which can be neglected for particles greater than 10 µm in diameter. [75]

One important notice is that in the book of springer Particle Image Velocimetry: practical guide of Markus Raffel et al. it is mentioned that the formula for the relaxation time works for the condition that the tracer particle density is higher than that of the fluid.[78] In our example it is the opposite situation, the particle density (of a gas) as smaller than that of the surrounding liquid. We think that the added mass for a particle, which is much heavier more than the fluid ($\rho_p \gg \rho_f$)is neglectable. If this is not the case, we expect a relatively longer relaxation time.

In our case, using equation (2.10), this means:

$$\boldsymbol{\tau} = \frac{0.09\ \text{kg/m}^3 \times (2.5 \times 10^{-5}\ \text{m})^2}{18 \times 1.002 \times 10^{-3}\ \text{kg/m.s}} = 3.1 \times 10^{-9}\text{s}$$

In the case of Stokes flow the particle relaxation time is 3.1 ns for particles of 25 µm.

From the calculations above we can make some preliminary conclusions that give an indication of the tracer fidelity.

If the flow is laminar and Stokes flow conditions applies, then it is accurate, the error is below the 0.1%.
For turbulence flows it can be accurate till certain frequencies/relaxation times of turbulent eddies (see for more information the paper of Melling [69] and the paper of Mei [79]).

Parameters, like relaxation time and Stokes number, are important for tracer fidelity. The reason for this is that particles need some time to adopt to the flow. Examples are oscillating flows. The time between two oscillations should be longer than the time needed to follow the flow. Otherwise the flow visualisation is not possible in unsteady flows. However, in the case the flow parameters in the obstacle or the obstacle itself changes (curves, bifurcations) the tracer fidelity may be calculated analytically or by Computational Fluid Dynamics (CFD).

The conclusion based on these first calculations is that a particle diameter in the order of micrometres is required to get tracer fidelity.

2.3.2 Scattering

Not only the tracer fidelity of the tracer particles based on its size and density is important, but also on the light scattering properties. These are important for capturing the particles on images and the possibility to analyse them. These properties will be discussed here.

The light scattering properties are mainly important when we use optical techniques for detecting the flow properties.

There are different ways light can interact with particles in our case we look at spherical tracer particles. In that situation Mie scattering occur [80], which, in addition, also depends on the diameter of the particle and the wavelength of the light. [81]

In figure 11, taken from [81], we see different types of scattering based on the wavelength of the incoming light and the particle radius by which the light is scattered.
This relation can be summarised in the size parameter x and can be calculated with:

$$x = \frac{\pi d_p}{\lambda} \tag{2.11}$$

[82]

For example in the case where the particle diameter is equal to 25 µm and we take the wavelength of light in the visible range: from 380 nm to 780 [83] the size parameter $x < 2000$. This is in the so-called Mie regime.

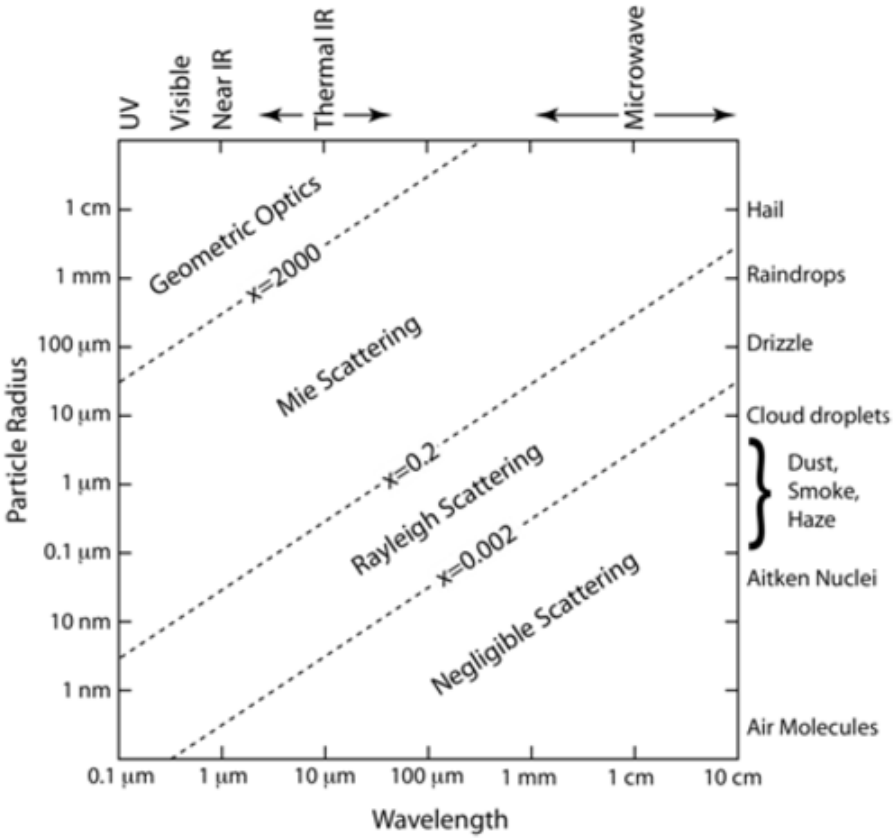

Figure 11: Taken from [81]In this figure different ways of scattering are illustrated by the relation between particle radius and the wavelength.

In figure 11, we see that Mie scattering occurs in this case. Mie scattering dominates more in the forward than in the backward direction [84].

Springer Handbook of experimental fluid dynamics illustrates that scattering amplitudes can be small in certain angles, which requires a strong light sources for PIV [71].
We can verify this by making a polar plot in the case of Mie scattering. Mieplot v4.6.03.[85] was used for the simulation. This was done for the case of an air particle with a radius of 12.5 µm in water (with the refractive index of water based on IAPWS[1]). All different plots can be seen in Appendix I. We took two different wavelengths (440 nm and 575 nm), corresponding to the two peaks with the highest relative power distribution of a high-power LED (see Appendix I).

For this simulation, we are mainly interested in the scattering anisotropy g.

The scattering anisotropy g can be calculated with:

$$g = \int_{4\pi} P(cos\theta) cos\theta d\theta = < cos\theta > \tag{2.12}$$

$g = 0$ Isotropic scattering

$g \to 1$Forward scattering

[1] International Association for the Properties of Water and Steam.

$g \to -1$ Backward scattering

[80]

From the simulation with Mieplot [85] we obtain an anisotropy value $g = 0.84$ at 440 nm and $g = 0.85$ at 575 nm, meaning there is mainly forward scattering. Comparing both polar graphs shows that mainly forward scattering occurs.

With this in mind, we should consider a high-power LED to get enough contrast between the different particles and the fluid.

2.3.3 "Hardware" for experimental setup

In this previous part we focused on the optical and tracking characteristics of the tracer particles. From here we focus on the experimental set-up. Which experimental set-up requirements have to be made for an initial flow visualisation experiment?

-Straight tube, without curves and branches:

A first step to look for a flow visualisation technique, is to investigate the flow in a straight tube. One of the reasons is the parabolic flow profile (in the case of a laminar flow), that is easy recognised. The implementation of branches and curves makes the quantification of tracer fidelity more complex. For example, if we look at the difference in inertia between the fluid particles and tracer particles. This requires additional modelling/calculations.

-Enough fluid is required for a fully filled tube system:

This is needed to avoid a sudden pressure drop in the tube, while pumping the fluid around. This can effect in a pulse pressure/wave into the fluid stream.

-At the inlet of the main tube air(bubbles) should not be present:

In addition to the previous aspect: Air bubbles, which end up at the inlet of the main tube, could cause a pulse wave in that tube. This disturbs the laminar flow profile and in this way also the flow visualisation.

-For an ideal situation for analysing and verifying tracer fidelity Stokes flow is considered:

But because in reality blood flows in the main arteries are at higher velocities Stokes' flow is not considered as the most desirable situation for laminar (/"biological") blood flow simulation. This means that in reality the Reynolds number based on the particle may be higher than 1.

-Steady flow:

In the case of a steady flow, flow visualisation is much easier to predict and analyse.
The tracer particles can have much more (response) time to be accelerated till the fluid velocity is reached and the flow profile is easier to capture. At the position/moment that the flow profile is recorded, V has to be minimal.

-Able to see a laminar flow profile:

If tracer fidelity is established a laminar flow profile should be seen. And the optical properties are not forming a limitation for capturing images with a flow profile.
Besides this, we see that theory and practise are congruent, and we have material to compare if we see “laminar” flow profiles with X-ray PIV. Assuming the tracer particles are the same in diameter and density, etc.

-Tube: constant diameter, long enough for entrance length

For getting a laminar profile, the flow profile has to develop. This means we want a tube with a constant diameter. Besides this, the tube should be longer than the entrance length to get a laminar profile.

-Easy to produce

-Pump: required for transporting the fluid through the “tube system”.

-Tube system reservoir: function as buffer for filling the tube system with enough water.

2.3.4 Type of tracer particles

As already mentioned bubbles can be identified by X-ray imaging and this is not difficult to implement. Therefore, these are some of the reasons why we choose to define our requirements based on the earlier mentioned hydrogen bubble method.

The way seeding particles, in this case hydrogen bubbles, travel through a fluid can be described in different ways. There are three terms to hold into account when looking at this technique. First of all, the collection of points all particles have travelled entering a specific point in space is called the streakline. Secondly, the path which along a particle travels in the fluid is called a pathline. In steady flows, both are the same. And finally, the line at every position tangent to the velocity vector is called the streamline. [62]

-Using timelines as simplification:

The velocity of the tracer particle can be easily calculated by the time between two pulses divided by the space between the bubble rows.[67] The lines produces by the electrode are called the timelines [62].
Another way of defining timelines is a specific line of fluid particles at a specific moment that was a continuous line at a time level in the near past[86].

-Type of probe:

For the electrode different materials can be used: stainless steel or platinum [62]. In the paper of Fox and Davis also tungsten is mentioned. [67]

Platinum is more expensive than stainless steel and stainless steel is stronger. Platinum can be used longer for electrolysis of water.[62] Mainly because platinum is currently quite expensive to buy, we will choose for a thin stainless steel wire.

-Thickness of the wire:

Most wires used for this technique are very thin. The bubbles formed at this wire are approximately ½ of the wire diameter up to the wire diameter itself. [62] Because of the tracer fidelity and wire strength we will use a maximum wire diameter of 100 μm.

-Polarity change:

Polarity should be changed for a short period of time, as bubble formation becomes unstable. [62] This means the electric circuit should be able to change polarity when it is required.

-Lighting:

In order to increase the contrast between the area of the flowing fluid and the hydrogen bubbles high intensity lighting should be used. And if necessary the room should be darkened.

-Pulsating voltage:

The timelines should be “thin” enough to estimate the time difference between two rows of bubbles. Otherwise, for calculating the velocity subtracting of two time levels is not discrete enough.

-Adding salt:

For the electrolysis of water, some salt should be added to initiate the electrolysis at a safe voltage level.

-Using relative low DC voltage levels:

Due to safety, we should not exceed high voltage levels during the experiments. Therefore, an absolute maximum voltage of 40 V is defined. This can be partly implemented in the extra circuit for changing polarity.

Redefinition of the first goal

With these requirements, we can make our goal more explicit:

Create a model for visualisation of timelines in a clear tube and that if possible can be used for comparing with an X-ray PIV method.

2.4 Experimental set-up: concepts and subconcepts

In this paragraph, the experimental set-up will be discussed. This experimental set-up for the generation of hydrogen bubbles consisted of several elements.

An electric circuit (see Appendix I) was build based on a H-bridge to change polarity when necessary and was used to sent pulsed voltages to the stainless steel 316 wire of 50 µm/100 µm in diameter. The original pulse sent by the pulse generator (Agilent 33120A). This was done in order to get timelines. The pulse generator was set on burst mode to get very low duty cycles (<20 percent). Otherwise, we cannot speak about time “lines” but more about time “rectangles”.
The voltage levels were checked with an oscilloscope.

In the original situation an aorta phantom was added, see figure 12 and figure 13. Unfortunately, this did not work out for this experiment (see discussion).

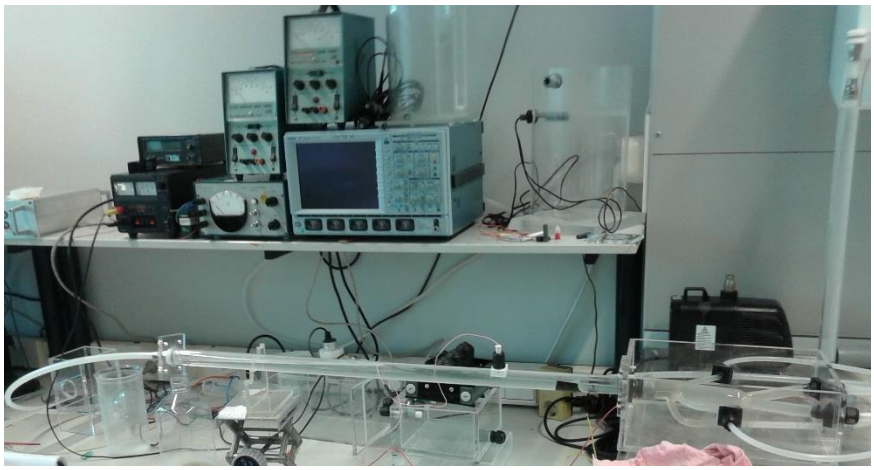

Figure 12: Experimental set-up with the aorta phantom.

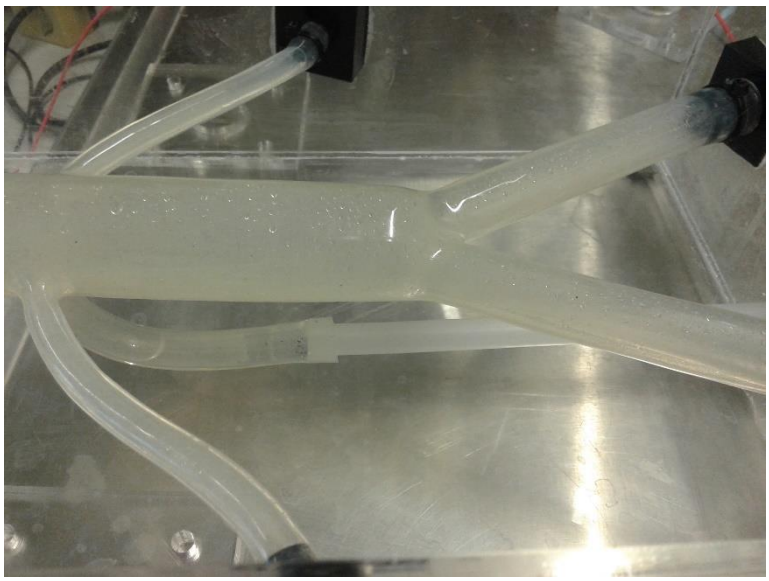

Figure 13: Close up of the aorta phantom with its main bifurcations

For testing the technique, the electrolysis was tested in a small tube (see figure 14).

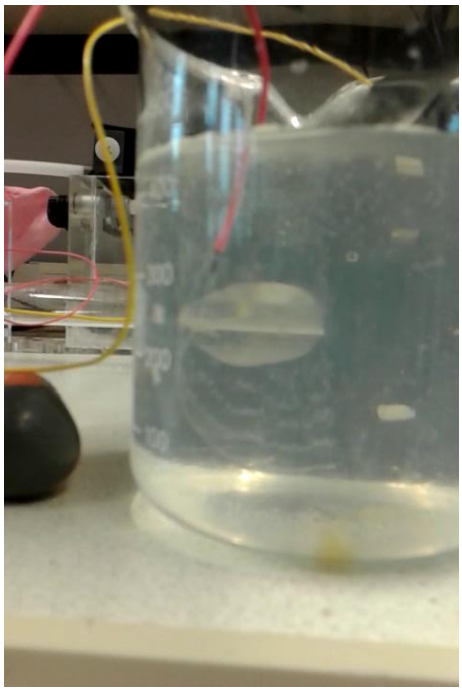

Figure 14: Snapshot of video checking the pulsating production of hydrogen bubbles.

In figure 15, a part of the devices is shown forming the pulsating voltage, needed for generating hydrogen bubbles (seen in figure 14): the oscilloscope for analysing the pulse, the pulse generator and the power supply for the pump

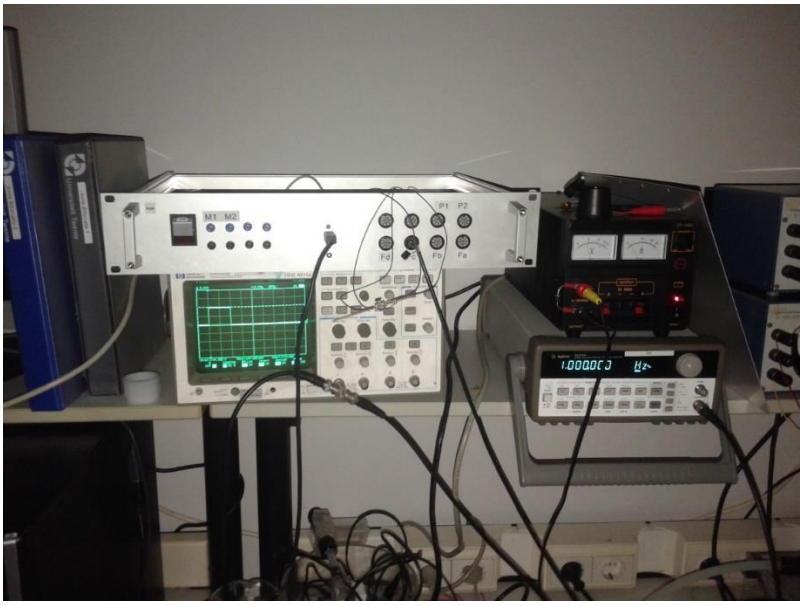

Figure 15: Part of the devices used for the experiments: power supply, pulse generator on this picture showing 1 Hz and the oscilloscope for checking the pulse

In figure 16, the camera (Sony XCD-X710 v.300 E) with a high-power LED (: Opulent REBEl-STAR-ES-NW200 High Brightness LED, see Appendix I) is shown. It is also shown that some bubbles adhere on the wall of the tube.

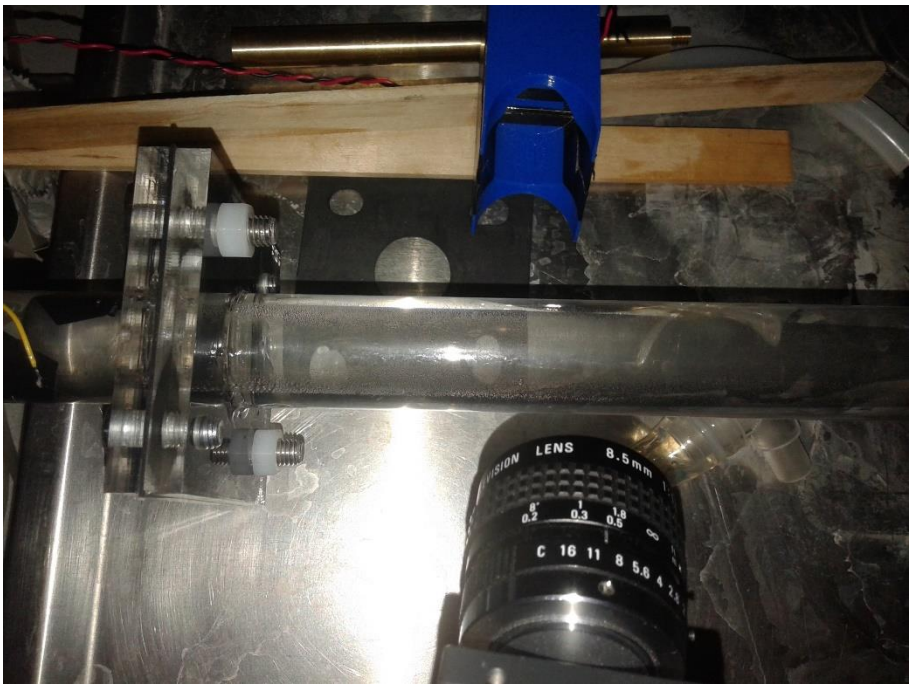

Figure 16: Camera with illumination (high power LED) for filming the timelines

In order to get a clear overview of the experimental set-up, we refer to figure 17 for the scheme showing the different parts of the model.

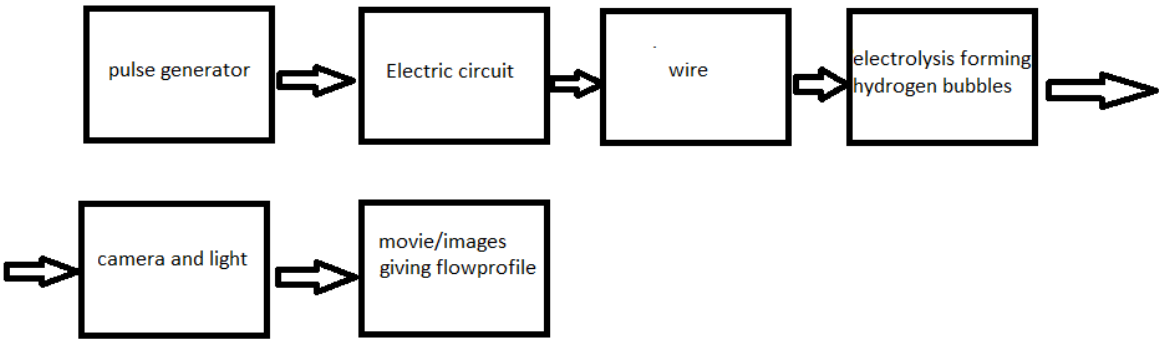

Figure 17: Schematic overview of the experimental model used for the hydrogen bubble technique

2.5 Results/evaluation

In the figures 18 to 25, timelines can be seen using different frequencies (1 Hz and 2 Hz with 20 percent duty cycle) with the effect of some filtering (background subtraction and contrast enhancement). In some cases, the onset of a parabolic profile can be recognised.

At 1 Hz, the background looks the same as in the case of 0.5 Hz. And there are no frames in the recorded movie (in the 1 Hz situation) without timelines, due to the higher frequency and the relative small region, that was filmed. Therefore, the background image was chosen in the situation where the frequency was 0.5 Hz (see figure 18).

This background image is followed by three figures (19, 20, and 21) showing the situation at 1 Hz and three figures (22, 23 and 24) showing the situation at 2 Hz. Finally, a snapshot from another camera is shown.

In figures 22, 23 and 24, consecutively, the original image, the image with background subtraction (of figure 18) and the combination of background subtraction and contrast enhancement is shown.

In figures 22 (original image) and 23 (with background subtraction) and 24 (background subtraction and contrast enhancement), a part of the timeline is visible at a frequency of 2 Hz and a duty cycle of 20 percent.

Figure 25 shows a snapshot of the movie taken with another camera, showing a parabolic profile.

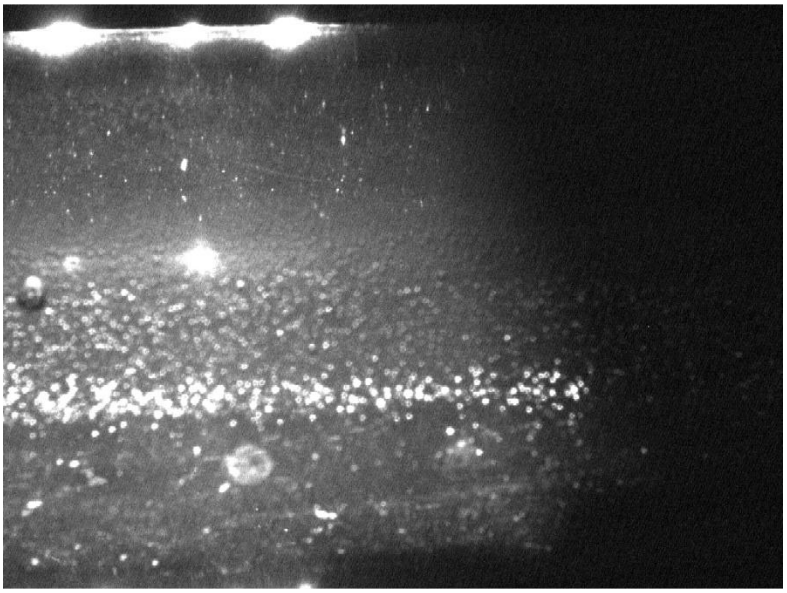

Figure 18: Background image at pulsation of 0.5 Hz and a duty cycle of 20 percent, frame 837. In this image are no timelines seen, therefore this is used as background image.

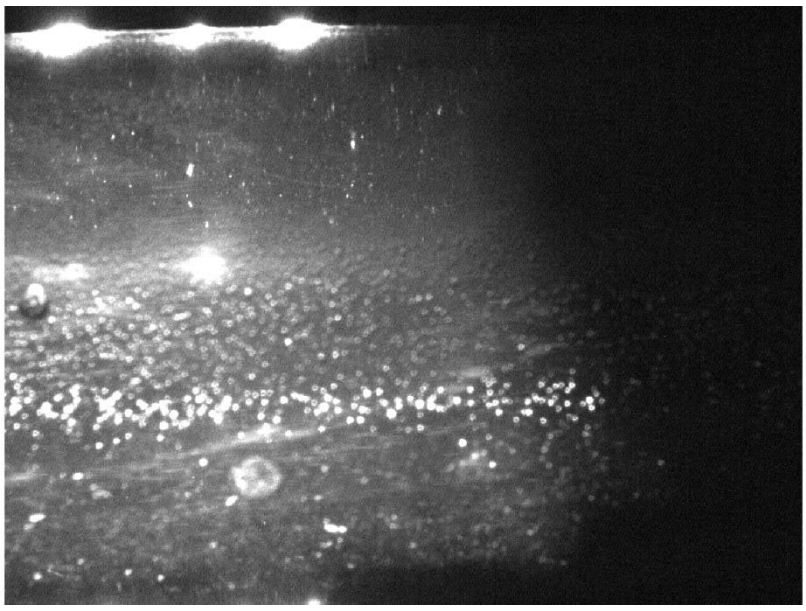

Figure 19: Original frame with a pulse of 1 Hz and a duty cycle of 20 percent

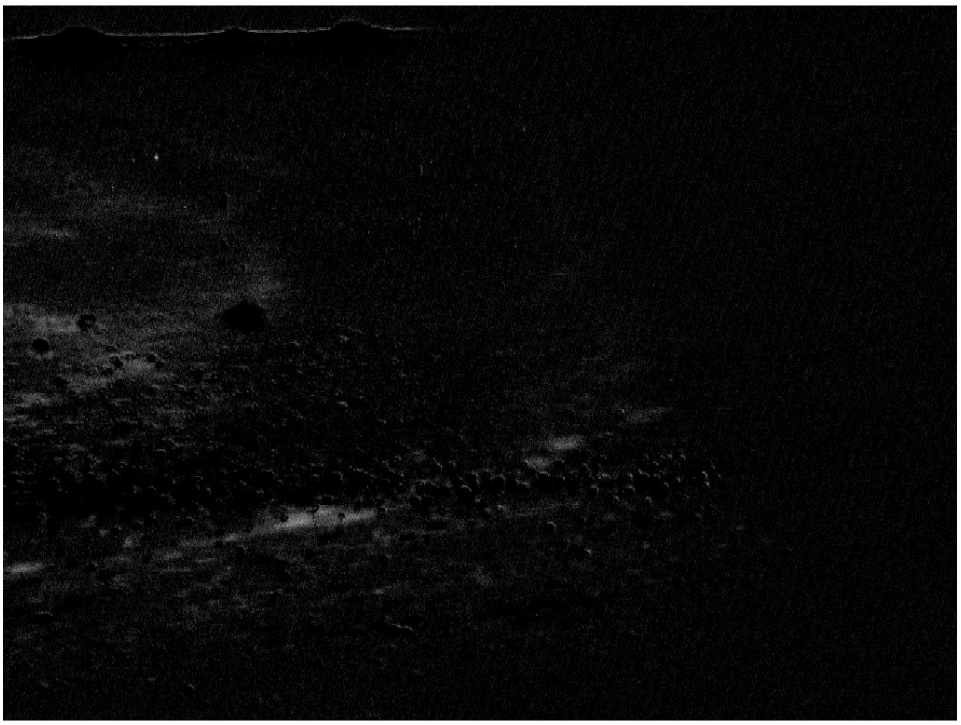

Figure 20: Background subtraction of the figure above.

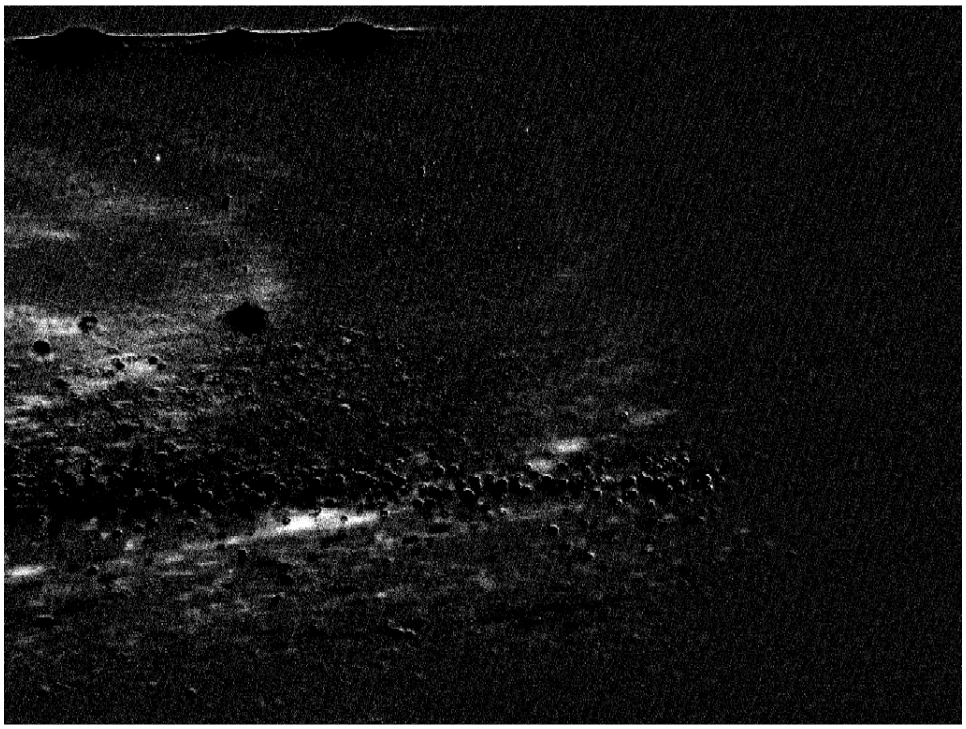

Figure 21: Background subtraction in combination with contrast enhancement

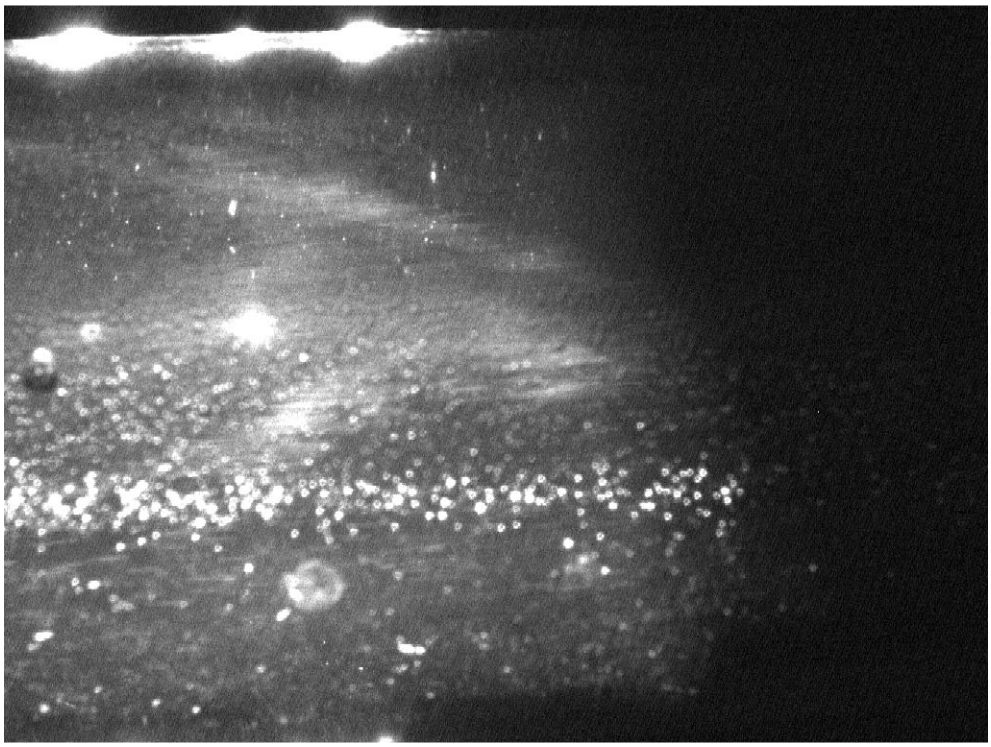

Figure 22: Almost no visible timeline due to the strong illumination (scattering)

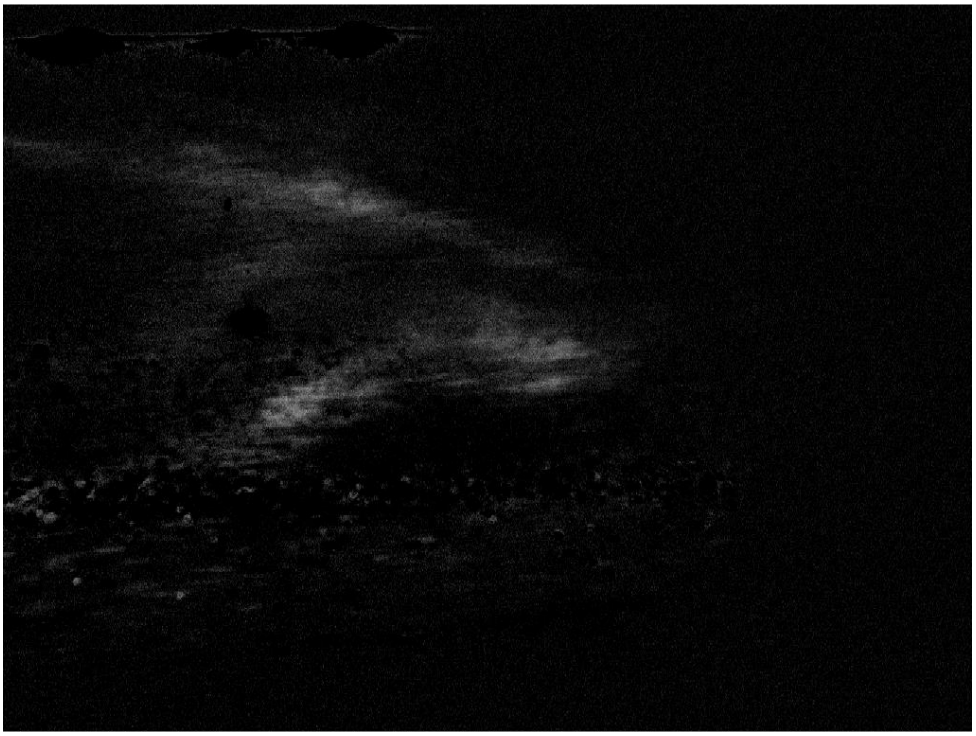

Figure 23: Filtered with background subtraction: small "top" of the timeline at the left and a profile from the wall more to the right, looks as a parabolic shape.

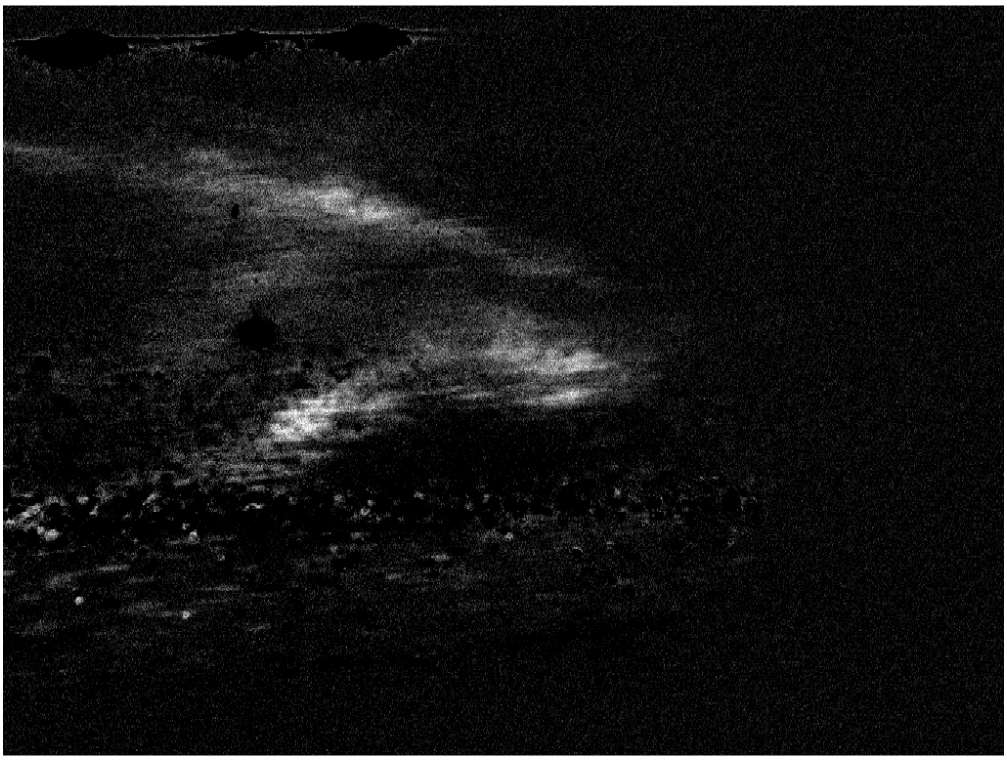

Figure 24: Filtered image with background subtraction and contrast enhancement.

Figure 25: Snapshot of video showing a parabolic shape.

2.6 Discussion

In 1994, the hydrogen bubble visualisation was used by Palmen et al. for simulating flow in an in-vitro model of a carotid artery with stenosis. In that case, the researchers were able to study the flow in different grades of stenosis. [59] Our research is looking at bubbles as flow visualisation tool for an X-ray PIV/PTV based technique studying flows inside stent grafts, with optical PIV as first step.

The initial idea was to use the hydrogen bubble method in an in-vitro model of the aorta abdominalis. However, during the preparations, small “ruptures” developed in the silicon material. Also, the particles were not visible anymore, because deposits of salts and other substances remained at the wall of the tube. These things forced us to continue our research with a straight model, which is mentioned in the paragraph 2.3.3 and paragraph 2.4.

The deposits of salt and “other dirt” at the wall were a serious problem in respect to visibility of the flow profile, which is essential in flow visualisation. This can be seen in figure 18 and the other results.

For the straight model as we can see (in figure 18, figure 19 and figure 22) some small bubbles adhere at the wall of the tube. This made the time period using bubbles for flow visualisation small. A way to avoid this might be a hydrophilic coating at the wall, meaning the water molecules will move more smoothly along the wall, instead of bubbles that will adhere to it. A disadvantage is that the wall structure changes (Fluid-Solid interaction at the wall might change) which can make a difference in the obtained velocity profile compared to the situation without a coating. Also, for this reason, if used, the coating has to be placed homogenous along the whole wall of the tube. This can cause problems (regarding to the transparency of the material).

Because of the adhesion of “dirt” in some cases, image processing might be necessary, such as background subtraction (see the difference between figure 22 and figure 23). However, analysing the different videos, we see that if there is too much dirt/noise, it is not useful anymore to apply background subtraction. This is mainly because too much useful data within the region of interest of the tube is filtered out. Therefore, it was difficult to take snapshots where a parabolic profile could be seen.

The videos make things more clear. A clear snapshot, showing a quite good parabolic shape, is the final picture in the results (figure 25). Showing a parabolic/laminar profile was the main goal of this part. With this result, we can move on to the next step of the research: using X-ray imaging.

Another aspect that we looked at was the problem of bubbles that may displace due to buoyance, during the recording of the timelines. Schraub et al. discussed this by mentioning that the trajectories of bubbles within timelines cannot be seen. The idea of solving this is by using time-streaklines. It was proposed to use a wire with coated insulated regions at regular sections. [62]

We did not use this proposed method, because of the thickness of the wire in combination with the spray that was available. It would be difficult to spray this wire with a homogenous layer at the whole circumference at the different sections, that need to be insulated.

We thought to solve this, with a different method, by developing a probe like in the figure below:

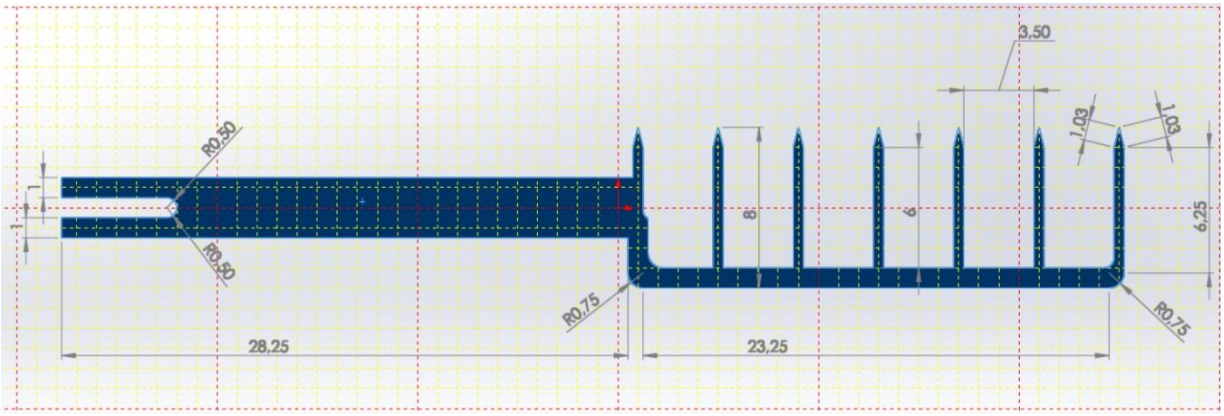

Figure 26: Concept for using time-streaklines, was not implemented further during the research.

This probe was experimented with shortly. Because this probe might induce vortices and the alignment is crucial, we did not use it for the recordings of the flow profile. Besides this, the lines in horizontal direction are very thin and only a few data points in vertical direction are available. Looking back at the results of a normal wire (without insulated regions), where not the whole timeline is seen on camera, this probe (figure 26) is not useful enough for doing velocity calculations.

Therefore, we continued with using normal wires for the bubble experiments: first a thicker wire (100 µm in diameter). This wire was, however, not good enough for tracer fidelity (the bubbles should be smaller, see the calculations in the paragraph "Requirements" of this chapter). Later on, a stainless steel wire of 50 µm in diameter was used. We chose to use this as minimum diameter, because by taking thinner wires: the strength decreases and the risk of rupture increases. This would have made it more difficult to analyse timelines.
Although, the wire broke a couple of times. This also shows a strong material is required for a proper way of using this technique. The way the wire is glued in the tube is important as well.

Looking at timelines means two main aspects for analysing fluid flows:

1) more than one timeline should be visible on a frame, required for analysing the distance between the timelines
2) the timeline should be a line and not a square: the pulse should be short enough.

Based on the experiments done, it is useful to analyse the fluid flow based on initial settings on the pulse generator (a certain frequency and pulse width, using the pulse generator indirectly defined as duty cycle) and use a sort of feedback loop which alters these two parameters until the points mentioned above are satisfied. In this way, the settings are optimised for the fluid flow, which is being analysed.

Looking at the goals of this report, we want at the end of this chapter to make the transition from optical to x-ray based techniques for flow visualisation. For this purpose different tracer particles, for example bubbles with a special coating, might be desirable. This should result in better recognition of these particles on X-ray images. These particles might have a higher density than the surrounding fluid ($\rho_p > \rho_f$). In that case we can use some formulas, mentioned in the book of Hinds et al. [75], to approximate the diameter of a particle needed for tracer fidelity and couple this to the position of the camera (defined as the distance from where the particles are created/injected).

The velocity of a particle in fluid as function of time is

$$U_p(t) = U_f + \left(U_{p0} - U_f\right)e^{-t/\tau} \tag{2.13}$$

Where U_{p0}: the initial velocity of the particle at $t = 0$; and $\left(\frac{ds_p}{dt}\right)_{t=0} = U_{p0}$; and τ: defined in formula (2.10).

The next step is to define the difference between the fluid velocity and particles velocity as ratio of the fluid velocity, this holds:

$$\frac{|U_f - U_p|}{U_f} \ll 1 \tag{2.14}$$

We want that this ratio in a sufficient period of time goes to 0.1. In other words, the difference between the particle velocity and fluid velocity approaches 10%.

Substitute equation (2.14) in equation (2.15):

$$\frac{-(U_{p0} - U_f)e^{-t/\tau}}{U_f} = 0.1 \tag{2.15}$$

When equation (2.15) is rewritten in terms of d_p it follows that $d_p = d_p(U_f, t, \rho_p, \mu, U_{p0})$. With this equation, it is possible to calculate the particle diameter which is needed to satisfy the condition in equation (2.15), within a predefined period of time.

This period of time can be expressed as a distance being traveled by the particle. Therefore, a maximum traveling distance can be defined at which the difference between the particle velocity and fluid velocity approaches, say, 10%.

The position of a particle in fluid is, found in the book of Hinds et al.:

$$s_p(t) = U_f t + \tau(U_{p0} - U_f)(1 - e^{t/\tau}) \tag{2.16}$$

[75]

From this equation, we can write the particle diameter in a second equation

$d_p = d_p(U_f, t, \rho_p, \mu, U_{p0})$. By equating the two expressions of d_p, we can solve for the unknown parameter t and subsequently can calculate the corresponding d_p. This is a method which can be used for the requirement of the tracer particles in a PIV system.

Besides the studying influence of catheters (see the introduction of this chapter), other research goals may also be considered using the hydrogen bubble technique. We can think of looking at the influence of using catheters for infusion of fluid which can be temporally in the vessels (like blood transfusion), but also for longer period, like different types of dialysis/hemofiltration. Or we gain more insight in the physiological influence of a bypass operation, because of the interventions made inside vessel. We can think, for instance, at the analysis of a Coronary Artery Bypass Grafting (CABG) vs. placing stent grafts.

When we are able to visualise the timeline better (in other words: unbroken timelines) than those shown in the figures of this chapter, we might use an algorithm to determine the velocity of the fluid in a tube, and subsequently make the flow pulsatile. On this moment, visualisation of the timelines for pulsating flows is difficult.

This algorithm should look at difference in space and time. For the difference in space, it could look at the spatial difference between the pixels of both timelines, if the tube alignment is in the same direction. For the difference in time, the duty cycle and frequency can be used.

We will shortly mention the image processing used for the hydrogen bubble visualisation of two papers: from Lu et al. [87] and Pauley et al. [88]. In these papers, such algorithms are discussed.

One of the papers that discusses the hydrogen bubble experiment and the image processing is the paper of Lu and Smith from 1985. In this paper mainly low pass filters were used to smooth the image because of the noise irregularities and some kind of edge detection was used. [87]

In the paper of Pauley et al., some techniques for image processing of timelines are discussed [88]:

- Vertical line enhancement can be used for lines with a width of 1 pixel. This is not the case in timelines.
- Optimal thresholding based on a histogram, which is done by statistical analysis. A disadvantage is that because of the non-uniform lighting there can be difference in intensity of the noise at different areas within the region of interest.
- Gradient/Laplacian method: looking at the gradient of a row of pixels, detecting the edge of a line of bubbles on a dark background.

  [88]

This last technique uses a convolution mask, meaning each pixel around the centre pixel is multiplied by a certain weighting coefficient, which alters the pixel value in the middle of the mask. Different options are possible: averaging based on the neighbours, Sobel operator (3×3 mask: $\left\langle \begin{matrix} 1 & 0 & -1 \\ 2 & 0 & -2 \\ 1 & 0 & -1 \end{matrix} \right\rangle$) smooths the neighbouring pixels. This means the effect of noise is decreased. Low pass filters are preferred in smoothing above median filters. The reason is median filters may affect the shape of the intensity distribution (at the edges) in contrast to low pass filters. The second derivative can be taken to find the edges. These are the locations where the intensity changes/gradient is maximum and the second derivative is zero. Noise can be filtered out by comparing the size of gradients of noise and timelines. This can be followed by threshold filtering, to filter out the noise by setting a threshold. The mean of the derivative was calculated as threshold and each pixels lower than that threshold was made zero, all values above the threshold remain the same. This can be finished by taking the mask $\left\langle \begin{matrix} 0 & 0 & 0 \\ 1 & 0 & 1 \\ 0 & 0 & 0 \end{matrix} \right\rangle$ to amplify the different maxima. After the edges are determined, the distance between timelines can be obtained “by measuring” the number of pixels in combination with a scaling factor.[88]

Also, the wake effects of the wire are mentioned as small error source. In the near area there is a difference between the bubble velocity and the true fluid velocity. [88]. However, the relaxation time is very short (see the paragraph about tracer fidelity). Therefore, we can neglect this for now (in the case of a laminar flow).

Besides all, we know also that we look at the flow in a tube. If we do PIV measurements in a tube, where the camera and the light source are not looking at a flat structure, we need to correct for this. Otherwise, the measurements of the displacement can give false results. This can be corrected by

first filming a grid and overlay it with other frames, showing the propagating tracer particles. Another option is to mark the tube with reference points on a regular interval.

Finally, if this al works out, the next step is to investigate also phantom models. In the situation we want to avoid small ruptures, instead of silicon model a rigid glass model can be considered. A disadvantage is the elastic properties cannot be simulated anymore.

2.7 Conclusion

Using the hydrogen bubble technique, we were able to see the onset of a parabolic profile in a straight tube. On video this was easier analysed than based on snapshots. The next step is to look for a way to translate these findings in an X-ray based technique (based on absorption), instead of the conventional optical techniques used for PIV.

3 X-ray PTV technique for developing X-ray PIV

In this chapter, we describe the development of a method for functional analysing flow inside opaque structures. This chapters starts with a short introduction and problem setting of the ongoing research, followed by the requirements for our used technique, experimental setup, results, and finally the discussion and conclusion.

3.1 Introduction

With the previously described optical PIV technique, we can only look at transparent structures. In contrast with optical techniques, flow visualisation in opaque structures (for example: biological tissue and organs) is not possible. With only optical techniques flow patterns will not be shown, because the transparency of the structure becomes the main limitation for imaging tracer particles.

In order to overcome this problem, other imaging modalities (like MRI, ultrasound or X-ray imaging) may play an important role. One of these is the X-ray PIV. This is an X-ray based technique, for studying flows with tracer particles.

For X-ray based techniques two main types may be distinguished: synchrotron phase contrast imaging (PCI) and conventional X-ray imaging based on absorption.

Synchrotron phase contrast imaging can be produced with synchrotrons. In these synchrotrons charged particles get accelerated and remain in a storage ring for several hours. With bending magnets, these particles travel in a quasi-circular orbit. This results in the so-called synchrotron radiation. The spectrum of the radiation, which depends on the magnetic field and the beam energy, is continuous and broad (from infrared to x-rays). With monochromators, it is possible to select a small part of this wavelength band, for example at the X-ray region. The broad and continuous spectrum makes it usable for different fields in scientific research.[89]

Synchrotron radiation is used for example in the field of the fluid dynamics.[90]

In the literature often synchrotron radiation is mentioned for the X-ray PIV technique [91] [92] [93]. The main reason for using PCI in medical research is the contrast on micron based scale [94], [95].

Looking back at the title of this chapter, besides PIV, also the term PTV is mentioned, standing for Particle Tracking Velocimetry.

The difference between PIV and PTV depends on the density of the particle images. In the case the density is low, tracking of the particles is required for velocimetry. In the case of PIV the image density is higher, inspection of pairs of tracer particles in not possible anymore. [78]

In summary, PIV is looking via an Eulerian point of view vs. PTV which looks at a Lagrangian point of view [96].
An example where an X-ray PTV technique for microbubbles, based on synchrotron radiation, is mentioned, is in the paper of Lee and Kim (2005) [97].

3.2 Problemsetting and goals

For producing synchrotron radiation special facilities are required, which are expensive to use. Besides this, it is favourable to look for an easier implementable technique to study flows for medical applications. In this study, we are not able to use a synchrotron facility. This study will focus on the X-ray imaging systems that are used in hospitals, based on absorption. The X-ray systems in the Experimental Centre of Technical Medicine were used for these experiments. These are the Siemens Mobilett XP digital and the OEC 9800 C-arm.

Because flow visualisation in opaque structures is still difficult to achieve, this study will analyse the possibilities for a certain type of tracer particle using (conventional /clinical) X-ray machines.

The ultimate goal will, however, be to develop a method that can be used to visualise a type of flow in opaque structures. In medicine, we can think of flow visualisation inside stent grafts under certain conditions, in rest vs. exercise for example or even in animals.

3.2.1 Subgoals

Before we can reach this goal, we have to define some subgoals. We should be able to:

1) visualise the position of small particles on a single shot X-ray image.

2) visualise motion/movement on X-ray image(s).

3) study the developed method in vitro and try imaging on a sequential way, by creating short image frames after each other.

First of all, the focus of this assignment will be on the first two subgoals. Therefore, in the next paragraph some of the first main requirements of the technique will be discussed briefly.

3.3 Requirements of the different subgoals

In this paragraph, the requirements for each subgoal are defined. These are also subdivided based on the building blocks of this experimental setup.

Subgoal 1: Able to visualise the position of small particles on a single shot X-ray image.

The development of a flow visualisation technique consists of two core elements: the tracer particles and an imaging system to capture them. The requirements of both elements for the X-ray PIV/PTV will be discussed in this paragraph.

A requirements for the Imaging system to capture (tracer) particles

-Clinical X-ray device with a detector inside the Experimental Centre for Technical Medicine (ECTM)
We want a method that can be implemented in the clinic. This requires the use of clinical X-ray imaging systems, which must be available in the ECTM. Because this is the place where experiments with the X-ray systems will take place.

-Capability to make a short pulse image
The requirement for a short pulse exposure is important, because otherwise the attenuation on the beampath (/the path that photons “travel”) will be averaged out over a longer period of time. Because the particle moves in time and only a part of this time the particle(s) will attenuate the X-rays at a specific place. This will result in less contrast in regard to short exposure time (assuming that the particles will cross along the X-ray path) and secondly, it causes motion blurring if the exposure time is too long.

-The type of (tracer) particles should be visible

Because we are developing a way to visualise flow, the visibility of the particles is the far most important requirement of all.

B Requirements for the production of small (tracer)particles

-Size of the particle should be “easy” adjustable
&
-The particles are visible on an X-ray image (: imaging settings):
These two requirements are linked to the requirements stated at part A.
For the optical flow visualisation we have used hydrogen bubbles, which were produced by electrolysis of water. For this electrolysis, a very thin stainless steel wire of 50 µm in diameter was used. And as already mentioned, the diameter of the bubbles is approximately ½ of the wire diameter up to the wire diameter itself [62].
It is not easy to use conventional medical X-ray imaging in this order of magnitude, because the spatial resolution is normally in the order of 1 mm.
Therefore, a different approach should be considered, which results in a primary focus on visualising the small particles. Without the visibility of the particles on an X-ray image, particle tracking on images using X-rays (in opaque structures) will not be possible. This is directly affected by the size of the particles and the spatial resolution of the system. When the particles are not visible, we want to be able to change the particle size in such a way that the particles become visible on an X-ray image.

-Way to produce the particles on an easy way.
There should be an easy way to produce the particle(s) (for example air bubbles), because the timing of the particle injection into the fluid may not become a limitation in respect to the timing of the exposure.

-Adjustable speed to decrease the number of particles per time
The speed of bubbles injected into the fluid must be adjustable, because of two reasons:

1) bubble size: this is a limitation because of the lifting velocity,
2) exposure time: this has to be short enough to avoid motion blurring.

-Way to get rid of pressure overload.
This in combination with the previous points are important to regulate the speed and the size of the bubbles. A pressure overload will give a high particle velocity and “big” particles. This can be a disadvantage for PIV measurements, because small particles are required for tracer fidelity (see the requirements in chapter 2). The goal is to use smaller particles instead of bigger particles.

Subgoal 2: Able to visualise some kind of motion/movement on X-ray image(s).

For the subgoal, image a motion, some additional requirements have to be set up.

First of all, the Mobilett (one of the two X-ray imaging systems at the ECTM) is not able to produce multiple X-ray images in a short sequence. This requires an additional device/feature that makes this possible. This additional feature can be a shutter, for which we also can define requirements. These are listed below.

The shutter should be able:

- to block (when it is closed) X-rays from certain energy levels used in the experiment.

Only the energy spectrum used for the imaging has a functionality in this flow visualisation technique. Therefore, we focus only on the energy spectrum used for capturing the particle motion.

-to open and close fast enough (with a maximum duration of 100 ms).
The shutter should be able to switch between the open and close state in a very short period of time, for letting X-ray through for tens of milliseconds.

-to have a constant operation time (opening plus closing) with a dynamic range of maximal 10 percent between the different operation times.

Besides the shutter requirements, the imaging system and the bubble injection system have to be modified slightly.

For the imaging system this holds:
- when the shutter is placed directly in front of the X-ray tube, the X-ray beam should be rectangular collimated in regard to the size of lead plate (: part of the shutter). This prevents ineffective blocking of the shutter at maximum stroke (the maximum movement of the shutter plate upwards). In the case the beam area is bigger than the area of lead plate, X-rays will not be blocked totally.

Also, the requirement for tuning the number of bubbles per time unit is important, in order to track the motion of individual tracer particles. When a shutter opens, closes and opens again, the bubble should remain within the area that is exposed. Otherwise, the motion cannot be visualised accurately. Another aspect is that when the number of bubbles per time unit is too high, individual bubbles cannot be easily distinguished anymore, when multiple “frames” are analysed.

Subgoal 3: Able to study the developed method in an in vitro study and try imaging on a sequential way.

As earlier mentioned, this subgoal will not be implemented in this research phase. It will be discussed in the discussion of this chapter.

`3.3 Experimental set-up: concepts and subconcepts

In this paragraph the main aspects for the experimental set-up will be discussed, also with their main parameters.

Subgoal 1: Able to visualise the position of small particles on a single shot X-ray image.

Imaging system

Contrast

Subject contrast is the parameter for the difference in intensities that reaches the image receptor between by two adjacent regions.

Subject contrast (C_s) can be defined with the following formula:

$$C_s = \frac{A - B}{A} \tag{3.1}$$

Where A and B are respectively the number of photons after attenuation; and μ: the attenuation constant; and x: the thickness of the substance exposed by X-rays:

$$A = N_0 e^{-\mu x} \tag{3.2}$$

In the case of B: in this formula A can be replaced by B and x becomes $x \pm \Delta x$ (assuming the substance is identical for A and B).

The μ*, mentioned here, should not be confused with the dynamic viscosity (mentioned in paragraph 1.2).*

If the substances that get exposed in A and B are not identical, this can be implemented by changing the attenuation coefficient μ. This coefficient is energy and material dependent. For lower energies, the attenuation is normally high and drops with increasing photon energy. In figure 27 the attenuation for dry air and water, based on the data from the site of the National Institute of Standards and Technology (NIST) [2], is visualised. Out of these images, it can be seen that the attenuation in air for photons with a high energy is almost negligible compared to water. This means it is important to look for the right energy level where the best (object) contrast can be found.

The object contrast can be calculated with:

$$C_{object} = \frac{\Delta\mu}{\mu_{background}} = \frac{\mu_{air(bubble)} - \mu_{water}}{\mu_{water}} \tag{3.3}$$

[98]

In figure 28 the object contrast for air in water is visualised. In this case depth is neglected.

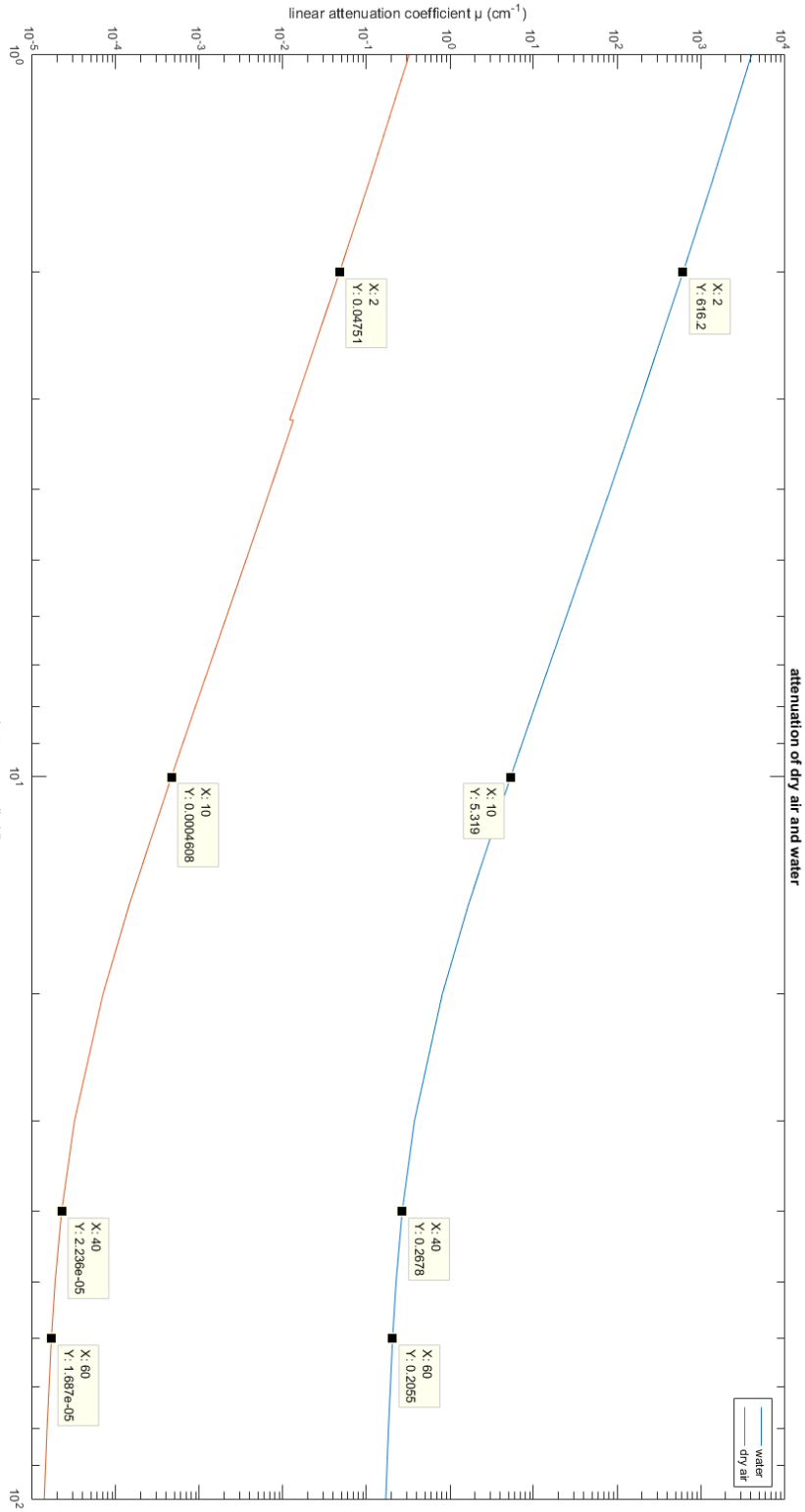

Figure 27: The linear attenuation coefficient μ as function of the phtonenergy for water and dry air based on the data of NIST [2]

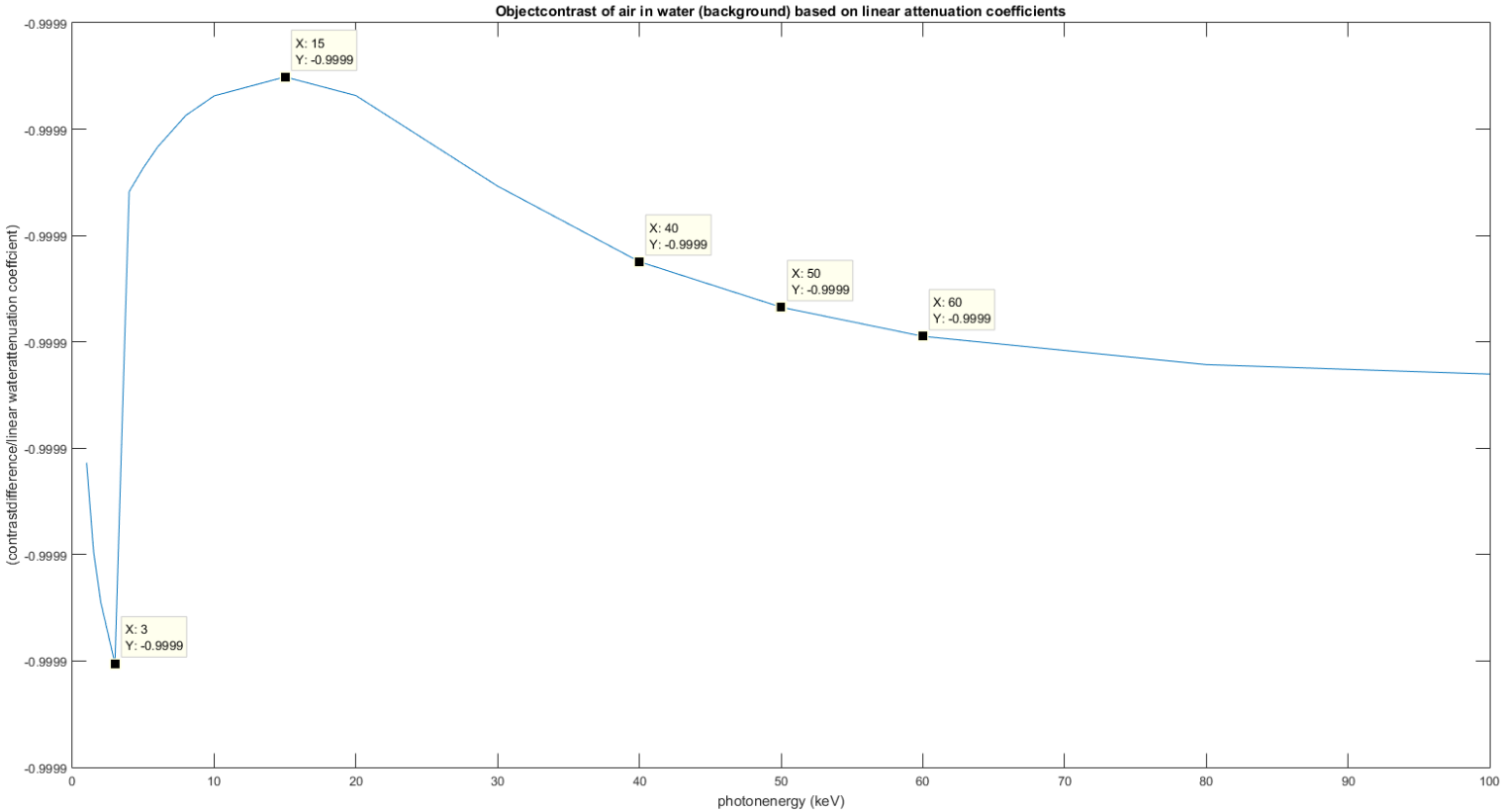

Figure 28: Object contrast of air in water for different photon energies, based on the attenuation coefficients of water and dry air (taken from NIST [2]).

In figure 28, we see that highest contrast exists around 20 keV. This is the range were the photo-electric effect and compton effect dominates [99].When using an X-ray tube producing a polyenergetic spectrum of photons, the average photon energy will be in general 1/3 to 1/2 of the maximum energy (V_{peak}). [100] Roughly speaking, this means the peak voltage inside the tube should be between 40 kV and 60 kV. Adjusting the peak voltage inside the tube will determine the contrast.

We have to keep to mind that in case we use "the 1/3 definition" we look also at the photons which have a low energy. However, in practise these photons will be filtered out.

In the case of the X-ray tube (Siemens Mobilett XP digital) in the ECTM, inherent filtering is 3.1 mm Al-equivalent (single tank plus the collimator) and the DAP measurement chamber increases the filtering with 0.4 mm. This means in total filtering is approximately 3.5 mm Al-equivalent.

An important notice is that, using this definition, the size of the bubble does not play a role in the formula. For incorporating the size, we can look at other types of contrast: the line-integral contrast and intensity contrast. Using the formulas for these contrasts, the attenuation coefficient μ is multiplied with the length of object inside the beam path (by which the photons are attenuated). And this is compared to the beam path length of the background. This is used as follows [98]:

$$C_{line-integral} = \frac{\Delta l}{l_{background}} \tag{3.4}$$

With: $l = \mu d$

$$C_{intensity} = \frac{\Delta I}{I_{background}} \tag{3.5}$$

With: $I = I_0 e^{-\mu d}$

[98]

As an example, we will look at a bubble of 3 mm in a cube of water (instead of a tube, because of the differences in beampath length caused by its shape) with a diameter of 25 mm and try to find the contrast for an average photon energy of 20 keV.

Filling in both *d*-values for water and air, we get:

$$C_{line-integral} = \frac{(2.2\mu_{water} + 0.3\mu_{air}) - 2.5\mu_{water}}{2.5\mu_{water}} \tag{3.6}$$

$$= \frac{(2.2\ \text{cm}\times(0.8096\ \text{cm}^2/\text{g})\times 0.998\ \text{g/cm}^3) + (0.3\ cm \times 0.0009/\text{cm}) - (2.5\times 0.8096\ \text{cm}^2/\text{g} \times 0.998\ \text{g/cm}^3)}{2.5\times(0.8096\ \text{cm}^2/\text{g})\times 0.998\ \text{g/cm}^3}$$

$$= \frac{1.78 - 2.02}{2.02} = -0.1198$$

$$C_{intensity} = 1 - e^{-0.242} = 0.2149$$

For this specific example, the intensity contrast is 0.2149 and the line-integral contrast is -0.1198.

mAs

Another factor of interest is the mAs. This is the current inside the tube multiplied by the exposure time and relates to the number of photons coming from the anode. It is important to choose an appropriate amount: too low mAs results in an underexposure and too high mAs in an overexposure. The exposure time will be as short as possible to get a high time ratio for the attenuation of the air bubble(s) in the direction of X-ray particle trajectory.

Besides this, the location of the detector and tube should be varied to get the best results:

- Source to image-receptor distance (SID): should be as small as necessary, the image quality will decrease with increasing SID further. The beam will spread over a larger area, meaning less photons per pixel. In order to compensate for an increase in SID, the mAs has to be increased or the collimation should be adjusted. Also, with increasing the SID rays become more parallel. This means there is an optimum distance, looking at parallel vs. divergent rays.
- Object to image receptor distance (OID): should be as small as possible. Increasing the OID will increase the magnification, but it will decrease the image quality. This means less details can be seen on the X-ray image.

Producing the bubbles

For the production of the particle(s) an air pump (laboport KNF LAB N86 KN.18, maximal operation pressure 2.4 bar g) can be used. The maximum permissible operating pressure was also tested with Manometer Auto off. The disadvantage of this pump is that produces a constant pressure. So, without any instrumentation the bubble production cannot be managed precisely. For this reason, a sort valve and a regulator was added which result in adjustable pressure. Another point of interest is the point of injection in the water. In order to produce small bubbles injection needles, up to 30g, with different internal diameters (: cross-sectional area) can be used. In table 4 the internal diameters for different needles are shown. However, this is just an indication of the size. There is tolerance between the different types of needles, because there are different manufacturers producing these needles.

The combination of adjusting the pressure towards the needles and changing the type of needle (based on the internal diameter) will result in different bubble diameters, see the paper of Oguz et al. [101].

Table 4: Needles with their internal diameter, found at [102]

Needles used for injection bubbles (gauge)	Internal diameter [11]
23	0.34
27	0.21
30	0.16

Figure 29: Two different needles used for the bubble injection

It should be noticed that its relation is complex, and therefore we will not discuss it in detail. Just its main ability to produce various bubbles will be used. Because we are only interested in a way to alter the bubble diameter.

The bubbles were injected first at a continuous cycle (meaning: without periodic blocking for example by a solenoid) in a tube with an internal diameter of approximately 50 mm. This tube was placed close to the detector (see figure 30). And the distance between the source and detector was varied for a short period of time to see its effect on the visibility of the bubbles.

X-ray images

The Mobilett XP Digital (Siemens) was used for taking X-ray images of the tubes (figure 30 and figure 31). These images were evaluated after they were taken, on the control panel of the device. This allowed us to adjust the settings for getting better results (looking at contrast and brightness of the bubbles with respect to the background).

Figure 30: Bubble injection in a water tube (bubble column), Two phase flow.

Figure 31: Smaller tube (23 mm inner diameter and 30 mm outer diameter) used for the later experiments

First X-ray images were taken with the tube, seen in figure 30. After a while also, a smaller tube (with a similar diameter as used in the optical experiments), see figure 31, was used to gain insight in the possibilities of using X-ray for the imaging of bubbles. The idea was that in a smaller tube the ratio water:bubbles changes, less water will attenuate the X-rays. Better results might be possible.

The different images were imported in Matlab and best results were chosen for discussing the options of this technique.

Subgoal 2: Able to visualise some kind of motion/movement on X-ray image(s).

Optimising for motion imaging

In advance of the previous mentioned concept (capturing (the position of) different bubbles on a single image) an additional requirement is made for the imaging of a bubble motion. For this, we need to choose the bubble injection rate. The way can be done by using a direct acting solenoid. The advantage is that the opening and closing rate can be varied for instance by a pulse generator.

This means that with an electronic circuit (see paragraph 2.4 and Appendix I) for opening and closing the air channel inside the solenoid, it is possible to inject bubbles one by one into the water.

Shutter and extra functional requirements

The next step is to find a way to capture the motion of an individual bubble in water. This can only be done if we at first are able to capture a bubble column on an X-ray image. We can use the same settings, but with a slightly increased exposure time (for the opening of the shutter) to see the bubble motion during exposure time. However, as already mentioned earlier an increase in exposure time will make it more difficult to get enough data for imaging the bubble, because the percentage of attenuation by only water will increase, while the attenuation by air will decrease. This results in less contrast, where it will be even more difficult to visualise small bubbles. The influence of this disadvantage might be less by implementing something which will not change this attenuation ratio that much. One way for doing so is to add a shutter in front of the X-ray tube. The idea is that the shutter will block X-rays during a part of the exposure time and opens for the same duration as the earlier taken single shot image (10 ms or longer limited by the systems response). Because the detector gets twice as much exposure, as in the previous case, and more attenuation of water, we have to correct for this. A possible way to do this is, to take a single shot with the same exposure time as the shutter is open and subtract this from the motion image.

For the shutter design itself there are some additional requirements that can be defined based on the location and functionality.

-sizes of the shutter:
The shutter should not hit the tube edge from below when solenoid is working (push mode) and fit between glass plate (DAP measurement chamber) and the tube (see figure 39).

- little energy transmission between the shutter and the X-ray arm, causing vibrations at the X-ray tube:
It should be avoided that the arm of the X-ray tube will vibrate due the rapid movement of the shutter. When vibration occurs, the original alignment is not the same as the position of the image field on the detector, causing artefacts on the X-ray image.

-timing opening and closing shutter:
This can be measured by sending light through during the operation of the shutter at closed-open-closed state. The time duration can be measured with a light sensitive sensor and an oscilloscope. This light must work based on DC-current to avoid interference of the measured signal of the shutter.

-lead plate sizes/thickness (half-value layer lead): the half-value layer of lead is dependent on the photon energy that has to be blocked.
This can be tested by opening and closing the shutter with the same X-ray settings to check its blocking ability.

-potential difficulty in timing:
initial exposure and bubble release.

Implementing these requirements led to the shutter design shown in figure 32.
For the shutter three plates were constructed in parallel:

- two plates on each side
- one shutter plate in the middle with a hole of 20×20 mm² a lead plate of $25\times25\times1$ mm³ attached in it.

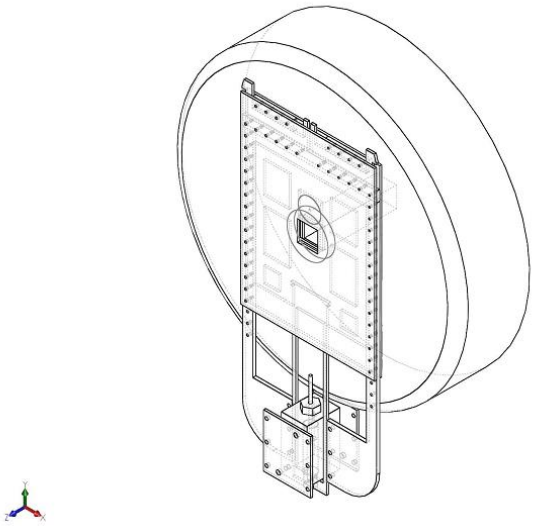

Figure 32: X-ray shutter design

The shutter plate was shifted between the two outer plates by a solenoid (Keyswitch SM2), with a maximum stroke of 25 mm.

The solenoid, itself, was driven by a h-bridge circuit (see Appendix I) and a pulse generator. Because the h-bridge works at a maximum voltage of 40 V, we chose to put the power supply in series (two times 20 Volts). In this way the current I was controlled. The pulse generator was set on different frequencies with a block pulse. The pulse was checked with an oscilloscope.

Testing the shutter

The shutters blocking ability and time properties can be tested, with the following methods.

The blocking effect of the shutter can be tested by putting the shutter in front of the X-ray tube in closed state, by switching the solenoid of. Followed by making an X-ray image with 56 kVp and 110 mA and an exposure time of 13 ms. The same imaging settings can be used at the open state of the shutter at (12 V, 0.5 A, 23 Ohm, 100 percent duty cycle). From both conditions X-ray images can be taken.

The shutter operation time (opening plus closing time) was tested with a light barrier. This consists of an orange LED used as photodiode for detecting the light and high power lead as light source (see Appendix I). By switching the shutter on and off in front of the light sheet the LED receive at intervals light which can be measured by connecting the LED on an oscilloscope. Further testing with this light barrier is needed to obtain useful results.

For further adjustment of the opening and closing time different compression springs were tested and modified in order to reach “a high frequent operation”. The maximum frequency that was reached for a fully open and closed state, at this moment, was 7 Hz. (see the discussion)

3.4 Results

First the results corresponding to the first subgoal will be mentioned. This is followed by showing the results of the second subgoal.

Subgoal 1

For the first subgoal the results of the X-ray experiments are shown in figures 34 to figure 37. The content of these X-ray images will be mentioned subsequently:
Figure 33 shows the injection of air bubbles via a 30g needle in a tube with an outer diameter of 6 mm (and an inner diameter of 5 mm).
The contrast of these bubbles was enhanced using the Matlab function 'imcontrast'.
This resulted in figure 34. The original image was fabricated by using the following X-ray settings: the peak voltage was 56 kV with a tube current of 230 mA and an exposure time of 12 ms.
This info could be obtained, by importing the images in Matlab and followed by using the function 'dicominfo'.

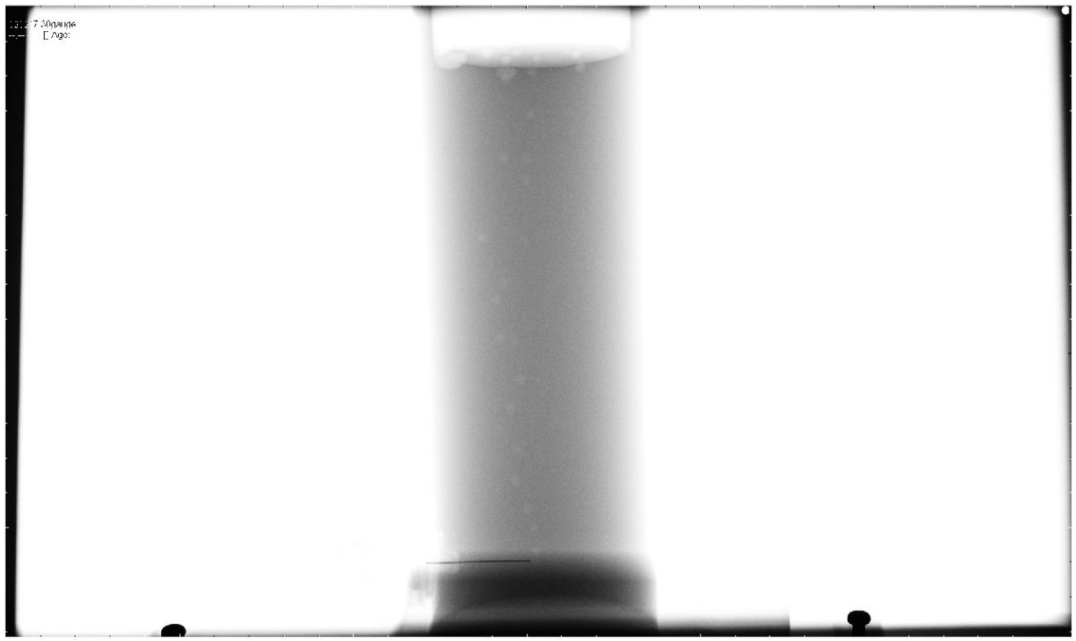

Figure 33: Grayscale image of air bubbles injected by a 30g needle in a tube, X-ray settings 56 kVp and 230 mA and an exposure time of 12 ms.

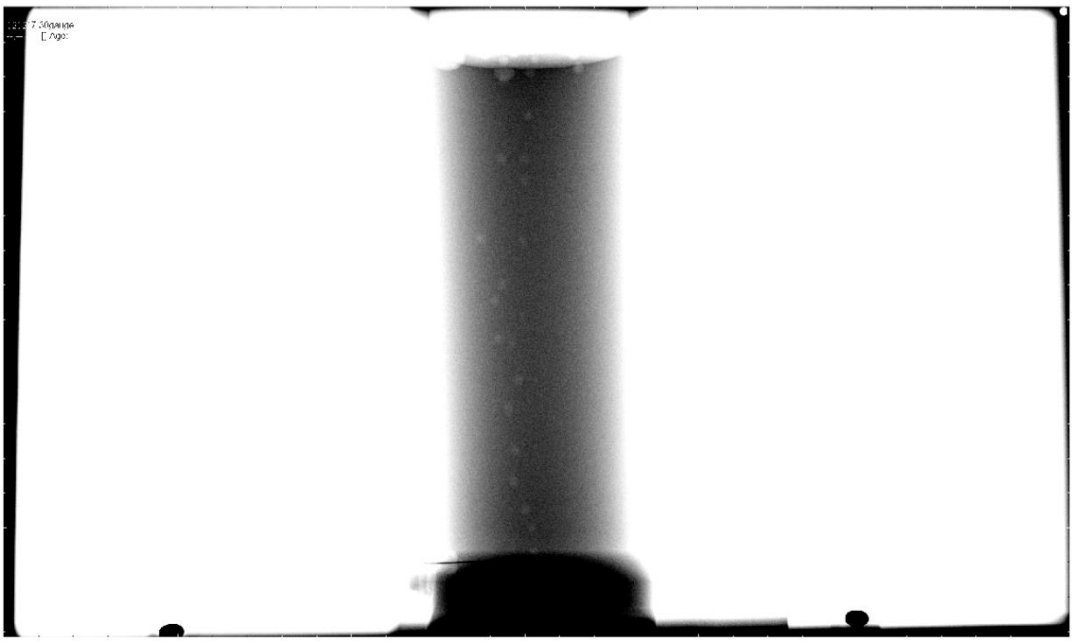

Figure 34: Improved contrast of the figure above with the Matlab function 'imcontrast'.

Figure 35 is an X-ray image showing the injection of bubbles in the smaller tube with an inner diameter of 23 mm and an outer diameter of 30 mm. This image was taken with a tube peak voltage of 56 kV, a tube current of 110 mA and an exposure time of 13 ms.

Figure 36 is, like figure 34, a contrast enhanced image of the original X-ray image (in this case figure 35).

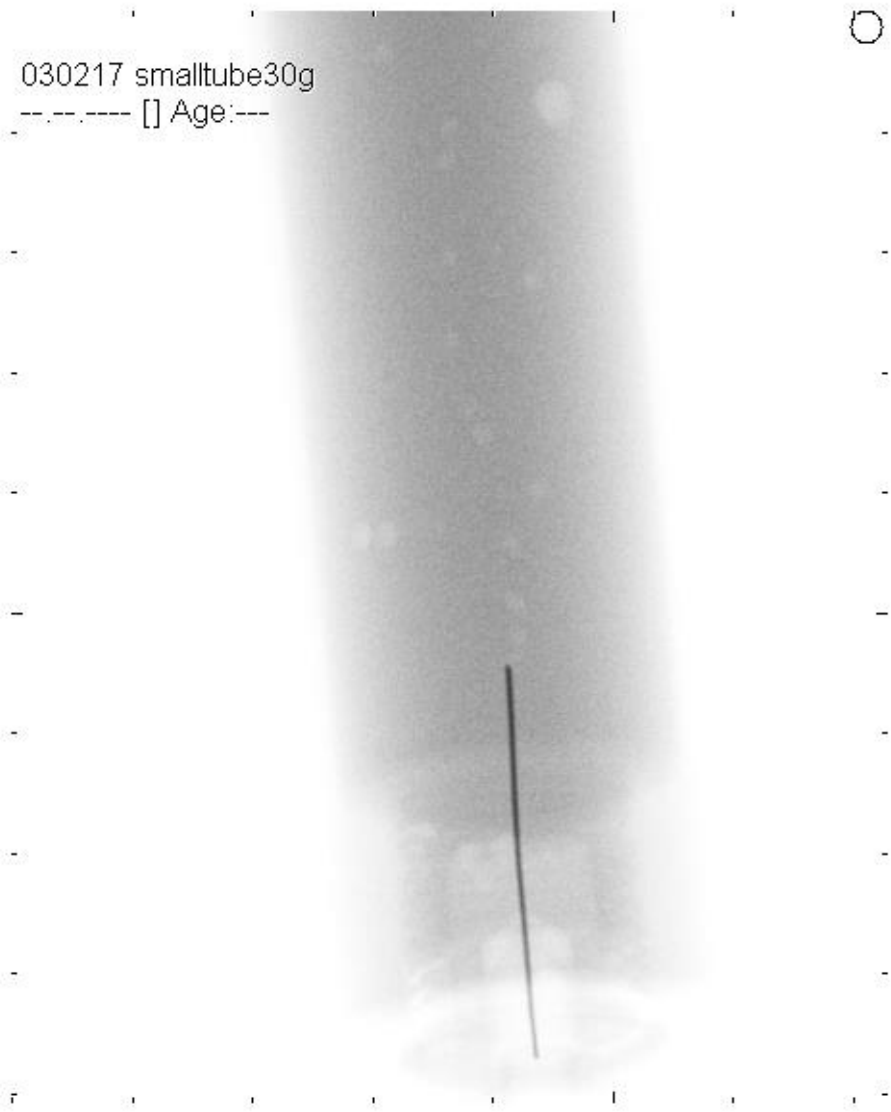

Figure 35: Grayscale image of bubbles injected by an 30g needle in a small tube , with X-ray settings: 56kVp and 110 mA and an exposure time of 13 ms.

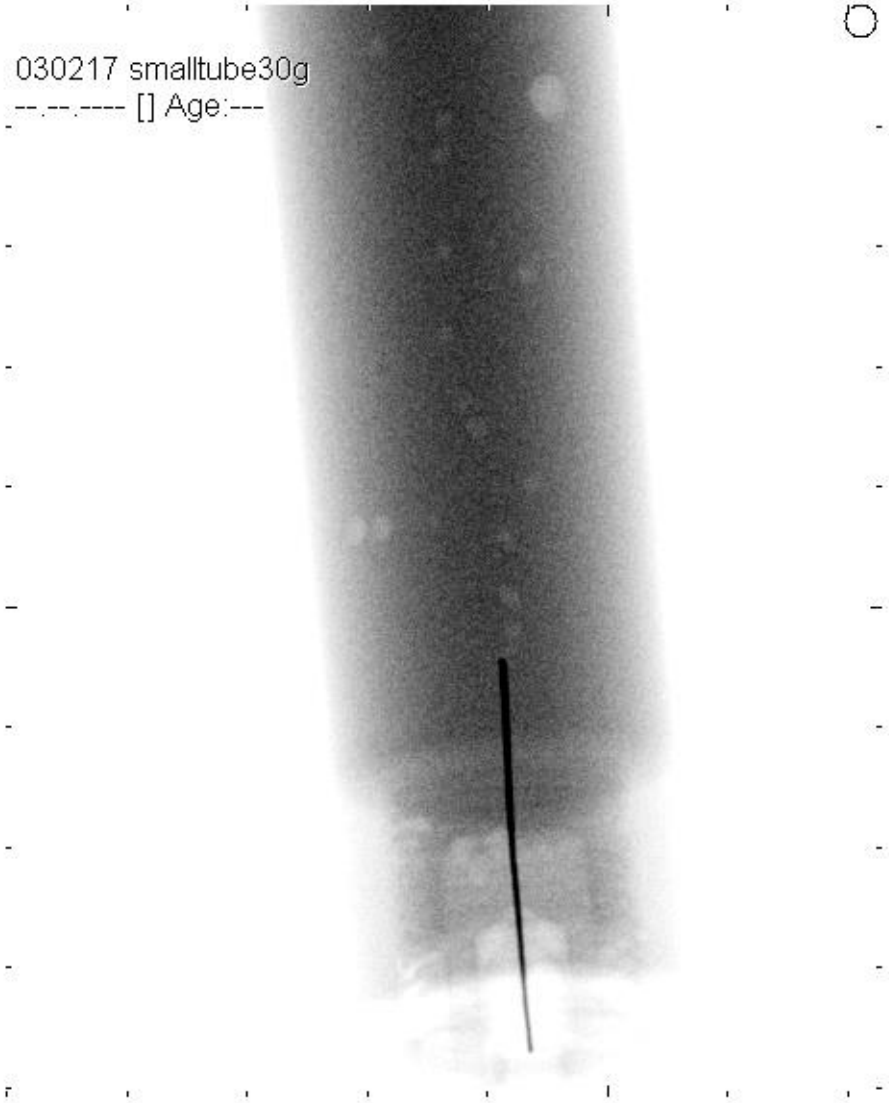

Figure 36: Adjusted contrast of the image above using the Matlab function 'imcontrast'.

Subgoal 2

For the second subgoal, a shutter was developed and build. This shutter in open and closed state can be seen in the figures 37 and 38. The design can be seen in figure 32.

Figure 37: Shutter at the open state

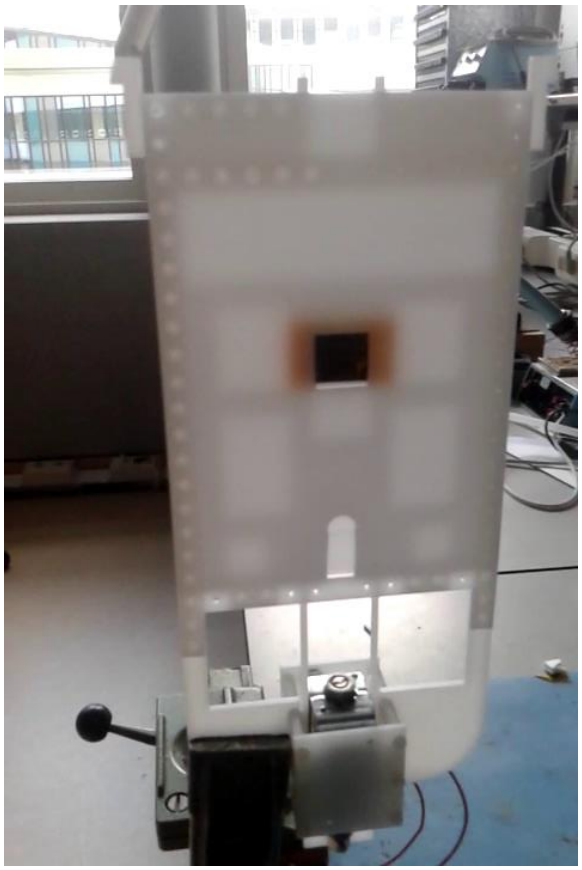

Figure 38: Shutter at the closed state.

Also, the operation of the shutter in front of the x-ray tube was shortly evaluated. This can be seen in figure 39.

Figure 39: Shutter in front of the X-ray tube (Mobilett)

A LED is used as photodiode was shortly used to check the opening and closing time of the shutter.

3.5 Discussion

In this paragraph the imaging of the bubbles, the segmentation and the shutter will be discussed. Finally, a possible correction for bigger bubbles will be elaborated.

Imaging of the bubbles

One of the most important aspects for looking at X-ray PIV is finding a balance between the tracer fidelity and the tracer visibility. Where for ”normal” PIV the main focus is within tracer fidelity, in X-ray PIV the main focus is the imaging itself. Because X-ray PIV based on absorption has a certain spatial resolution, which lies under the bubble diameter used for optical flow tracers.

Image segmentation

Based on the X-ray images (in the report: figures 34 and 36), we can conclude that with using the setting (56 kV and 2.76 mAs for the thick tube and 1.21 mAs for the thin tube) it is difficult to segment the bubbles from the background. Edge detection is an interesting feature for this. However, we should also notice that segmentation purely based on only one threshold (for example by Otsu’s method) will not be enough for these bubbles and the background. Regional segmentation might be a better option, like region growth and region merging (that can be based on a certain interval or percentage). An example of edge detection for low contrast images is discussed in the paper of McCarthy[103]. Also, different segmentation methods based on contour lines are possible for consideration.

Besides all this, contrast enhancement may be improved by background subtraction of a tube without bubbles (using the same X-ray settings). This can be done in future research.

Shutter

The quality of the shutter can be based on different aspects, such as the timing (opening and closing) and its blocking ability.

First, we discuss some aspects regarding to the operation time of the shutter. The solenoid is creating a magnetic field which pulls the armature in this field. We did some short experiments to have a quick look at the operation time, but these where not evaluated in detail. The total operation time (pull in plus drop down time) should be below 100 ms. For some applications, we can imagine that this operation time should be further reduced, for example where flow visualisation plays a role. The first results showed that the motion of the shutter was not periodic and the operation time was too long for PIV measurements. Therefore, we looked further at other options to increase the performance of the shutter.

By increasing the voltage of the solenoid, the magnetic field will be created faster. Because a high voltage (e.g. 40 V) creates a faster current build up. But to hold the pin at its position a lower voltage level (e.g. 12 V) is enough. After the current level, that is required for the pull in (in our case 0.5 A), is reached, the voltage can switched be to zero or even can be made negative, for a faster current drop. This is necessary to decrease the magnetic field. The measurement of the current level can be done by a shunt resistor. By using this method, with fast switching of voltage, the solenoid may operate faster.

We measured the inductance of the solenoid at two states: one with the metal pin out, where the inductance L=42 mH and one with the metal pin inside L=176 mH. This was measured at 50 Hz with the Hameg HM8118 LCR-Bridge. The resistance of the coil is approximately 26 ohm. The solenoid works on continue level at 12 V, which requires a current of 0.5 A. At higher voltage the duty cycle should be changed (50% at 24 V and 1 A etc).

Blocking X-rays

The main goal of the shutter is to block X-rays for a certain period of time. This can be done by metals like lead. This is used for instance in lead aprons for the purpose of radiation protection for people working with X-rays at the radiology department.

For checking its blocking ability, the half value layer can be calculated. Which means the thickness at which 50% of the incoming photons will be blocked, this is going exponentially.

For calculating the half value layer (HVL) formula (3.7) can be used:

$$HVL = \frac{0.693}{\mu} \tag{3.7}$$

[104]

(note: 0.693 is a rounded number of ln(2))

This μ should not be confused with the dynamic viscosity (see paragraph 1.2).

With respect to the attenuation of lead, we will look at the attenuation coefficient μ around the peak and average photon energies, because we are dealing with poly-energetic radiation. In practice, this means we look at the site of NIST for the $\frac{\mu}{\rho}$ value of lead at a photon energy of 20 keV and 60 keV: 86.36 cm²/g and 3.713 cm²/g [2].

The density of lead, found at The Engineering Toolbox [105],gives: 11340 kg/m³, which is equal to 11.3 g/cm³.

After five half value layers: $1 - 0.5^5 = 0.97$ is blocked, which is equal to 97%. Looking at the peak energy attenuation and putting everything together five HVL's corresponds to 0.8 mm lead.

We can compare lead also with other metals that are used to block X-rays, like tungsten. This can be done by looking at the densities of both and the $\frac{\mu}{\rho}$ values. Tungsten has a density of 19.3 g/cm³ and for lead, this is 11.3 g/cm³. After five half value layers 97 % of the incoming photons are blocked. For tungsten, the attenuation coefficient for 60 keV is: $\mu = \frac{\mu}{\rho} \times \rho = 3.713\ \mathrm{cm^2/g} \times 19.3\ \mathrm{g/cm^3} = 71.66\ \mathrm{cm^{-1}}$ and the half value layer in this case is: $\frac{\ln(2)}{\mu} = \frac{\ln(2)}{71.66\ \mathrm{cm^{-1}}} = 0.0097\ \mathrm{cm}$.

This results, for five halve value layers, in $0.0097 \times 5 = 0.05$ cm, which is required in the case of tungsten. This is not a plate thickness, which is widely available. A plate thickness of 1 mm is more regular. Therefore, we evaluate this thickness for choosing lead or tungsten.

The shutter plate weights approximately 68 g (incl. lead plate). The total shutter construction weights 470 g. When replacing the lead plate (1 mm thick) for tungsten, this would increase the ability for

blocking X-rays. However, the mass of the plate would be doubled in the case of using the same thickness. This means the actuation time for the solenoid would increase. Blocking for these energies 1 mm lead is enough, because five half value layers corresponding to 0.8 mm is lower than the 1 mm. For blocking higher energies tungsten can be considered. This would mean in addition that the electrodynamic response time should be optimised by decreasing it. The way to do this should be considered, when higher photon energies are used.

Optimising spring

First, we used a solenoid without an extra return spring. We observed directly that this results in a situation where the pin remains too long at the maximum stroke. To decrease this time a spring could be added to overcome the magnetic force. This means, besides the gravitational force, the reaction force of the spring can be added up with the intension the solenoid reaches faster its inactive state, which means the shutter closes faster. We, therefore, putted different springs (around the pin of the solenoid) inside the construction and observed via optical detection that the opening and closing of the shutter was not regular. This can be caused by the shape of the spring at both sides and its movement/rotation around the pin during operation.

For a more regular compression and extension, also meaning a more regular opening and closing time of the shutter, two disks were with four springs were attached and putted around the pin. With these springs, it was not possible to close the shutter completely at relative high frequencies Therefore, in future research different springs should be tried. Its operation time should be optimised for the shutter. If this done, the shutter will be able to block x-rays during a short period of time. Hence, multiple "X-ray frames" can be taken within one second.

After optimising the spring and the blocking effect of the shutter plate

There is no straightforward solution to visualise the small bubbles with the shutter. Therefore, it is better two separate this problem in different parts. First, the operation of the shutter must be analysed, by visualising the motion of a particle (which is radio-opaque/absorbing X-rays). This particle must be easy visualised on X-ray images. This can be done by analysing particles in air and moving the pin of the solenoid. Subsequently, seeding particles in a fluid can be visualised. In combination with all these observations, the right time parameters must be found. In the long run, these experiments can be continued by using bubbles.

<u>Possible correction for using bigger bubbles</u>

We used small particles in the model for tracer fidelity. However, we were not able to visualise these particles with X-ray. For estimating the particles size for tracer fidelity Stokes flow was used as assumption, because this is an analytical way to solve this problem.

At Stokes flow where particles' Reynolds number $Re_p \leq 1$ is:

$$Re_p = \frac{DV}{\nu} \tag{3.8}$$

(D= bubble diameter, V=velocity difference between the bubble and the field and ν=kinematic viscosity)

Where the drag force can be calculated with $F_{drag} = 3\pi\mu d(U_f - U_p)$, which is called the Stokes law.

This is based on Newtons second law: $F = ma$

We see, also, in this formula (3.8) that the Reynolds particle number has a linear relation with the particle diameter.

Because in the experiments (of chapter 3) we used bigger particles than required for tracer fidelity, we discuss a way to correct for the bubbles with a bigger diameter.

First, we have to consider that the drag force for bigger spherical particles (depending on the drag coefficient) is different from the Stokes flow (where $Re_p > 1$). In that case the drag coefficient (C_d) is based on Schiller Naumann:

$$C_d = \frac{24}{Re_p}(1 + 0.15Re_p^{0.687}) \text{ for } Re_p < 1000 \tag{3.9}$$

[106, 107]

$$C_d = 0.44 \text{ for } Re_p > 1000 \tag{3.10}$$

[107]

The drag force, in the case where $Re_p \gg 1$, is given by [108] in vector notation:

$$\vec{F}_{drag} = \frac{1}{2} C_d A_p |\vec{V}| \vec{V} \tag{3.11}$$

[108]

Where for a bubble particle the frontal area is: $A_p = \pi r_p^2$; and r_p: the radius of the particle.

We will continue with our 1-dimensional situation which is applied in this report. This model can be used as extension for Reynolds particle number higher than 1.

Let us assume that the drag force can be rewritten with the second law of Newton:

$$F_{drag} = ma \tag{3.12}$$

$$F_{drag} = f|u_f - u_p|(u_f - u_p) = ma \tag{3.13}$$

$$\text{And } f = \frac{1}{2} C_d A_p \tag{3.14}$$

For solving u_f, this gives two solutions:

$$u_f = \frac{\sqrt{f} u_p - \sqrt{a}\sqrt{m}}{\sqrt{f}} \tag{3.15}$$

and

$$u_f = \frac{\sqrt{f}u_p + \sqrt{a}\sqrt{m}}{\sqrt{f}} \tag{3.16}$$

Where $a = \frac{d^2 s_p}{dt^2}$ and $u_p = \frac{ds_p}{dt}$; and s_P: the postion of the particle; and t: time.

Filling this in for f gives:

$$u_f = \frac{\sqrt{\frac{1}{2}C_d A_p}\frac{ds_p}{dt} + \sqrt{\frac{d^2 s_p}{dt^2}}\sqrt{m}}{\sqrt{\frac{1}{2}C_d A_p}} \tag{3.17}$$

and

$$u_f = \frac{\sqrt{\frac{1}{2}C_d A_p}\frac{ds_p}{dt} - \sqrt{\frac{d^2 s_p}{dt^2}}\sqrt{m}}{\sqrt{\frac{1}{2}C_d A_p}} \tag{3.18}$$

These are the differential equations that describes the motion of the particle.

Because we can take photos at different moments of the big bubbles, we can also record the position and time of each bubble. With discretising the above equation, we can be able to estimate the fluid velocity at a specific position were the bubbles is on that recorded moment.

On time t1 the first order time discretisation with the forward difference is:

$$\left(\frac{ds_p}{dt}\right)_{t1} \approx \frac{S_{p,t1} - S_{p,t0}}{\Delta t} \tag{3.19}$$

And for the second order we can use the central differencing scheme:

$$\left(\frac{d^2 s_p}{dt^2}\right)_{t1} \approx \frac{S_{p,t2} - 2S_{p,t1} + S_{p,t0}}{(\Delta t)^2} \tag{3.20}$$

On point s1 and t1:

$$U_f \approx \frac{\sqrt{\frac{1}{2}C_d A_p}\frac{S_{p,t1}-S_{p,t0}}{\Delta t} - \sqrt{\frac{S_{p,t2}-2S_{p,t1}+S_{p,t0}}{(\Delta t)^2}}\sqrt{m}}{\sqrt{\frac{1}{2}C_d A_p}} \tag{3.21}$$

And

$$U_f \approx \frac{\sqrt{\frac{1}{2}C_d A_p}\frac{S_{p,t1}-S_{p,t0}}{\Delta t} + \sqrt{\frac{S_{p,t2}-2S_{p,t1}+S_{p,t0}}{(\Delta t)^2}}\sqrt{m}}{\sqrt{\frac{1}{2}C_d A_p}} \tag{3.22}$$

The next step is to add the buoyancy term, which is related to the density difference between the surrounding fluid and the gas inside the bubble.

$$F_{drag} + F_{buoyancy} = f\left|u_f - u_p\right|\left(u_f - u_p\right) + \frac{4}{3}\pi r_p^3\left(\rho_p - \rho_f\right)g = m\frac{d^2 s_p}{dt^2} \tag{3.23}$$

This means when we implement the first term:

$$\tfrac{1}{2}\pi r_p^2 \rho C_d\left|u_f - u_p\right|\left(u_f - u_p\right) + \tfrac{4}{3}\pi r_p^3\left(\rho_p - \rho_f\right)g = m\tfrac{d^2 s_p}{dt^2} \tag{3.24}$$

With

$$C_d = \tfrac{24}{Re_p}(1 + 0.15Re_p^{0.687} \text{ for } Re_p < 1000 \tag{3.25}$$

$$C_d = 0.44 \text{ for } Re_p > 1000 \tag{3.26}$$

And

$$Re = \frac{D\left(u_f - u_p\right)}{\mu_f/\rho} \tag{3.27}$$

For the X-ray system, bubbles can be used in the order of 1 mm.

Let us assume water has a velocity of 0.1 m/s

This means the particle Reynolds number is:

$$Re_p = \frac{1\times10^{-3}\times0.1}{10^{-6}} = 100$$

Solving the differential equation, mentioned in formula (3.24), analytically is difficult. Therefore, solving the equation with numerical techniques is a better option.

Here we start with a first guess for the fluid velocity. We can do this by assuming Poiseuille flow or by taking the average velocity in a tube.

We solve the formula for U_f with the help of Matlab. The next step is to substitute U_f in C_d en iterate till U_f converges. We can therefore define a certain maximum error of difference between two subsequently calculated fluid velocities of 1 percent for example.

The idea is to do this multiple times at different points along a tube. By using big bubbles in combination with the possible correction described here, we look if we can recognise a Poiseuille profile (parabolic profile).

Besides using bigger bubbles, we can also think about other imaging modalities like Magnetic resonance velocimetry (MRV) [109, 110], Ultrasound [111-113], 4D-CT, and the methods using PCI, which are discussed in the introduction of this chapter.

In vivo, Ultrasound (Echo-PIV) might be interesting for the peripheral vascular system. Where MRV and X-ray PIV might be used in deeper located blood vessels.

Looking at the development of X-ray systems, also new flat panel detectors are being developed, for example with the Direct conversion hybrid-organic X-ray detectors on metal oxide backplane (DiCoMo)-project [114]. With these developments on X-ray technique, X-ray PIV might not only be used at synchrotron facilities but also in clinic.
Or, we can even suggest that in the future smaller synchrotron radiation devices are available in hospitals.

3.6 Conclusion

The first subgoal was to visualise the position of small particles on a single X-ray image. This goal was reached. The second research goal was to visualise the motion of small particles on an X-ray image. This goal has not been reached yet. The shutter should be optimised for this purpose. Furthermore, this research shows it is still challenging to use X-ray imaging for Particle Image Velocimetry. More research is necessary to investigate the possibilities using state of the art X-ray detectors and newly developed tracer particles that have a better contrast than the used air bubbles.

Also, “the correction for bigger particles” should be investigated by doing experiments. Mainly, if this can gain insight in the local velocity of the fluid.

Besides, the use of X-ray, we see that different imaging modalities are also being developed. Each with its own advantage and disadvantage.

4. Future: connection with biomedical research

In this short chapter, we will mention some subjects, regarding to parameters that might also be used to quantify the progression or development of an arterial disease, like an AAA. We will shortly discuss the Pulse Wave Velocity (PWV) and the wall shear stress (wss).

4.1 Pulse Wave Velocity

As already mentioned in the introduction of this thesis an AAA is for a part related to pathophysiological mechanisms in the artery wall (figure 2). Another parameter that indicate some changes in the vascular wall is the Pulse Wave Velocity (PWV).

This is related to the elasticity/stiffness and defined as the velocity of a pressure wave in the artery of interest. The Pulse Wave Velocity can be calculated by the distance a pressure wave travels divided by the transit time between the two points marking this distance. [115]

In the literature, some important guidelines and documents show the importance of measuring the PWV:

In the guideline of 2007 from the European Society of Cardiology (ESC) and the European Society of Hypertension (ESH) about the management of arterial hypertension, PWV is mentioned as marker for predicting a cardiovascular disease [116]. In 2012 an expert consensus document was published about the measurement of PWV in daily practise [117]. Both documents are mentioned in the newer 2013 guideline for arterial hypertension [118]. In the new document of 2016 about prevention of cardiovascular disease, it is recommended that arterial stiffness should not be used as risk prediction indicator in the general population [119].
Also the American Heart Association published a scientific statement about this topic in 2015 [120].

All these publications show the importance of this research topic.

The PWV can be calculated with the Moens-Korteweg equation [115]:

$$PWV = \sqrt{\frac{Eh}{\rho d}} \tag{4.1}$$

if the elastic modulus (E), wall thickness (h) and the radius of the vessel lumen (d) is known and $h<<d$ [115].

The PWV is mentioned in literature on three levels: global PWV (measuring over a long arterial distance: carotid femoral PWV)[115] , regional PWV and the local PWV [115].

The global PWV is an average of the velocity over a long segment, where different (muscular and elastic) arteries can have different elasticities [115]. Because vascular pathologies, like an AAA, are not diffused along this segment this global PWV cannot give a detailed representation of the vessel wall elasticity at the location of the aneurysm.

One can imagine that local information about the stiffness of an artery (segment), requires a local measuring technique instead of the determination of the global PWV. Different aspects of measuring the PWV locally, are mentioned in the dissertation of Hermeling [115].

But first, some theoretical background is important about pulse propagation, which is given in the paper of Pedley (2003): discussing topics like the theory of pulse wave propagation, reflection based

on impedance mismatch. [121] Understanding these principles gives a better insight in factors that influence the PWV on different levels of the arterial system.

Now we have discussed some aspects why measuring at a local level is important and we will focus more on computing the PWV based on measurements.

Because we are talking here about Pulse Wave **Velocity**, distance and time measurements are the main parameters of interest. We will start by discussing the time measurements using wavefronts.

4.1.1 Algorithms used in the determination of PWV

In literature a couple of algorithms are discussed to calculate the pulse wave velocity, more specifically for the time estimation between two points of the subsequent pressure waves. This is called the pulse transit time (PTT) [122].

In the paper of Chiu et al. of 1991 several different algorithms were tried, analysing pressure waves. A good point in the wave for determining the PWV is the foot of the wave. The reason for using this part is that it is less sensitive to wave reflection(s). The best techniques for finding the foot of the wave/PWV were: the maximum of the second derivative and the intersecting tangent method. For more details about these different techniques analysed we refer to the paper of Chiu et al. [123].

In measurements also noise can have negative influence on obtaining results for the clinician or researcher, which may require filtering. This may also be the case with PWV-measurements.

In the paper of Hermeling et al., signal pre-processing as preparation step in determining the PWV was analysed. They found that, in the case of using distension waves, the threshold 20% method (20% between the min. and max. distension) and tangent method were better than using the maximum of the second derivative for finding the foot of the wave, including the effect of noise on the whole process. [124] For the details, we refer to the paper of Hermeling et al [124].

Also, new algorithms are developed and compared with these foot-to-foot algorithms for determining the PTT. These algorithms look not at the foot of the wave, but on the whole wave. These algorithms are cross correlation and least squares differencing methods. In the paper of Gaddum et al. the different methods are discussed, including recommendations which algorithm should be used in different situations. [125]

The foot-to-foot algorithm can be used in case the noise is lower than 10 percent of the signal magnitude and the temporal resolution is higher than 100 Hz. In the other cases, when these conditions are not satisfied, the so-called least squares differencing method can be used. [125]

This technique starts with clipping the distal wave at the minimum radius of curvature and maximum, normalising both waveforms (proximal and distal) and shifting the distal part along the proximal waveform. At each shift the sum of the squared difference can be calculated. In case this sum is minimal at a certain temporal shift the clipped waveform and proximal waveform is mostly the same, indicating the systolic rise. Finally, a second order polynomial is used to find the minimum. In this way, the transit time can be approximated. [125]

Another technique is the cross-correlation. This technique is based on finding the maximum correlation, by shifting the waveforms along each other and calculating the sum of the inner product at each “temporal shift”. It is advised to use cross correlation only when the distance between the measuring points is small and where noise and temporal resolution effects are a disadvantage for the quality of the early systolic ascending part of the wave. [125]

4.1.2 Off-set PWV technique

We have shortly looked at a method for measuring the Pulse Wave Velocity based on the piezo electric elements, which is partly based on(/also used in the paper in) the papers of Lopes et al. [126] and Pereira et al.[127]. In this papers probes were developed with these elements and the results analysed.[126, 127]

This technique is based on piezo-electric elements and with this technique the PWV can be obtained by measuring the distance and the time of arrival between both elements.

We build also a probe by 3D-printing with two piezo electric elements (Murata 7BB-20-6L0) on a distance of 24 mm from each other and tested it shortly on a tube.

An example is shown in the figure below. The time between both signals can be measured using cross-correlation for example.

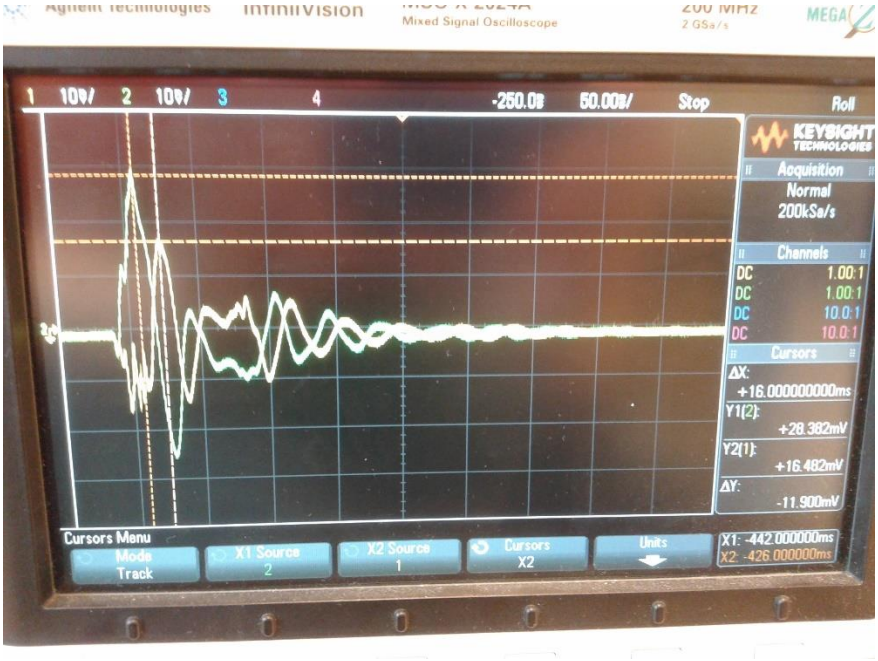

Figure 40: Oscilloscope: showing two pulse waves of both piezo electric elements on a small segment of a thin tube. PWV can be obtained by the distance between both elements, and the transit time (obtained by cross-correlation).

This technique could be analysed further in the future. The main problem for these type of probes is the type of fixing on a tube. One solution could be a sort sock which fixate the probe on the tube.

Besides, these type of techniques also much research is done based on measuring PWV with ultrasound [128] [115, 129] [130, 131] .

4.2 wall shear stress

Also, the wall shear stress is interesting for clinical research. One of the reasons is: wall shear stress (wss) is mentioned as parameter of interest in some vascular diseases. For example, in the paper of Boyd et al (2016) where a CFD study was done to simulate the wss at ruptured aneurysms of the abdominal aorta. [132] Another example is the paper of Arzani et al (2016) which looked at different wss parameters in aneurysmal flow.[133]

In 1998, a dissertation was published about modelling the wall shear stress in the main arteries. [134]

A different part of the clinical research is looking at measurement techniques for example based on sensors and imaging modalities.

Looking at imaging modalities, Van Disseldorp et al. published for example recently some papers about wall stress analysis using 4 D ultrasound [135] and the limiting field of view [136].

Before measurement techniques can be developed, we have to make an estimation of the expected wall shear on a theoretical base, based on a "simple theoretical approach" or with the help of computer simulations (CFD). We will shortly discuss some theoretical aspects.

First, we have to recall that the shear stress is defined is the dynamic viscosity multiplied by the velocity gradient at the wall (see paragraph 1.2). The last one is approximately equal to the gradient near the wall. We know from the introduction of this thesis that from the start a flow has to develop. This means the velocity profile in this segment will change.

And interpolation is needed to calculate the velocity near the wall and so the change in velocity in order to estimate the wall shear stress at a certain location. So, this means three things: the thickness of the boundary layer has to be known, the outer flow velocity. With this we can interpolate for finding the velocity at the wall, and thus the slope $\frac{du}{dy}$ of the velocity profile, which can result in an approximation of the wall shear stress.

A first approximation may be based on the boundary layer thickness. At the edge of the boundary layer, the velocity is approximately equal to the outer flow velocity. Hence, a linear interpolation can be made of the velocity gradient near the wall (see figure 41).

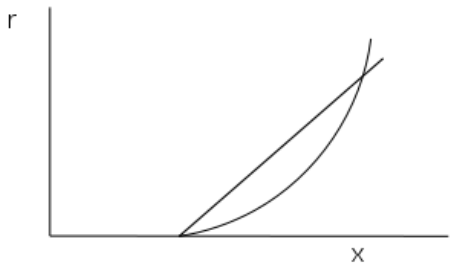

Figure 41: illustrating the difference in linear interpolation vs. quadratic interpolation (with r: distance to the wall and x: in the downstream direction). The slope of the linear interpolation is higher, resulting in a higher shear rate near the wall in respect to the quadratic approximation.

In the paper of Lou et al. different interpolation methods are analysed. Also, the pulsatile flow is analysed. The linear interpolation underestimates the shear rate, compared to the quadratic method. [137]

At the boundary layer the viscosity is taken into account, together with a no-slip condition (the velocity at the wall is zero). In this layer, the viscous effects are strongly present. As discussed by [138] the viscosity can be neglected in the main flow, this is the inviscid outer flow.

In the case of a plate, the laminar boundary layer thickness $\delta(x)$ increases in the downstream direction, denoted here with x. This can be approximated by:

$$\delta \sim \sqrt{\frac{\mu x}{\rho U_\infty}} = \sqrt{\left(\frac{\nu x}{U_\infty}\right)} \tag{4.2}$$

Where U_∞: the outer flow velocity

The factor in front of this term, in the case of a laminar boundary layer at a plate at zero incidence, is determined by Blasius and this gives [138]:

$$\delta_{99}(x) = 5\sqrt{\left(\frac{\nu x}{U_\infty}\right)} \tag{4.3}$$

This shows that the thickness grows with $\sqrt{x}$. [138] This δ_{99} is the place where 99 percent from the outer flow velocity is reached, looking from the wall of the plate, so $0.99U_\infty$.

We can use the formula for the boundary layer to approximate the wall shear stress. The formula for the wall shear stress [138]:

$$\tau_w = \mu\left(\frac{du}{dy}\right)_w \tag{4.4}$$

We can implement the boundary layer in the case of a plate in a linear way that [138]:

$$\frac{du}{dy} \sim \frac{U_\infty}{\delta} \tag{4.5}$$

Using this to approximate the wall shear stress gives [138]:

$$\tau_w \sim \mu U_\infty \sqrt{\left(\frac{U_\infty \rho}{\mu x}\right)} = \sqrt{\frac{\mu \rho U_\infty^3}{x}}. \tag{4.6}$$

This means τ_w is proportional to: $\frac{1}{\delta}$; $U^{3/2}$. If the boundary layer grows the wall shear stress decreases in the case of a plate. [138] We may use this knowledge in the case of flow in a pipe, because we do not know the analytical solution for the velocity profile at an undeveloped flow in a pipe.

Besides calculating the (approximation of) the wall shear stress, there are different techniques mentioned in literature for the measurement of wall shear stress/skin friction. [139]

One possible reason for this is that it is difficult to measure the wall shear stress without interrupting the flow at the wall. Different methods are used, such as Preston tubes [86] and hot wire anemometry [140]. Hot wire anemometry may be an interesting technique for using real-time data of the wall shear stress. However, we have to keep in mind that we are measuring in the velocity near the wall, so we need to interpolate. There we need modelling of the boundary layer if measuring inside the boundary layer is infeasible. This would be essential with flows in non-circular structures/without plates, if flows are non-steady/pulsatile etc. For hot wire anemometry there is published about corrections when measuring near the wall [141] and also the paper of Durst et al. discussed some aspects of measuring near the wall [142]. The reader is referred to these papers, when using this technique for determining the wall shear stress.

In 1990 a paper was published using a hot-film anemometer probe to determine the shear rate at an elastic tube model of the aorta. [143]

In the case we have fully developed laminar flow in a circular tube, we just can use the formula in the introduction for a Hagen-Poiseuille flow, and calculate the slope of the wall from figure 8, theoretically or used flow velocity measurements.

If we want to couple the data obtained by hydrogen bubble visualisation to a theoretical approximation/calculation, the imaging of the boundary layer is important: we need a camera with a high temporal resolution and a lens with sufficient magnification.

For getting the wall shear stress we need a good image resolution, because any irregularities created by the placement of the wire causes disturbances in the boundary layer. With this in mind the assumption of Hagen-Poiseuille flow may no longer be valid close to the wire.

For using tracer particles in-vivo, instead of bubbles in-vitro (as discussed in this thesis), we have to keep in mind that these particles (in-vivo) can cause side effects (like nephrotoxicity) and they have to be approved by the FDA/EMA.

With mentioning the different aspects, we see that measuring wall shear stress is challenging. But with a good theoretical basis about the fluid dynamic principles in elastic structures and its biological response in-vivo it should be able to get a good approximation of the wall shear stress in-vivo.

Here, velocity profiles near the wall can gain insight, equally important is the spatial resolution near the wall of imaging modalities.

For combining all parameters in the future, we have to look also to long term effects such as thrombus formation and neointima formation.

The most ideal situation is a way to measure non-invasively the wall shear stress, pulse wave velocity and fluid motion in one patient session. This makes it possible to connect these parameter in patient research and do an easy follow-up research.

In the case of the aorta abdominalis also studies of the wall shear stress are published, for example in the paper of Moore were MRI velocimetry was used with pixels of 1 by 1 mm [144]. In the case the boundary layer is thinner than 1 mm, it may be difficult to determine the slope of the velocity profile on the wall with enough accuracy.

Also, things like stent maps are being developed, published in the paper of Born et al. [145] Another example where stent grafts are studied is in the paper of Stefanov et al. [146]

With the aorta phantom, the same kind of studies can be used to analyse the difference effects of different stent grafts on the flow in arteries. In this way stent graft designs can be optimised for different patients, with a possible outcome of less complications during surgery and after stent graft implantation. This can be followed by in-vitro studies using specific type of sensors or tracer particles.

5. Acknowledgement

I want to thank shortly some people within the RAM-group. I want to thank the people from the technical staff, especially Hennie Kuipers. Thank you for your help during this project.
Also, I would like to thank Prof. Slump. Thank you for supervising me during my graduation period.

Appendix I

Matlab script for determining velocity at Poiseuille flow

```
clear all
%% water
D=0.026;
R=D/2;
r=-D/2:(D/2)/1000:D/2;
L=1.5;
Q_water=(5.9*10^-3)/60;
mu_water=1.002*10^-3;
delta_P=8*mu_water*L*Q_water/(pi*R^4);

for z=1:length(r)
    U(z)=(delta_P/(4*mu_water*L))*(R^2-r(z)^2);
end
plot(U,r)
```

Basset equation

$$\frac{\pi d_p^3}{6}\rho_p\frac{dU_p}{dt} = -3\pi\mu d_p V + \frac{\pi d_p^3}{6}\rho_f\frac{dU_f}{dt} - \frac{1}{2}\frac{\pi d_p^3}{6}\rho_f\frac{dV}{dt} - \left(\frac{3}{2}\right)d_p^2(\pi\mu\rho_f)^{1/2}\int_{t_0}^{t}\frac{dV}{d\xi}\frac{d\xi}{(t-\xi)^{1/2}}$$

[69]

Electric circuit

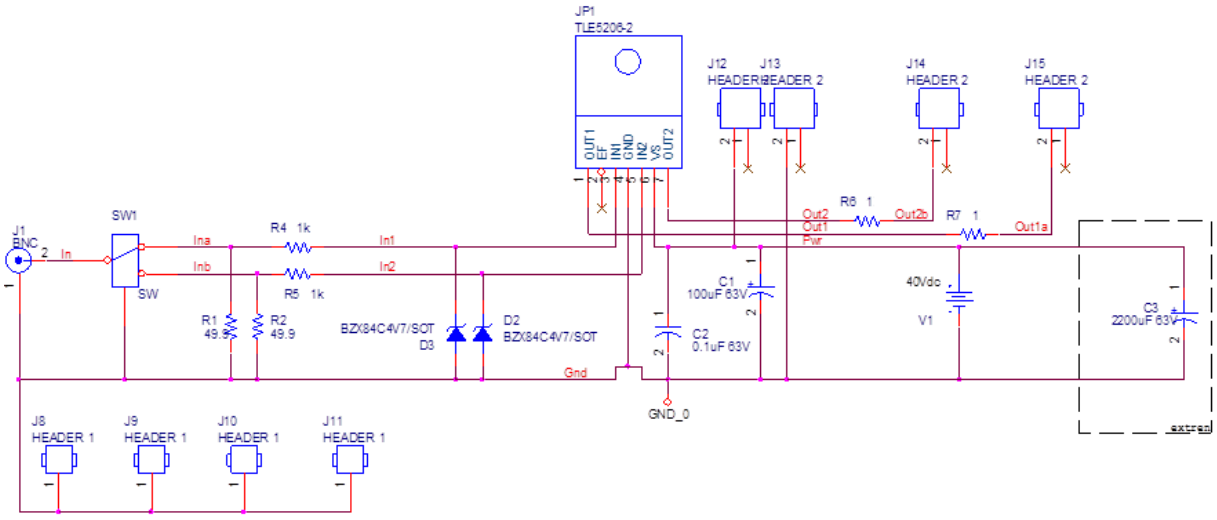

Figure A 1: electric circuit used for the hydrogen bubbles: J# are the connectors; SW1: the switch (normal/inverted); Vmax-power: 40 V; Pulse amplifier TLE 5206-2 with Icontinu,max: 5 A

Color spectrum High power LED at 4100 K, thermal pad temperature is 25 degrees Celsius.

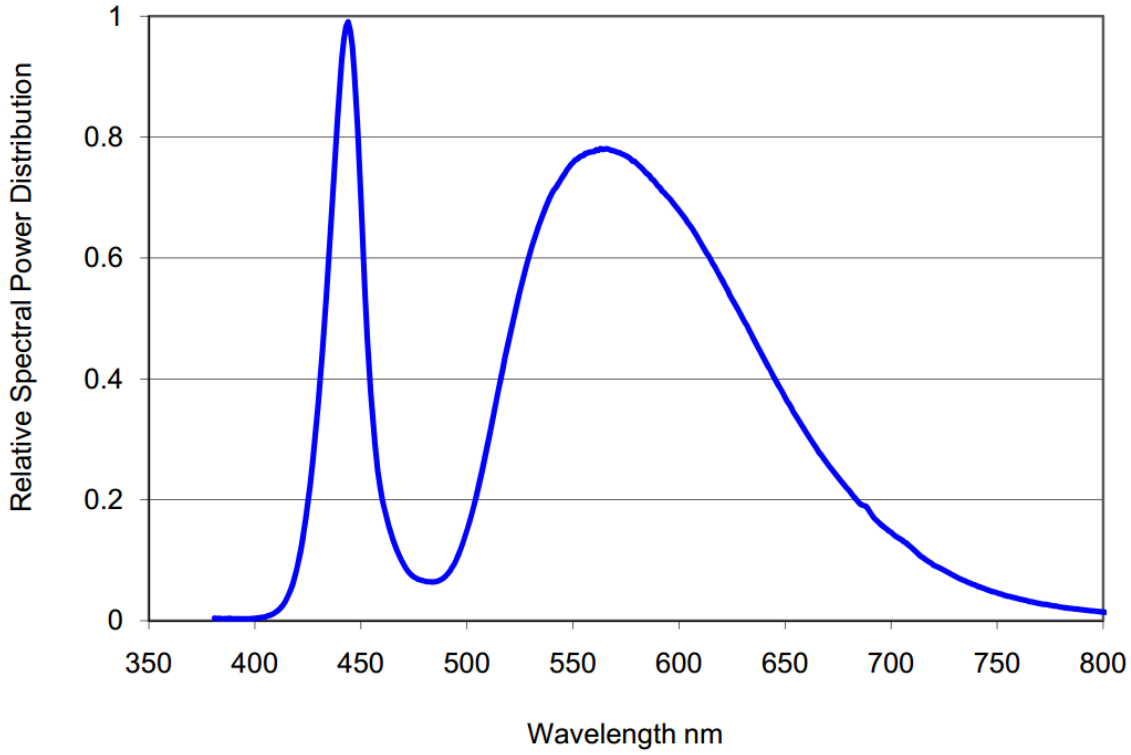

Figure A 2: Colorspectrum taken from the datasheet of the OPULENT REBEL-STAR-ES-NW200 High Brightness LED, Chip on Board, LUXEON Rebel ES Series, Neutral White, 120 °, 230 lm, 4100 K.

Mie plot 1 made with Mieplot version 4603 [85]

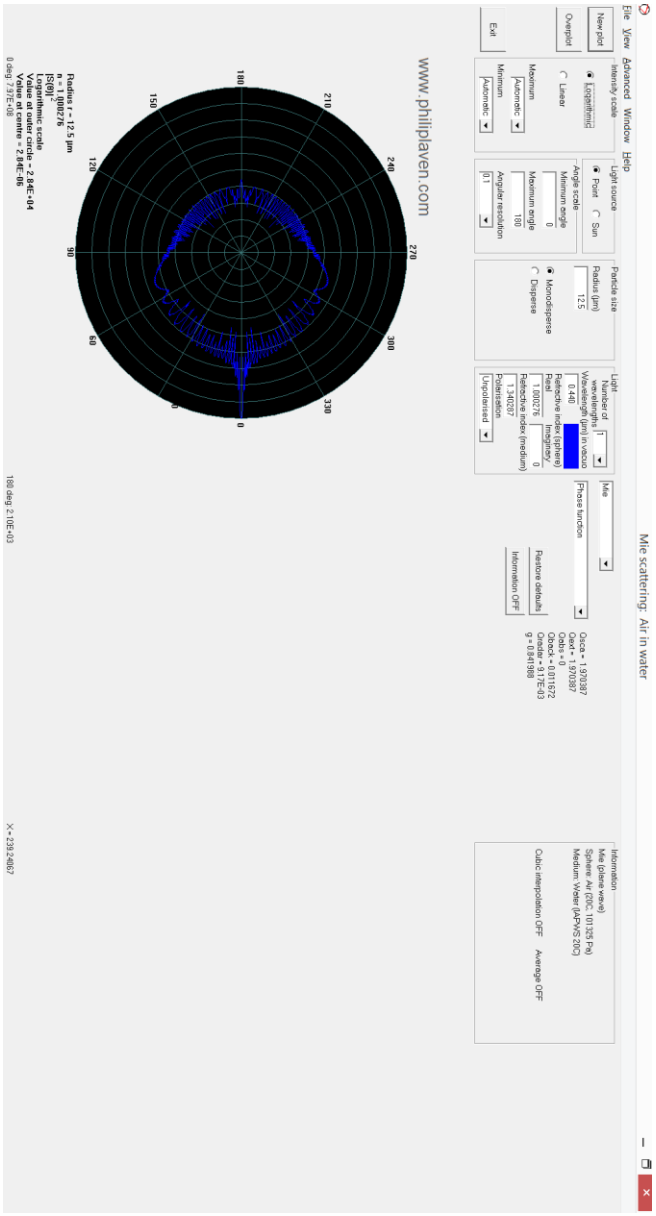

Figure A 3: logarithmic polar plot of an 25 µm air particle in water with incident light at 440 nm, made with Mieplot [83].

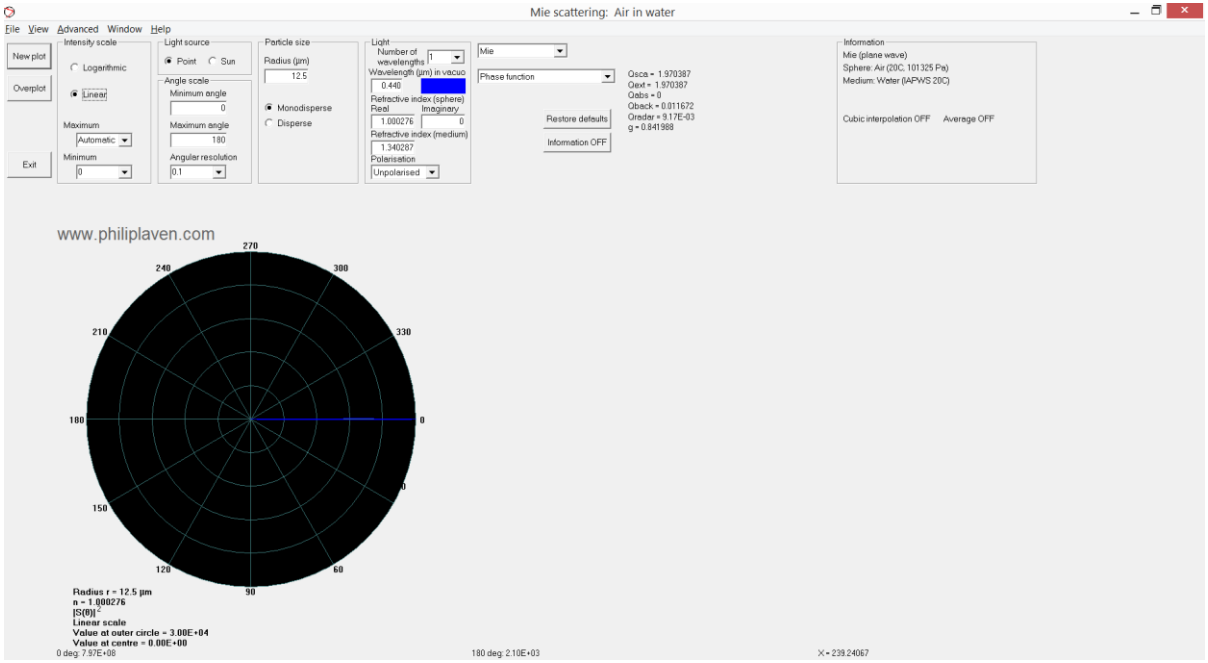

Figure A 4: linear polar plot of an 25 µm air particle in water with incident light at 440 nm, made with Mieplot [83].

Mie plot 2 made with Mieplot version 4603 [85]

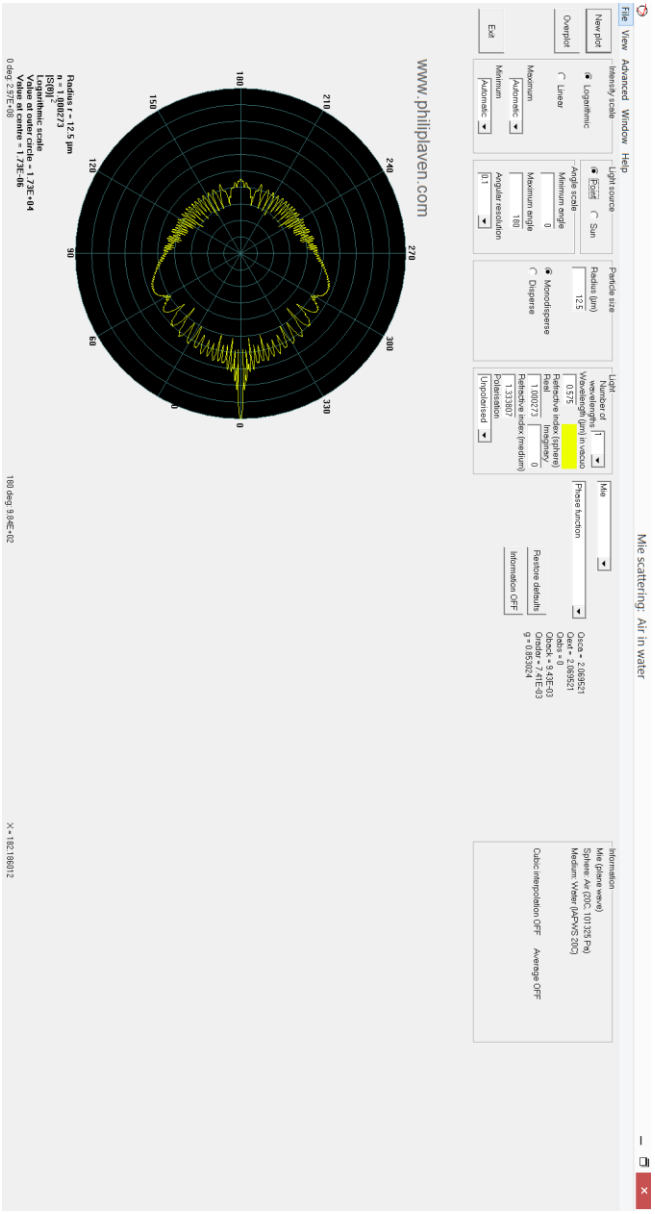

Figure A 5: logarithmic polar plot of an 25 µm air particle in water with incident light at 575 nm, made with Mieplot [83]

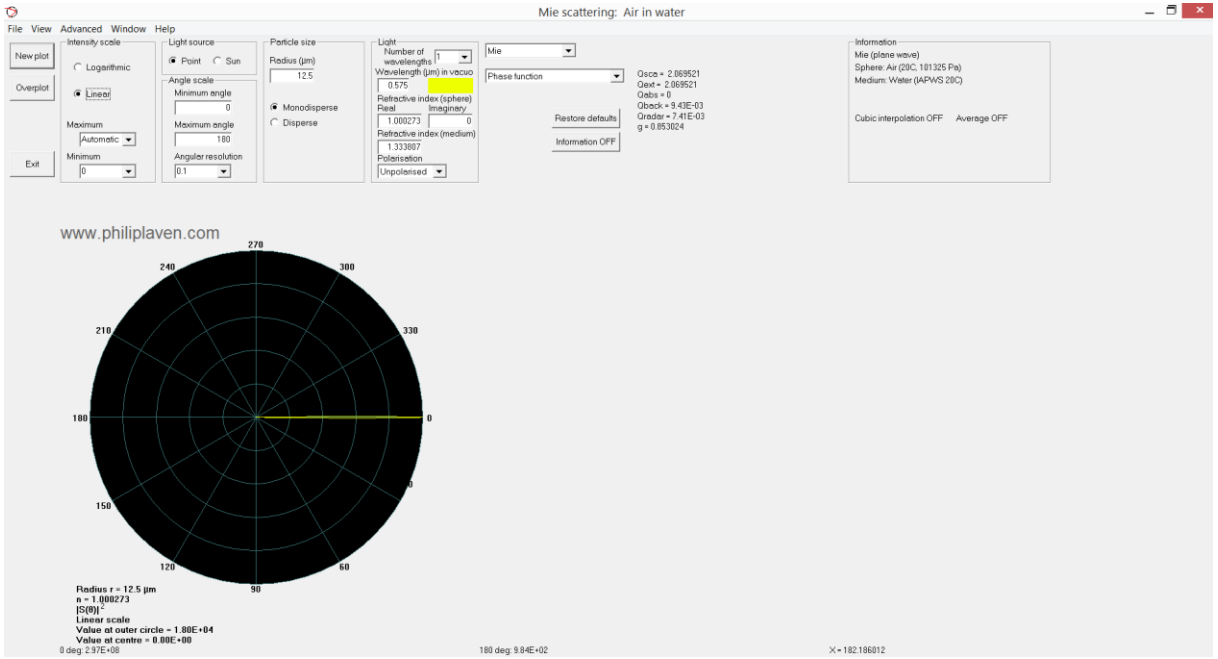

Figure A 6: linear polar plot of an 25 µm air particle in water with incident light at 575 nm, made with Mieplot [83].

Short example script for background subtraction

```
for i=1:1000 % number of frames

test(:,:,:,i)=f1_20p_1000frames(:,:,:,i)-f05_20p_1000frames(:,:,:,773); %
files with each frame subtracted by the backgorund without
% /minimal area of a timeline
i
end


implay(test) % play the movie with after the background subtraction
```

6. Bibliography

1. Schoretsanitis, N., et al., *A critical appraisal of endovascular stent-grafts in the management of abdominal aortic aneurysms.* Radiol Med, 2017. **122**(4): p. 309-318.
2. Hubbell, J. and S. Seltzer, *Tables of X-ray mass attenuation coefficients and mass energy-absorption coefficients (version 1.4).* National Institute of Standards and Technology, Gaithersburg, MD, 2004.
3. Powell, J.T., et al., *Meta-analysis of individual-patient data from EVAR-1, DREAM, OVER and ACE trials comparing outcomes of endovascular or open repair for abdominal aortic aneurysm over 5 years.* Br J Surg, 2017. **104**(3): p. 166-178.
4. de Hartstichting, *Hart- en vaatziekten in Nederland 2015: Cijfers over heden, verleden en toekomst.* December 2015.
5. Hill, M.A. *Embryology HM Practical- Blood Vessel Histology*. 2017; Available from: https://embryology.med.unsw.edu.au/embryology/index.php/HM_Practical_-_Blood_Vessel_Histology.
6. Junqueira, L.C., J. Carneiro, and E. Wisse, *Functionele histologie*. 11e dr., 2e opl. ed. 2010, Amsterdam :: Elsevier gezondheidszorg.
7. Toczek, J., J.L. Meadows, and M.M. Sadeghi, *Novel Molecular Imaging Approaches to Abdominal Aortic Aneurysm Risk Stratification.* Circ Cardiovasc Imaging, 2016. **9**(1): p. e003023.
8. Pearce, W.H. and V.P. Shively, *Inflammatory Pathogenesis and Pathophysiology of Abdominal Aortic Aneurysms*, in *Aortic Aneurysms: Pathogenesis and Treatment*, G.R. Upchurch and E. Criado, Editors. 2009, Humana Press: Totowa, NJ. p. 27-34.
9. Piechota-Polanczyk, A., et al., *The Abdominal Aortic Aneurysm and Intraluminal Thrombus: Current Concepts of Development and Treatment.* Front Cardiovasc Med, 2015. **2**: p. 19.
10. Toor, S.M., et al., *Aortic Aneurysms: OSR, EVAR, Stent-Grafts, Migration and Endoleak—Current State of the Art and Analysis*, in *Cardiovascular and Cardiac Therapeutic Devices*, T. Franz, Editor. 2014, Springer Berlin Heidelberg: Berlin, Heidelberg. p. 63-92.
11. Erbel, R., et al., *2014 ESC Guidelines on the diagnosis and treatment of aortic diseases: Document covering acute and chronic aortic diseases of the thoracic and abdominal aorta of the adult. The Task Force for the Diagnosis and Treatment of Aortic Diseases of the European Society of Cardiology (ESC).* Eur Heart J, 2014. **35**(41): p. 2873-926.
12. Kent, K.C., *Clinical practice. Abdominal aortic aneurysms.* N Engl J Med, 2014. **371**(22): p. 2101-8.
13. Kontopodis, N., et al., *The - Not So - Solid 5.5 cm Threshold for Abdominal Aortic Aneurysm Repair: Facts, Misinterpretations, and Future Directions.* Front Surg, 2016. **3**: p. 1.
14. Shelmerdine, S.C., J.L. Barber, and C.D. George, *Applications of Laplace's law in clinical medicine: a radiological pictorial review.* Br J Hosp Med (Lond), 2013. **74**(8): p. 451-6.
15. Vorp, D.A., *Biomechanics of abdominal aortic aneurysm.* J Biomech, 2007. **40**(9): p. 1887-902.
16. Fillinger, M.F., et al., *In vivo analysis of mechanical wall stress and abdominal aortic aneurysm rupture risk.* J Vasc Surg, 2002. **36**(3): p. 589-97.
17. Fillinger, M.F., et al., *Prediction of rupture risk in abdominal aortic aneurysm during observation: wall stress versus diameter.* J Vasc Surg, 2003. **37**(4): p. 724-32.
18. Maier, A., et al., *A comparison of diameter, wall stress, and rupture potential index for abdominal aortic aneurysm rupture risk prediction.* Ann Biomed Eng, 2010. **38**(10): p. 3124-34.
19. Duffy, J.M., R. Rolph, and M. Waltham, *Stent graft types for endovascular repair of abdominal aortic aneurysms.* Cochrane Database Syst Rev, 2015(9): p. CD008447.
20. Mohler III, E., *Patient information: abdominal aortic aneurysm (beyond the basics). UpToDate*.
21. Fults, D.W. and P. Taussky, *The Life of Rudolf Nissen: Advancing Surgery Through Science and Principle.* World Journal of Surgery, 2011. **35**(6): p. 1402-1408.
22. Cohen, J.R. and L.M. Graver, *The ruptured abdominal aortic aneurysm of Albert Einstein.* Surg Gynecol Obstet, 1990. **170**(5): p. 455-8.
23. Parodi, J.C., J.C. Palmaz, and H.D. Barone, *Transfemoral intraluminal graft implantation for abdominal aortic aneurysms.* Ann Vasc Surg, 1991. **5**(6): p. 491-9.
24. DICA, *DICA Jaarrapportage 2016*. 2016, Dutch Institute for Clincal Auditing (DICA).
25. Baas, A.F., et al., *The Glasgow Aneurysm Score as a tool to predict 30-day and 2-year mortality in the patients from the Dutch Randomized Endovascular Aneurysm Management trial.* J Vasc Surg, 2008. **47**(2): p. 277-81.
26. Nederlandse Vereniging voor Heelkunde (NVvH). *Diagnostiek en behandeling van het aneurysma van de abdominale aorta* Operatieve behandelingen van een aneurysma van de abdominale aorta 2009 [cited 2017 May 10]; Available from: https://richtlijnendatabase.nl/richtlijn/aneurysma_van_de_abdominale_aorta/operatieve_behandelingen_van_een_aaa.html.
27. Bohm, N., et al., *Objective risk-scoring systems for repair of abdominal aortic aneurysms: Applicability in endovascular repair?* European Journal of Vascular and Endovascular Surgery, 2008. **36**(2): p. 172-177.
28. Gore. *A Closer Look at ePTFE*. [cited 2017 May 11]; Available from: https://www.gore.com/about/technologies?view=section4
29. Kleinstreuer, C., et al., *Computational mechanics of Nitinol stent grafts.* J Biomech, 2008. **41**(11): p. 2370-8.

30. Rand, T., et al., *Quality improvement guidelines for imaging detection and treatment of endoleaks following endovascular aneurysm repair (EVAR).* Cardiovasc Intervent Radiol, 2013. **36**(1): p. 35-45.
31. Savlovskis, J., et al., *Aortic neck enlargement after endovascular aneurysm repair using balloon-expandable versus self-expanding endografts.* Journal of Vascular Surgery, 2015. **62**(3): p. 541-549.
32. Oberhuber, A., et al., *Comparison of aortic neck dilatation after open and endovascular repair of abdominal aortic aneurysm.* Journal of Vascular Surgery, 2012. **55**(4): p. 929-934.
33. Kalliafas, S., et al., *Stent-graft migration after endovascular repair of abdominal aortic aneurysm.* J Endovasc Ther, 2002. **9**(6): p. 743-7.
34. Antoniou, G.A., K. Bashaeb, and R. Ibrahim, *Nellix stent graft migration after endovascular aneurysm sealing.* Vasa, 2016. **45**(6): p. 505-507.
35. Resch, T., et al., *Distal migration of stent-grafts after endovascular repair of abdominal aortic aneurysms.* J Vasc Interv Radiol, 1999. **10**(3): p. 257-64; discussion 265-6.
36. Jacobs, T.S., et al., *Mechanical failure of prosthetic human implants: a 10-year experience with aortic stent graft devices.* J Vasc Surg, 2003. **37**(1): p. 16-26.
37. Kansal, V. and S. Nagpal, *Delayed Type IIIb endoleak secondary to graft fabric tear 7 years following implantation of a Medtronic Talent endovascular aortic device: A case report and review of the literature.* SAGE Open Med Case Rep, 2016. **4**: p. 2050313X16670304.
38. Teruya, T.H., et al., *Treatment of type III endoleak with an aortouniiliac stent graft.* Ann Vasc Surg, 2003. **17**(2): p. 123-8.
39. Hedayati, N., et al., *Prolonged renal artery occlusion after endovascular aneurysm repair: endovascular rescue and renal function salvage.* J Vasc Surg, 2008. **47**(2): p. 446-9.
40. Bastos Gonçalves, F.M., H.J.M. Verhagen, and R.J. Stolker, *Endovascular aortic repair: clarifying risk factors, complications and follow-up strategies = Endovasculaire aorta reparatie. Verduidelijking van risocofactoren, complicaties en follow-up strategieën*. 2015, [Erasmus Universiteit Rotterdam]: [Rotterdam] :.
41. Eckroth-Bernard, K., R. Garvin, and E. Ryer, *Current status of endovascular devices to treat abdominal aortic aneurysms.* Biomed Eng Comput Biol, 2013. **5**: p. 25-32.
42. Moore, J.E. and J.L. Berry, *Fluid and solid mechanical implications of vascular stenting.* Annals of Biomedical Engineering, 2002. **30**(4): p. 498-508.
43. Biswas, G., M. Breuer, and F. Durst, *Backward-Facing Step Flows for Various Expansion Ratios at Low and Moderate Reynolds Numbers.* Journal of Fluids Engineering, 2004. **126**(3): p. 362.
44. Shao, W. and M. Agelin-Chaab, *Turbulent Flows Over Forward Facing Steps With Surface Roughness.* Journal of Fluids Engineering, 2015. **138**(2): p. 021103-021103-12.
45. Iftekhar, H. and M. Agelin-Chaab, *Structure of Turbulent Flows Over Forward Facing Steps With Adverse Pressure Gradient.* Journal of Fluids Engineering, 2016. **138**(11): p. 111202-111202-12.
46. Suess, T., et al., *Shear accumulation as a means for evaluating risk of thromboembolic events in novel endovascular stent graft designs.* J Vasc Surg, 2016.
47. Walsh, P.W., S. Chin-Quee, and J.E. Moore, Jr., *Flow changes in the aorta associated with the deployment of a AAA stent graft.* Med Eng Phys, 2003. **25**(4): p. 299-307.
48. Chong, C.K. and T.V. How, *Flow patterns in an endovascular stent-graft for abdominal aortic aneurysm repair.* J Biomech, 2004. **37**(1): p. 89-97.
49. Chandra, S., et al., *Fluid-structure interaction modeling of abdominal aortic aneurysms: the impact of patient-specific inflow conditions and fluid/solid coupling.* Journal of biomechanical engineering, 2013. **135**(8): p. 81001.
50. Lin, S., et al., *Fluid-Structure Interaction in Abdominal Aortic Aneurysm: Effect of Modeling Techniques.* Biomed Res Int, 2017. **2017**: p. 7023078.
51. Oertel, H., *Prandtl's essentials of fluid mechanics*. 2nd ed. ed. Applied mathematical sciences ; v. 158; Applied mathematical sciences (Springer-Verlag New York Inc.) ; v. 158. 2004, New York :: Springer.
52. *The Engineering ToolBox*. Resources, Tools and Basic Information for Engineering and Design of Technical Applications! ; Available from: http://www.engineeringtoolbox.com/.
53. Westerhof, N., N. Stergiopulos, and M.I.M. Noble, *Snapshots of hemodynamics : an aid for clinical research and graduate education*. 2005, Springer: New York, NY :.
54. Cheng, C.P., R.J. Herfkens, and C.A. Taylor, *Comparison of abdominal aortic hemodynamics between men and women at rest and during lower limb exercise.* J Vasc Surg, 2003. **37**(1): p. 118-23.
55. *The Engineering ToolBox: Moody Diagram*. Available from: http://www.engineeringtoolbox.com/moody-diagram-d_618.html
56. Wilson, W.C., *Trauma, Volume 1 : Emergency Resuscitation, Perioperative Anesthesia, Surgical Management*. 2007, Informa Healthcare: Hoboken :.
57. Mateer, J.R., et al., *Effects of high infusion pressure and large-bore tubing on intravenous flow rates.* Am J Emerg Med, 1985. **3**(3): p. 187-9.
58. Noori, N., et al., *Blood flow in distal end-to-side anastomoses with PTFE and a venous patch: results of an in vitro flow visualisation study.* Eur J Vasc Endovasc Surg, 1999. **18**(3): p. 191-200.
59. Palmen, D.E.M., et al., *Analysis of the Flow in Stenosed Carotid-Artery Bifurcation Models - Hydrogen-Bubble Visualization.* Journal of Biomechanics, 1994. **27**(5): p. 581-590.

60. Chong, C.K., T.V. How, and P.L. Harris, *Flow visualization in a model of a bifurcated stent-graft.* Journal of Endovascular Therapy, 2005. **12**(4): p. 435-445.
61. Stamhuis, E.J., *Basics and principles of particle image velocimetry (PIV) for mapping biogenic and biologically relevant flows.* Aquatic Ecology, 2006. **40**(4): p. 463-479.
62. Schraub, F.A., et al., *Use of Hydrogen Bubbles for Quantitative Determination of Time-Dependent Velocity Fields in Low-Speed Water Flows.* Journal of Basic Engineering, 1965. **87**(2): p. 429-&.
63. Smits, A.J. and T.T. Lim, *Flow visualization : techniques and examples*. 2012, Imperial College Press: London :.
64. Groot-Jebbink, E., *Innovation in aortoilliac stenting, an in vitro comparison*. 2013, University of Twente.
65. Roobottom, C.A., J.D. Hunter, and P.J. Bryson, *The diagnosis of fatal gas embolism: detection by plain film radiography.* Clin Radiol, 1994. **49**(11): p. 805-7.
66. Kizer, K.W. and P.C. Goodman, *Radiographic manifestations of venous air embolism.* Radiology, 1982. **144**(1): p. 35-9.
67. Davis, W. and R.W. Fox, *An Evaluation of Hydrogen Bubble Technique for Quantitative Determination of Fluid Velocities within Clear Tubes.* Journal of Basic Engineering, 1967. **89**(4): p. 771-&.
68. Zoulias, E., et al., *A review on water electrolysis.* TCJST, 2004. **4**(2): p. 41-71.
69. Melling, A., *Tracer particles and seeding for particle image velocimetry.* Measurement Science and Technology, 1997. **8**(12): p. 1406-1416.
70. Shivamoggi, B.K., *Theoretical fluid dynamics*. Mechanics of fluids and transport processes, 0921-3805 ; 4; Mechanics of fluids and transport processes ; 0921-3805 4. 1985, Dordrecht :: Nijhoff.
71. Tropea, C., A.L. Yarin, and J.F. Foss, *Springer handbook of experimental fluid mechanics*. 2007, Springer Science+Business Media: Berlin :.
72. Dring, R.P., *Sizing Criteria for Laser Anemometry Particles.* Journal of Fluids Engineering-Transactions of the Asme, 1982. **104**(1): p. 15-17.
73. The Editors of Encyclopædia Britannica. *drag*. Encyclopædia Britannica 2017 [cited 2017 1 July]; Available from: https://www.britannica.com/science/drag.
74. Cimbala, J.M. and Y.A. Çengel, *Essentials of fluid mechanics : fundamentals and applications*. McGraw-Hill series in mechanical engineering; McGraw-Hill series in mechanical engineering. 2008, Boston :: McGraw-Hill Higher Education.
75. Hinds, W.C., *Aerosol technology: properties, behavior, and measurement of airborne particles*. 2012: John Wiley & Sons.
76. van Overbrüggen, T., et al., *Experimental analysis of particle sizes for PIV measurements.* Measurement Science and Technology, 2016. **27**(9): p. 094009.
77. Bossel, U. and B. Eliasson, *Energy and the hydrogen economy.* ABB Switzerland Ltd, 2003.
78. Raffel, M., *Particle image velocimetry : a practical guide*. 2007, Springer: Heidelberg ;.
79. Mei, R., *Velocity fidelity of flow tracer particles.* Experiments in Fluids, 1996. **22**(1): p. 1-13.
80. University of Twente, C.B.O., *Session 2: light scattering by small particles*. 2015.
81. TU Delft: the international Genetically Engineered Machine competition (iGEM). *Mie theorie*. 2016; Available from: http://2016.igem.org/Team:TU_Delft/Model/Theory#mie.
82. Friedlander, S.K., *Smoke, dust, and haze : fundamentals of aerosol dynamics*. 2nd ed. ed. Topics in chemical engineering; Topics in chemical engineering (Oxford University Press). 2000, New York :: Oxford University Press.
83. Atchison, D.A. and G. Smith, *Optics of the human eye*. 2000, Butterworth-Heinemann: Oxford ;.
84. Lahiri, A., *Basic optics : principles and concepts*. 2016, Elsevier: Amsterdam, Netherlands :.
85. Laven, P., *MiePlot v.4.6.03, 22 March 2017.* A computer program for scattering of light from a sphere using Mie theory & the Debye series, available at: "http://www. philiplaven. com/MiePlot.htm" 2017.
86. Tavoularis, S., *Measurement in fluid mechanics*. 2005, Cambridge ;: Cambridge University Press.
87. Lu, L.J. and C.R. Smith, *Image-Processing of Hydrogen Bubble Flow Visualization for Determination of Turbulence Statistics and Bursting Characteristics.* Experiments in Fluids, 1985. **3**(6): p. 349-356.
88. Bruneau, S.D. and W.R. Pauley, *Measuring unsteady velocity profiles and integral parameters using digital image processing of hydrogen bubble timelines.* Journal of Fluids Engineering-Transactions of the Asme, 1995. **117**(3): p. 331-340.
89. Lewis, R., *Medical applications of synchrotron radiation x-rays.* Phys Med Biol, 1997. **42**(7): p. 1213-43.
90. Kastengren, A. and C.F. Powell, *Synchrotron X-ray techniques for fluid dynamics.* Experiments in Fluids : Experimental Methods and their Applications to Fluid Flow, 2014. **55**(3): p. 1-15.
91. Kim, G.B. and S.J. Lee, *X-ray PIV measurements of blood flows without tracer particles.* Experiments in Fluids, 2006. **41**(2): p. 195-200.
92. Jung, S.Y., et al., *Time-resolved X-ray PIV technique for diagnosing opaque biofluid flow with insufficient X-ray fluxes.* Journal of Synchrotron Radiation, 2013. **20**(3): p. 498-503.
93. Park, H., et al., *Measurement of real pulsatile blood flow using X-ray PIV technique with CO2 microbubbles.* Scientific Reports, 2015. **5**(1).
94. Millard, T.P., et al., *Evaluation of microbubble contrast agents for dynamic imaging with x-ray phase contrast.* Sci Rep, 2015. **5**: p. 12509.
95. Lewis, R.A., *Medical phase contrast x-ray imaging: current status and future prospects.* Phys Med Biol, 2004. **49**(16): p. 3573-83.

96. Fu, S., P.H. Biwole, and C. Mathis, *Numerical and experimental comparison of 3D Particle Tracking Velocimetry (PTV) and Particle Image Velocimetry (PIV) accuracy for indoor airflow study.* Building and Environment, 2016. **100**: p. 40-49.
97. Lee, S.J. and S. Kim, *Simultaneous measurement of size and velocity of microbubbles moving in an opaque tube using an X-ray particle tracking velocimetry technique.* Experiments in Fluids, 2005. **39**(3): p. 492-497.
98. Fessler, J. *X-ray Imaging: noise and SNR* 2009; Available from: https://web.eecs.umich.edu/~fessler/course/516/l/c6-noise.pdf.
99. Bos, A.J.J., F.S. Draaisma, and W.J.C. Okx, *Inleiding tot de stralingshygiëne*. 2007, Den Haag :: Sdu Uitgevers.
100. Bushberg, J.T., *The essential physics of medical imaging*. 2nd ed. ed. 2002, Philadelphia :: Lippincott Williams & Wilkins.
101. Oguz, H.N. and A. Prosperetti, *Dynamics of Bubble-Growth and Detachment from a Needle.* Journal of Fluid Mechanics, 1993. **257**: p. 111-145.
102. *Syringe Needle Gauge Chart*. 2017; Available from: http://www.sigmaaldrich.com/chemistry/stockroom-reagents/learning-center/technical-library/needle-gauge-chart.html.
103. McCarthy, S., T.C. Miller, and I.N. Bankman, *Segmentation algorithm for objects with very low edge contrast [5608-19].* PROCEEDINGS- SPIE THE INTERNATIONAL SOCIETY FOR OPTICAL ENGINEERING, 2004. **5608**: p. 162-168.
104. NDT Resource Center. *Half-Value Layer* 2017; Available from: https://www.nde-ed.org/EducationResources/CommunityCollege/Radiography/Physics/HalfValueLayer.htm.
105. *The Engineering ToolBox: Metals and Alloys-Densities.*
106. Kim, J.-H., et al., *Uncertainty analysis of flow rate measurement for multiphase flow using CFD.* Acta Mechanica Sinica, 2015. **31**(5): p. 698-707.
107. Mann, H., et al., *Analytical description of the unsteady settling of spherical particles in Stokes and Newton regimes.* Granular Matter, 2015. **17**(5): p. 629-644.
108. Brennen, C.E., *Fundamentals of multiphase flow*. 2005, Cambridge [England] ;: Cambridge University Press.
109. Elkins, C.J. and M.T. Alley, *Magnetic resonance velocimetry: applications of magnetic resonance imaging in the measurement of fluid motion.* Experiments in Fluids, 2007. **43**(6): p. 823-858.
110. Neville, R.F., et al., *Hemodynamic Comparison of Differing Anastomotic Geometries Using Magnetic Resonance Velocimetry.* Journal of Surgical Research, 2011. **169**(2): p. 311-318.
111. Poelma, C., et al., *3D Flow reconstruction using ultrasound PIV.* Experiments in Fluids, 2011. **50**(4): p. 777-785.
112. Niu, L., et al., *Ultrasonic particle image velocimetry for improved flow gradient imaging: algorithms, methodology and validation.* Phys Med Biol, 2010. **55**(7): p. 2103-20.
113. Kheradvar, A., et al., *Echocardiographic particle image velocimetry: a novel technique for quantification of left ventricular blood vorticity pattern.* J Am Soc Echocardiogr, 2010. **23**(1): p. 86-94.
114. *DiCoMo: Direct conversion hybrid-organic X-ray detectors on metal oxide backplane (DICoMo) project*. Available from: http://dicomo-project.eu/.
115. Hermeling, E., *Local pulse wave velocity determination : the arterial distension waveform from foot to crest*. 2009, Maastricht University.
116. Mancia, G., et al., *2007 Guidelines for the Management of Arterial Hypertension: The Task Force for the Management of Arterial Hypertension of the European Society of Hypertension (ESH) and of the European Society of Cardiology (ESC).* Journal of hypertension, 2007. **25**(6): p. 1105-87.
117. Van Bortel, L.M., et al., *Expert consensus document on the measurement of aortic stiffness in daily practice using carotid-femoral pulse wave velocity.* J Hypertens, 2012. **30**(3): p. 445-8.
118. Mancia, G., et al., *2013 ESH/ESC guidelines for the management of arterial hypertension: the Task Force for the Management of Arterial Hypertension of the European Society of Hypertension (ESH) and of the European Society of Cardiology (ESC).* Eur Heart J, 2013. **34**(28): p. 2159-219.
119. Piepoli, M.F., et al., *2016 European Guidelines on cardiovascular disease prevention in clinical practiceThe Sixth Joint Task Force of the European Society of Cardiology and Other Societies on Cardiovascular Disease Prevention in Clinical Practice (constituted by representatives of 10 societies and by invited experts)Developed with the special contribution of the European Association for Cardiovascular Prevention & Rehabilitation (EACPR).* European Heart Journal, 2016. **37**(29): p. 2315-2381.
120. Townsend, R.R., et al., *Recommendations for Improving and Standardizing Vascular Research on Arterial Stiffness: A Scientific Statement from the American Heart Association.* Hypertension, 2015. **66**(3): p. 698-722.
121. Pedley, T.J., *Mathematical modelling of arterial fluid dynamics.* Journal of Engineering Mathematics, 2003. **47**(3-4): p. 419-444.
122. Vardoulis, O., T.G. Papaioannou, and N. Stergiopulos, *Validation of a novel and existing algorithms for the estimation of pulse transit time: advancing the accuracy in pulse wave velocity measurement.* Am J Physiol Heart Circ Physiol, 2013. **304**(11): p. H1558-67.
123. Chiu, Y.C., et al., *Determination of pulse wave velocities with computerized algorithms.* American heart journal, 1991. **121**(5): p. 1460-70.
124. Hermeling, E., et al., *Measurement of local pulse wave velocity: effects of signal processing on precision.* Ultrasound Med Biol, 2007. **33**(5): p. 774-81.

125. Gaddum, N.R., et al., *A Technical Assessment of Pulse Wave Velocity Algorithms Applied to Non-invasive Arterial Waveforms.* Annals of Biomedical Engineering, 2013. **41**(12): p. 2617-2629.
126. Lopes, T.M.P. and C. Correia, *Double Probe Based in Piezoelectric Sensors for Local Pulse Wave Velocity Assessment.* 2012 Ieee 2nd Portuguese Meeting in Bioengineering (Enbeng), 2012.
127. Pereira, H.C., et al., *Characterization of a double probe for local pulse wave velocity assessment.* Physiol Meas, 2010. **31**(11): p. 1449-65.
128. Eriksson, A., et al., *Arterial pulse wave velocity with tissue Doppler imaging.* Ultrasound in Medicine and Biology, 2002. **28**(5): p. 571-580.
129. Shahmirzadi, D., R.X. Li, and E.E. Konofagou, *Pulse-Wave Propagation in Straight-Geometry Vessels for Stiffness Estimation: Theory, Simulations, Phantoms and In Vitro Findings.* Journal of Biomechanical Engineering-Transactions of the Asme, 2012. **134**(11).
130. Messas, E., M. Pernot, and M. Couade, *Measuring the elasticity of the arterial wall: state of the art and perspectives.* Journal De Radiologie Diagnostique Et Interventionnelle, 2013. **94**(5): p. 577-585.
131. Li, F.B., et al., *High frame rate and high line density ultrasound imaging for local pulse wave velocity estimation using motion matching: A feasibility study on vessel phantoms.* Ultrasonics, 2016. **67**: p. 41-54.
132. Boyd, A.J., et al., *Low wall shear stress predominates at sites of abdominal aortic aneurysm rupture.* J Vasc Surg, 2016. **63**(6): p. 1613-9.
133. Arzani, A. and S.C. Shadden, *Characterizations and Correlations of Wall Shear Stress in Aneurysmal Flow.* Journal of Biomechanical Engineering-Transactions of the Asme, 2016. **138**(1).
134. Gijsen, F.F., *Modeling of wall shear stress in large arteries*. 1998, Technische Universiteit Eindhoven: Eindhoven.
135. van Disseldorp, E.M., et al., *Patient Specific Wall Stress Analysis and Mechanical Characterization of Abdominal Aortic Aneurysms Using 4D Ultrasound.* Eur J Vasc Endovasc Surg, 2016. **52**(5): p. 635-642.
136. van Disseldorp, E.M., et al., *Influence of limited field-of-view on wall stress analysis in abdominal aortic aneurysms.* J Biomech, 2016. **49**(12): p. 2405-12.
137. Lou, Z., W.J. Yang, and P.D. Stein, *Errors in the estimation of arterial wall shear rates that result from curve fitting of velocity profiles.* Journal of biomechanics, 1993. **26**(4-5): p. 383-90.
138. Schlichting, H., K. Gersten, and K. Mayes, *Boundary-layer theory*. 2016, Springer: Berlin :.
139. Naughton, J.W. and M. Sheplak, *Modern developments in shear-stress measurement.* Progress in Aerospace Sciences, 2002. **38**(6-7): p. 515-570.
140. Fernholz, H.H., et al., *New developments and applications of skin-friction measuring techniques.* Measurement Science and Technology, 1996. **7**(10): p. 1396-1409.
141. Lange, C.F., F. Durst, and M. Breuer, *Correction of hot-wire measurements in the near-wall region.* Experiments in Fluids, 1999. **26**(5): p. 475-477.
142. Durst, F., J.M. Shi, and M. Breuer, *Numerical prediction of hot-wire corrections near walls.* Journal of Fluids Engineering-Transactions of the Asme, 2002. **124**(1): p. 241-250.
143. Klanchar, M., J.M. Tarbell, and D.M. Wang, *In vitro study of the influence of radial wall motion on wall shear stress in an elastic tube model of the aorta.* Circulation research, 1990. **66**(6): p. 1624-35.
144. Moore, J.E., et al., *Fluid Wall Shear-Stress Measurements in a Model of the Human Abdominal-Aorta - Oscillatory Behavior and Relationship to Atherosclerosis.* Atherosclerosis, 1994. **110**(2): p. 225-240.
145. Born, S., et al., *Stent maps - Comparative visualization for the prediction of adverse events of transcatheter aortic valve implantations.* Ieee Transactions on Visualization and Computer Graphics, 2014. **20**(12): p. 2704-2713.
146. Stefanov, F., T. McGloughlin, and L. Morris, *A computational assessment of the hemodynamic effects of crossed and non-crossed bifurcated stent-graft devices for the treatment of abdominal aortic aneurysms.* Medical Engineering & Physics, 2016. **38**(12): p. 1458-1473.